Large-Eddy Simulation
of
Arctic Stratocumulus

Process Representation and Surface Heterogeneity

Inaugural-Dissertation

zur
Erlangung des Doktorgrades
der Mathematisch-Naturwissenschaftlichen Fakultät
der Universität zu Köln

vorgelegt von
Robert Rauterkus
aus Haltern am See

Köln, 2021

Berichterstatter

Prof. Dr. Yaping Shao

Prof. Dr. Ulrich Löhnert

Tag der mündlichen Prüfung

14.01.2021

Erklärung zur Dissertation

Hiermit versichere ich an Eides statt, dass ich die vorliegende Dissertation selbstständig und ohne die Benutzung anderer als der angegebenen Hilfsmittel und Literatur angefertigt habe. Alle Stellen, die wörtlich oder sinngemäß aus veröffentlichten und nicht veröffentlichten Werken dem Wortlaut oder dem Sinn nach entnommen wurden, sind als solche kenntlich gemacht. Ich versichere an Eides statt, dass diese Dissertation noch keiner anderen Fakultät oder Universität zur Prüfung vorgelegen hat; dass sie—abgesehen von unten angegebenen Teilpublikationen und eingebundenen Artikeln und Manuskripten—noch nicht veröffentlicht worden ist sowie, dass ich eine Veröffentlichung der Dissertation vor Abschluss der Promotion nicht ohne Genehmigung des Promotionsausschusses vornehmen werde. Die Bestimmungen dieser Ordnung sind mir bekannt. Darüber hinaus erkläre ich hiermit, dass ich die Ordnung zur Sicherung guter wissenschaftlicher Praxis und zum Umgang mit wissenschaftlichem Fehlverhalten der Universität zu Köln gelesen und sie bei der Durchführung der Dissertation zugrundeliegenden Arbeiten und der schriftlich verfassten Dissertation beachtet habe und verpflichte mich hiermit, die dort genannten Vorgaben bei allen wissenschaftlichen Tätigkeiten zu beachten und umzusetzen. Ich versichere, dass die eingereichte elektronische Fassung der eingereichten Druckfassung vollständig entspricht.

Teilpublikationen:

Rauterkus, R. and Ansorge, C., 2020: Cloud-Top Entrainment in Mixed-Phase Stratocumulus and its Process-Level Representation in Large-Eddy Simulation, *Journal of the Atmospheric Sciences*, **77(12)**, 4109–4127, doi: 10.1175/JAS-D-19-0221.1.

Rauterkus, R. and Ansorge, C., 2019: LES of Arctic Mixed-Phase Stratocumulus (ACLOUD RF13), *PANGAEA*, doi: 10.1594/PANGAEA.904399.

Robert Rauterkus
Bonn, 02.11.2020

Abstract

Small-scale processes are crucial for the evolution of Stratocumulus and act on scales reaching down to less than one meter. Most large-eddy simulation studies still apply a horizontal resolution of tens of meters, limiting the ability to resolve cloud-driving processes. I investigate such small-scale processes in a reference case that is—based on the recent field campaigns ACLOUD and PASCAL—defined within this thesis to represent a mixed-phase Stratocumulus during Arctic spring. I apply large-eddy simulations with horizontal resolutions of 35 m, 10 m, 3.5 m, and 3 m and a vertical resolution of about 3 m. My analysis focuses on the resolution sensitivity of cloud-top entrainment processes and the effects of surface heterogeneity structure on the atmospheric boundary layer. First, I find that for a horizontal grid spacing larger than 10 m, the effects of small-scale microphysical cooling and turbulent engulfment on cloud-top entrainment are only represented sufficiently for the atmospheric boundary layer bulk profiles but not on a process level. The stratification-limited size of energy-containing eddies violates the assumptions underlying many sub-grid scale models of turbulent mixing. Second, I observe a decrease in cloud-top entrainment for a horizontal resolution coarser than 10 m, which results in 15 % more cloud water after six hours of simulation and a corresponding optical thickening of the Stratocumulus. Third, I find that structuring surface heterogeneity does not affect zero- and first-order bulk quantities outside the surface layer. A notable sensibility in higher altitudes is only observed for higher-order quantities, which show increased values over structured surface heterogeneity. Fourth, I observe structured surface heterogeneity to form a streamwise elongated, roll-like, secondary circulation perpendicular to the mean wind. Its formation is neither captured by traditional Arctic lead theory nor by the theory of surface heterogeneity effects on cloud-free atmospheric boundary layers. It turns out that the streamwise elongated structure evolves due to streamwise “smudging” of the surface signals at the lower cloud boundary. This “smudging” is a consequence of weak vertical motion and cloud-induced turbulence—a unique feature compared to other studies investigating the effects of surface heterogeneity structure.

Acronyms

AA Arctic Amplification

ABL atmospheric boundary layer

(AC)^3 ArctiC Amplification: Climate Relevant Atmospheric and SurfaCe Processes, and Feedback Mechanisms

ACLOUD Arctic Cloud Observations Using Airborne Measurements During Polar Day

CFL Courant–Friedrichs–Lewy

CPU computing processing unit

CTE cloud-top entrainment

DNS direct numerical simulation

DYCOMS-II Dynamics and Chemistry of Marine Stratocumulus Phase II

HPC high-performance computing

LES large-eddy simulation

PASCAL Physical Feedbacks of Arctic Boundary Layer, Sea Ice, Cloud and Aerosol

Sc Stratocumulus

SGS sub-grid scale

TKE turbulence kinetic energy

WRF The Weather Research and Forecasting Model

Contents

Abstract **v**

Acronyms **vi**

1 Introduction **1**
1.1 Stratocumulus Feedback Mechanisms 4
1.2 Research on Stratocumulus 7
1.3 Research Proposition 11

2 Numerical Setup **13**
2.1 Large-Eddy Simulation 14
2.2 The Weather Research and Forecasting Model 17
2.2.1 Coordinate System 18
2.2.2 Physical Parameterization 19
2.2.3 Parallelization and Scaling Efficiency 27
2.3 Inclusion of Subsidence 31
2.3.1 Physical Derivation 32
2.3.2 Numerical Implementation 34

3 Model Evaluation by a Case of Subtropical Stratocumulus **37**
3.1 Campaign and Case Description 38
3.2 Model Adjustments 40
3.3 Results 44
3.3.1 Bulk Evolution of the Simulations 44
3.3.2 Sensitivity on Domain Size 49

4 Process-Level Representation of Arctic Stratocumulus 53
4.1 Campaign and Case Description . . . 54
4.2 Model Adjustments . . . 58
4.3 Results . . . 59
4.3.1 Representativity of the Results . . . 60
4.3.2 Representation of Turbulence . . . 61
4.3.3 Bulk Evolution of the Simulations . . . 63
4.3.4 Cloud-Top Entrainment . . . 67

5 Surface Heterogeneity Effects on Stratocumulus 75
5.1 Setup Description . . . 76
5.2 Model Adjustments . . . 77
5.3 Test Suite . . . 79
5.4 Results . . . 82
5.4.1 Bulk Evolution of the Basic Pattern . . . 82
5.4.2 Surface Heterogeneity Effects on the Atmospheric State . . . 86
5.4.3 Surface Heterogeneity Effects on Cloud-Top Entrainment and Cloud Structure . . . 90
5.4.4 Circulation Pattern and Heat Fluxes over Structured Surface Heterogeneity . . . 96
5.4.5 Effects on the Surface . . . 101

6 Conclusion 105

Acknowledgements 111

Bibliography 111

A Parameterization of Large-Scale Subsidence 129

B Pattern Creation Algorithm 133

C Model Modifications 137

Chapter 1

Introduction

The international movement *Fridays for Future* ultimately drew the attention of the general public towards the anthropogenic climate change we currently live in. However, the anthropogenic influence is nothing new. Studies in the 19th century already indicated that a higher greenhouse gas concentration might cause warming of near-surface air temperature (Tyndall, 1861; Arrhenius, 1897). This effect was considered to be rather small due to the low amount of emissions at that time. The concern in this topic grew throughout the 20th century because greenhouse gas emissions kept increasing rapidly. A consensus formed on the anthropogenic influence on changes in the global climate latest mid of the 20th century. Then, upcoming computers allowed for the first time to simulate former more theoretical concepts (Adem, 1965; Manabe and Wetherald, 1967). It was that time when experiments (Manabe and Wetherald, 1975; Manabe and Stouffer, 1980) revealed something astonishing—the warming in the polar regions is enhanced compared to the global average.

These early experiments are confirmed by the last decades—especially for the Arctic, where the near-surface air temperature rises about twice as fast as the global mean (Fig. 1b). This phenomenon is, in accordance with Manabe and Stouffer (1980), aptly termed *Arctic Amplification* (AA). Similar to global warming, Arctic warming comes along with drastic ecological and economic changes—possibilities and risks. For instance, the declining sea ice (Fig. 1a) facilitates new shipping routes (Rogers et al., 2013; Lee and Song, 2014) but also threatens the habitat of many Arctic animals such as polar bears (Regehr et al., 2007; Stern and Laidre, 2016). In addition, melting glaciers uncover new fossil resources but also induce sea-level rise, which threatens coastlines and islands as well as the millions of people living there (Gregory and Oerlemans, 1998; Zemp et al., 2019). AA also affects the weather and climate patterns, especially in the northern hemisphere. Many studies investigate and debate the reduced lower tropospheric temperature gradient between Arctic and mid-latitudes, which might cause shifting storm tracks (Cohen et al., 2014; Wang et al., 2017; Cohen et al., 2020).

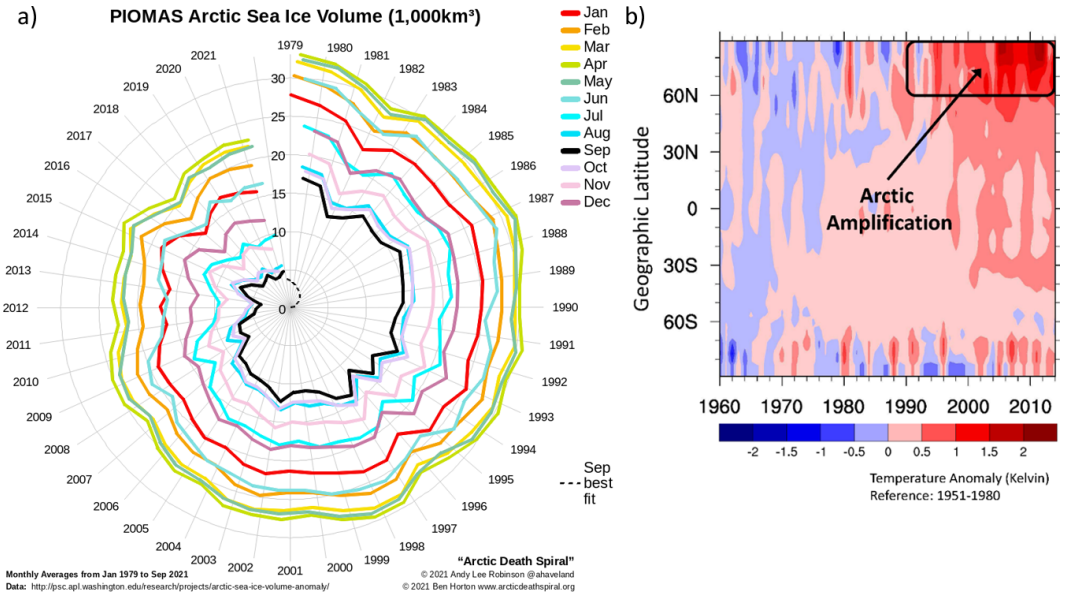

Figure 1: Averaged monthly Arctic sea-ice volume (a) and global near-surface temperature anomalies compared to 1951–1980 (b). The figures are accessed from Andy Lee Robinson and Ben Horton (www.acrticdeathspiral.org, 2021-10-31) and Wendisch et al. (2017).

These examples symbolize only some consequences of the current rapid Arctic warming. More exist, and scientists still struggle to grasp all of them. Even more problematic than not grasping all consequences of the rapid warming is that its reasons and prediction remain elusive (Hodson et al., 2013; Wendisch et al., 2017). Related research is not only of interest to understand AA itself. Indeed, the Arctic is often considered as a natural laboratory. For instance, its pristine air condition facilitates the investigation of aerosols and their relations to clouds. The seasonal contrast between polar night and day provides many distinct—nearly idealized—cases, such as stable stratifications of the atmospheric boundary layer (ABL) or extended Stratocumulus (Sc) decks. Similar situations, of course, also occur in other latitudes, but there they are usually only short-term and much more complex, for example, due to topography or the diurnal cycle. Consequently, understanding and projecting AA with all its processes not only yields more accurate global climate projections and therefore better estimates of future ecological and economic changes as well as weakening risks. Moreover, the knowledge gained from field studies, model experiments, and theoretical considerations can be applied to other latitudes and inject the physical understanding of the more short-term and complex cases observed there.

Of course, a complex phenomenon like AA with such far-reaching effects on the world's ecology and economy attracts scientists from many different disciplines such as chemistry, biology, oceanology, and meteorology. In the recent years, research got

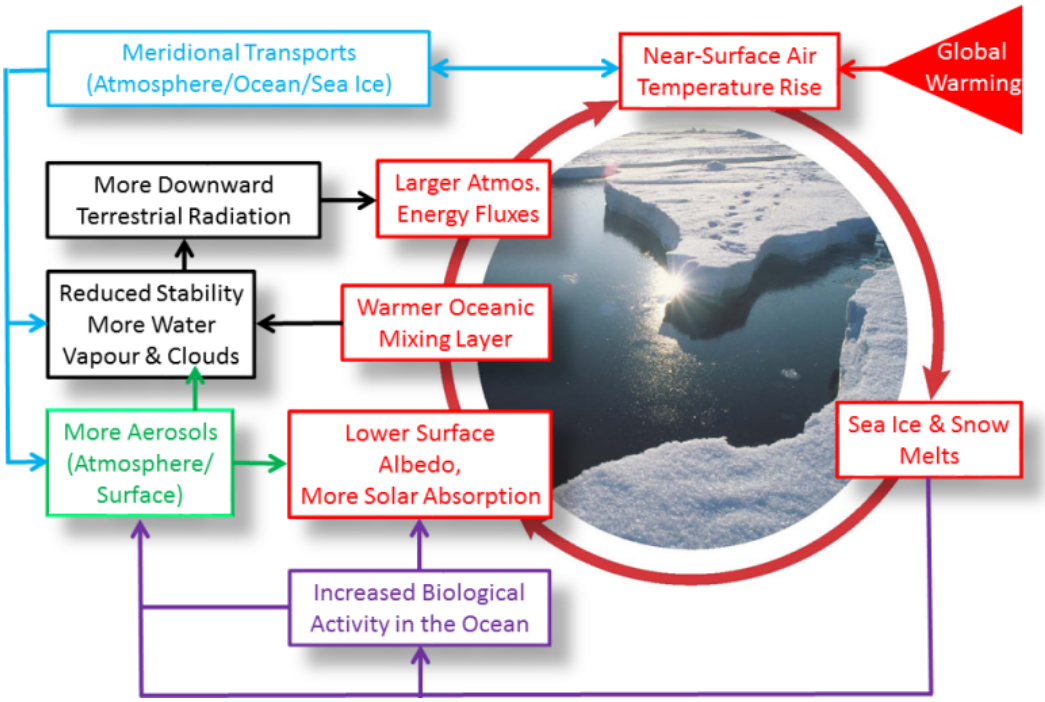

Figure 2: A selection of important feedback mechanisms and their interactions determining *Arctic Amplification*. Processes that are related to the surface (red), atmospheric water (black), atmospheric and oceanic transport (blue), aerosols (green), and oceanic biological activities (purple) are highlighted by colors. This figure is adapted from Wendisch et al. (2017) and can be accessed from www.ac3-tr.de.

enhanced and many interdisciplinary as well as international campaigns and projects were and are pushed. For example, the *World Meteorological Organization* declared the period from mid-2017 to mid-2019 as the *Year of Polar Prediction* (Jung et al., 2016), and end of 2019, the *RV Polarstern* participated in the *MOSAiC Expedition*[1]—a one-year-long expedition into the central Arctic. Also the *ArctiC Amplification: Climate Relevant Atmospheric and SurfaCe Processes, and Feedback Mechanisms* ((AC)^3)[2] was and is involved in many of these campaigns and projects and provided the framework of this thesis. (AC)^3 is a consortium of three universities and two research institutes. Its scientific objectives aim on identification, investigation, and evaluation of the key processes contributing to AA and to improve the understanding and quantification of related feedback mechanisms (Fig. 2).

A feedback mechanism describes a process where changing one quantity causes a second quantity to change, which in turn changes the first quantity. Feedback mechanisms are distinguished between positive feedbacks where changes in the first quantity are amplified and negative feedbacks where changes in the first quantity are damped. A well-known positive feedback mechanism is the ice–albedo feedback:

[1] www.mosaic-expedition.org
[2] www.ac3-tr.de

rising near-surface air temperature provokes melting of Arctic sea ice; the underlying ocean is less reflective than the sea ice and thus absorbs more solar radiation, which causes even warmer near-surface air temperatures (red circle in Fig. 2). Many feedback mechanisms exist in the Arctic (Fig. 2). Some are of a complexity comparable to the ice–albedo feedback presented above, and others are much more complex. Even the feedback mechanisms which are known and understood are often ambiguous in climate projections. Not only because physics or parameterizations remain uncertain but also because they interact and influence each other (Wendisch et al., 2017; Goosse et al., 2018).

Sc interacts with various feedback mechanisms whose most prominent contributors I present in Section 1.1. Although the prediction of Sc is especially crucial for the Arctic, climate projections also react sensitively to their representation in other latitudes. In turn, a lot of numerical, observational, and theoretical effort has been put throughout the last decades into the exploration of Sc (Section 1.2). However, the research on Sc, especially in the Arctic, is still ongoing. To support this research, in the framework of $(AC)^3$, I analyze in this thesis the effects of small-scale processes and their representation on Arctic Sc. To give a general overview of my work, I end this introductory chapter with a short description of the thesis structure as well as its scientific objectives (Section 1.3).

1.1 Stratocumulus Feedback Mechanisms

Sc is the most common cloud species in the Arctic ABL (Eastman and Warren, 2010). It may cover tens of thousands of square kilometers horizontally, but it is vertically confined to a few hundreds of meters, often only tens of meters (Wood, 2012). The combination of large horizontal coverage and small vertical extent causes Sc to be a leading uncertainty in prediction of the future Arctic climate and AA because climate models hardly resolve Sc explicitly. Even if they do so, their horizontal and vertical resolution allows not to capture the driving processes of Sc (Section 1.2), which is why many of them—or Sc as a whole—are parameterized. Parameterizations, in turn, depend heavily on our understanding of the underlying processes. While many individual processes are understood completely or at least to a sufficient degree, others are not (Wood, 2012; Kay et al., 2016; Mellado, 2017). The manifoldness of interactions between individual processes and their high sensitivity to the atmospheric quantities makes corresponding parameterizations also prone to errors.

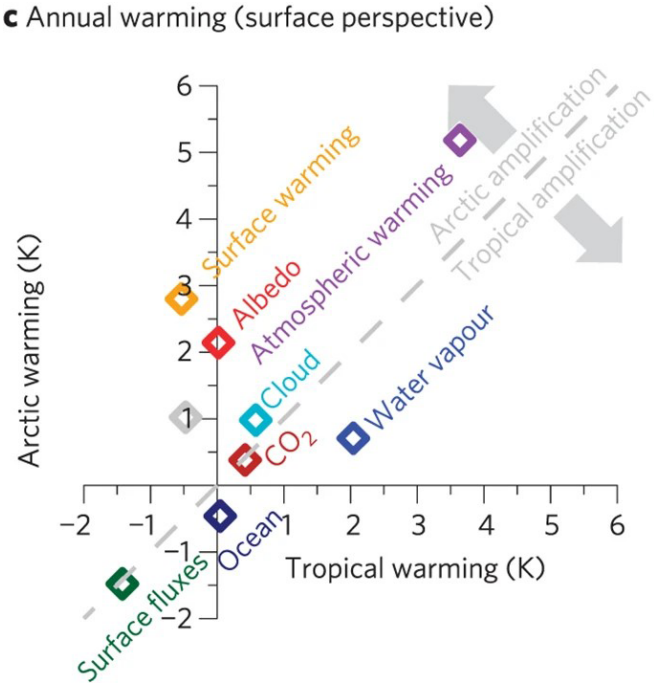

Figure 3: Annual arctic and tropical surface warming due to feedback mechanisms. The dashed line indicates homogeneous warming between the Tropics and the Arctic. Feedback mechanisms plotted above this line cause stronger warming in the Arctic than in the Tropics. Thus, they tend to reduce the surface temperature gradient between both regions. The distance to the dashed line correlates to the amplification's tendency. Feedback mechanisms plotted below this line act vice versa. This figure is accessed from Pithan and Mauritsen (2014).

Observations and climate projections indicate that cloud cover generally increases in the Arctic (Wang and Key, 2003; Vavrus, 2004; Zelinka et al., 2012). The net direct effect of all clouds on AA is estimated to be rather low (Fig. 3; Pithan and Mauritsen, 2014; Goosse et al., 2018) and is well understood: clouds reflect shortwave radiation back into space but also trap and emit longwave radiation. The intensity of both processes depends strongly on altitude, season, and surface type (Wang and Key, 2003; Shupe and Intrieri, 2004; Vavrus, 2004). All these measures influence the cloud properties that determine the interaction of clouds with radiation such as the ratio of liquid and solid cloud particles. Indeed, not only the surface properties but also their structure and heterogeneity can affect clouds. For example, (Gryschka et al., 1967) show that the heterogeneity of sea ice and oceanic water determines the formation of distinct roll clouds during cold air outbreaks, which would form a comparable solid cloud deck without these heterogeneities. Although the net direct effects of clouds on AA is considered to be rather small, clouds affect many feedback mechanisms directly and indirectly (such as *Albedo* and *Atmospheric warming* in Fig. 3) and also contribute to the surface water budget. Some of the most prominent feedback mechanisms, which Sc affect are outlined below: the cloud–albedo feedback, the cloud–optical depth feedback, and the lapse-rate feedback.[3]

[3]The discussions of the individual feedback mechanisms are limited to the effects of Sc, but other cloud types may induce similar or counteracting effects.

Cloud–Albedo Feedback The cloud–albedo feedback describes the interactions of Sc and the Arctic surface. Kay and Gettelman (2009), Morrison et al. (2018), and Yu et al. (2019) reveal that formation of Sc is correlated to the underlying surface types for all seasons but summer. Formation of Sc during summer is, according to them, mainly driven by large-scale atmospheric circulations because the Arctic surface is usually considerably colder than the ABL. In turn, no or only marginal surface–air interactions occur. The absence of sun or its low zenith angle during the other seasons is named to cause the ABL to cool or even to dissolve while the ocean stays relatively warm. Sensible and latent heat fluxes experience strong variations between relatively warm oceanic water and rather cold ice sheets. Over oceanic water, the heat fluxes promote formation of Sc, which in turn possibly hinders freezing of the oceanic water due to trapped longwave radiation. Summarized, these studies assume a positive feedback mechanism: Arctic surface warming leads to less sea ice which causes more formation of Sc; the increased Sc cloud cover hinders radiative cooling and causes, in turn, Arctic surface warming.

Cloud–Optical Depth Feedback The cloud–optical depth feedback summarizes changes in the microphysical properties that affect the optical depth of Sc. These changes can be straightforward, like changes in the liquid water path. But, they can also be more complex and difficult to capture and parameterize: ratio of liquid to solid particles, size of the individual hydrometeors, or the vertical and horizontal distribution of individual hydrometeor types (Zelinka et al., 2012; Ceppi et al., 2017). Despite the ratio between liquid and solid particles, this feedback mechanism is not even approximately ascertainable by climate models in the foreseeable future. However, the other contributors to the feedback mechanism are likely negligible and might even balance out on an annual or spatial average. Zelinka et al. (2012) and Ceppi et al. (2017) address the cloud–optical depth feedback to be negative for shortwave radiation and positive for longwave radiation in the Arctic. The net cloud–optical depth feedback is stated to be slightly negative due to an increasing optical depth of low-level clouds.

Lapse-Rate Feedback According to Pithan and Mauritsen (2014), lapse-rate feedback is the strongest contributor to AA. It arises because different altitudes warm with different intensities. AA is mainly confined to the near-surface atmosphere because strong temperature inversions frequently hinder convective heat transfer to the free troposphere. Consequently, the top of the atmosphere warms less intense, and the delta between the emitted longwave radiation at the surface and at the top of the atmosphere is larger than it would be for an uniform heating of the atmosphere (Fig. 4;

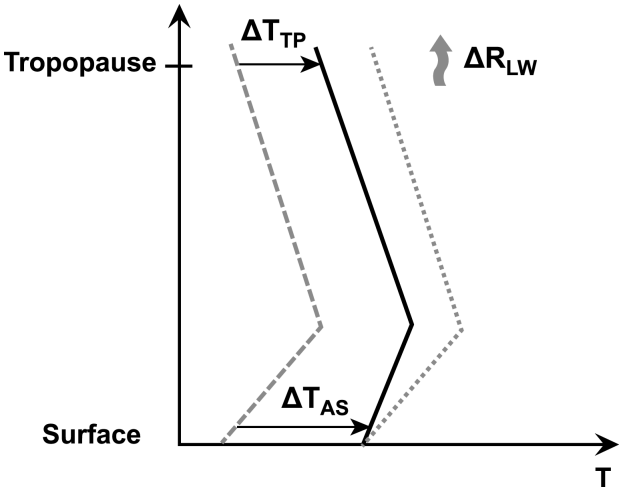

Figure 4: Scetched representation of the lapse-rate feedback mechanism. Contrary to uniform warming (dashed to dotted line), the surface experiences a stronger warming ΔT_{AS} than the upper atmosphere ΔT_{TP} (dashed to solid line). The resulting delta in longwave radiative flux ΔR_{LW} increases where the surface emits more longwave radiation than the upper atmosphere. This figure is adapted from (Pithan and Mauritsen, 2013).

Pithan and Mauritsen, 2013). The lapse-rate feedback evolves in general independent of Sc. But, Pithan et al. (2014) outline that the presence of temperature inversions is strongly related to Sc, whose under- and overestimation cause a major part of corresponding uncertainties in climate models. According to Pithan et al. (2014), the cycle of temperature inversion development can be summarized: moist and warm air is advected to the Arctic from lower latitudes and experiences radiative cooling from the surface; Sc forms in the colder atmosphere and erodes the temperature inversion; the Sc transforms into a lower and lower emissive ice cloud which again permits stronger radiative cooling from the surface; once the Sc is precipitated out, the ABL reaches a cloud-free state, and surface cooling again forms a surface inversion. Summarized, the lapse-rate feedback is considered to be generally positive, but increasing Sc cloud cover counteracts this feedback mechanism.

1.2 Research on Stratocumulus

[4]Section 1.1 outlines the large-scale effects and interactions of Sc. Still, it is important to recap that most Sc-driving processes such as cloud-top entrainment (CTE) and turbulence act on smaller scales of meters to millimeters (Wood, 2012; Mellado, 2017). CTE describes the mixing of cloudy and clear air along the upper cloud boundary. Thus, it heavily regulates the cloud's future development because it determines the surrounding moisture and temperature profiles (Mellado, 2017). A central measure to estimate cloud-top entrainment's strength is the entrainment velocity

$$w_{\mathrm{e}} = \partial_t z_{\mathrm{i}} - \tilde{w} \tag{1}$$

[4]Large parts of this section are excerpts of Rauterkus and Ansorge (2020); see footnote 21.

with z_i the ABL height and $\tilde{w}$ the large-scale subsidence (Stevens et al., 2005; Mellado, 2017). Thereby, a positive entrainment velocity correlates with a growing ABL height and indicates air mixing from above the ABL into it. This mixing may be, for example, induced by thermodynamic and dynamic instability resulting from shear or radiative and microphysical cooling at the cloud-top (Fig. 5). Accordingly, other turbulent measures such as turbulent moisture, heat, or mass fluxes also hint at the mixing's strength.

Mesoscale and climate models must parameterize Sc and its individual processes, which enhances corresponding uncertainties in such models (Tjernström et al., 2008; Pithan et al., 2014; Schneider et al., 2017). This delicacy is not only a consequence of Sc parameterization, but also Sc intensely interacts with other components of the Arctic climate system and sensitively responds to changes within them. For example, the evolution and optical properties of Sc strongly depend on anthropogenic and natural aerosols (Possner et al., 2017; Solomon et al., 2018), surface latent and sensible heat fluxes (Gultepe et al., 2003; Solomon et al., 2014), and atmospheric state variables such as temperature, humidity, and wind (Wood, 2012).

Arctic Sc is a matter of recent simulation-based studies (Klein et al., 2009; Pithan et al., 2014) and field campaigns (Verlinde et al., 2007; Tjernström et al., 2014) that affirm its importance for an understanding of the changing Arctic climate. These studies also reveal that there is a particular need for a better understanding of processes driving Sc. Field campaigns are one option to improve this process-level understanding. In-situ observations provide locally highly-resolved data but often lack adequate spatial coverage. On the contrary, remote sensing offers sufficient spatial coverage but often lacks local resolution. Sometimes precision becomes an issue in both approaches. A tailor-made combination of them allows for deep insight into the processes from a large-scale and local perspective. Recently, such a combination of different measurement techniques was shown to improve process-level understanding of Arctic Sc through the campaigns *Arctic Cloud Observations Using Airborne Measurements During Polar Day* (ACLOUD) and *Physical Feedbacks of Arctic Boundary Layer, Sea Ice, Cloud and Aerosol* (PASCAL) (Wendisch et al., 2017, 2019). Comparable field campaigns in the Arctic are scarce for observation-related challenges: low temperature, high relative humidity, and lack of daylight.

In lower latitudes, such extensively equipped field campaigns are more common (Albrecht et al., 1988; Stevens et al., 2003a; Zhou et al., 2004; Sorooshian et al., 2018). In the framework of these campaigns, large-eddy simulation (LES) is already a well-established research tool for process-level investigation of Sc (Stevens et al., 2005).

Indeed, observation and LES fertilize and complement each other. LES applies microphysical parameterizations, which are often calibrated using observational data. In turn, it may support field campaigns by forecasting conditions or suitable flight tracks, for instance, to reduce instrument icing or to ascertain adequate statistical coverage.The reason LES became such an essential tool for the investigation of Sc is that it allows one to modify in a straightforward and controlled manner the atmospheric state, cloud properties, and surface conditions. Such precise control of the initial and boundary conditions motivates the use of LES as a virtual laboratory where effects of particular changes can be studied and mechanistically attributed. While undoubtedly present in the field, such effects may be hardly, if at all, observable. In any case, the isolation of effects and cause–effect attribution is highly problematic in the field for the manifold interactions and broad-scale nature of meteorological processes. LES can unify the advantages of a high temporal and local resolution as well as sufficient spatial coverage. With recent advances in cost- and energy-efficient high-performance computing, the costs for such simulations are relatively low when compared to comprehensively equipped field campaigns, such as ACLOUD or PASCAL.

In practice, there is a dichotomy in numerical simulation between spatial coverage and high resolution that is overcome in my studies by extensive use of computational resources. Indeed, one to two decades ago, representation of CTE was problematic in many studies and known to be under-resolved, even in carefully designed dedicated LES inter-comparisons such as Stevens et al. (2005). Since an investigation of the idealized so-called smoke cloud (Bretherton et al., 1999), vertical resolution on the order of few meters and higher is applied. While an adequate process-level representation of CTE evidently requires a small vertical grid spacing, results concerning sensitivity towards horizontal resolution were contradictory at that time (Stevens and Bretherton, 1999; Lewellen and Lewellen, 1998). This ambiguity is shown to be a consequence of—consciously or unconsciously—tuning CTE by choice of grid resolution and aspect ratio to achieve a sufficient representation of the ABL and its cloudiness (Pedersen et al., 2016; Mellado et al., 2018). As discussed in Pedersen et al. (2016), higher horizontal resolution allows more small-scale turbulence, which enhances CTE. Contrary, applying higher vertical resolutions tends to strengthen the capping inversion, which hinders CTE. The increased inversion strength, however, depends on the definition of the capping inversion itself, which is either sharp or smooth. Pedersen et al. (2016) further show that domain size has only a minor effect on the results as long as it is large enough to encompass the largest updrafts. These results indicate that the use of strongly anisotropic small-sized grids substantially reduces computational demand

but at the same time neglects physical processes that act on small scales but drive the system.

More recently, LES-based studies (Matheou and Chung, 2014; Matheou, 2018) and direct numerical simulation (DNS) studies (de Lozar and Mellado, 2017; Mellado et al., 2018) investigated Sc with approximately isotropic grids up to a resolution of one meter (Mellado et al., 2018). These studies provide deep process-level insight into CTE (Fig. 5) and demonstrate that specific configurations of LES may only work for particular purposes. For example, the lower-resolved tuned setups mentioned above are sufficient in a forecasting context where many of the relevant properties are governed by the boundary conditions (Schemann and Ebell, 2020). But, their utility for process-level analysis is strongly limited. Although these numerical and also recent observational studies deepen our understanding of Sc CTE (Mellado, 2017), most of them focus on simplified cases. They are either idealized or substantially simplified by their reliance on equilibrium microphysics, neglect of solar radiation, being at a near-steady state, or confinement to a homogeneous surface or the open ocean. Comparable studies of more complex transitional cases are lacking to my knowledge, but they are essential to eventually predict why Sc forms, breaks up, or vanishes.[5]

LES studies on Arctic Sc are rare if compared to their lower-latitude counterpart. To date, they rely on strongly anisotropic grids with low horizontal resolution. Most of them focus on the complex microphysical processes, for instance the interaction of aerosols with distributions of liquid and solid hydrometeor species (Klein et al., 2009; Ovchinnikov et al., 2014; Solomon et al., 2014; Kaul et al., 2015; Young et al.,

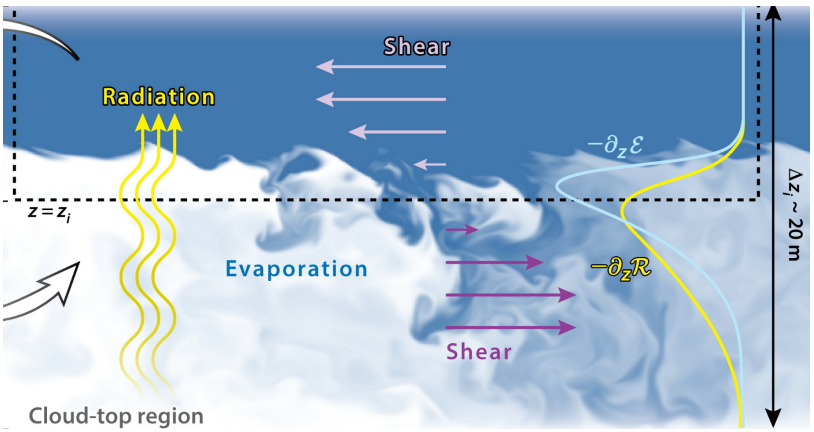

Figure 5: The individual processes determining cloud-top entrainment are shown with z_i the interface between cloud top and free troposphere, Δz_i the entrainment layer, and $\partial_z \varepsilon$ and $\partial_z R$ being proportional to cooling rates due to microphysics and radiation. This figure is accessed from Mellado (2017).

[5]The transition of Sc is a crucial component and uncertainty in climate models, for instance, while predicting the aforementioned lapse-rate feedback mechanism (Section 1.1).

2017). Those sensitivity studies show that LES ensembles exhibit substantial spread for mixed-phase clouds while they tend to converge more for liquid-only clouds. The complex interactions in multi-phase microphysical processes have been identified as one cause for this inter-model spread. However, as mentioned before, studies at lower latitudes indicate that higher horizontal resolution is required to gain a process-level understanding of the cloud-driving mechanisms. On top, the relatively small size of eddies in the Arctic ABL—as compared to its lower-latitude counterpart—also calls for higher resolution, in particular under neutral to stable conditions that frequently occur (Beare et al., 2006). Stable conditions are of particular relevance near the top of Sc, where CTE takes place. Thus, higher horizontal resolution ensures a realistic turbulence representation within the whole Arctic ABL and, at the same time, helps to physically understand cloud-driving processes such as CTE. Existing studies on Arctic Sc call for extensive process-level research and identify particular challenges to traditional cloud-resolving LES (Stevens et al., 2001, 2005; Neggers et al., 2011). First, as a consequence of stable stratification and shallow ABL height, characteristic eddies are smaller than in lower latitudes, which requires higher resolution. Second, Arctic Sc is predominantly of mixed-phase, and therefore microphysical processes are more complex than in liquid-only Sc.

1.3 Research Proposition

The preceding Sections 1.1 and 1.2 give a short overview on the importance of Sc for Arctic climate projections and describe related uncertainties and for which reasons they arise. It is outlined that a large part of the uncertainties not necessarily results from generally unknown processes. Instead, the uncertainties result from specific intermediate sub-processes, which are either not considered, difficult to parameterize, or not parameterized because of unknown underlying processes. LES is stated to be a suitable tool for the investigation of small-scale processes what may inject physical understanding, improve existing parameterizations, or even develop new parameterization approaches. I apply a highly-resolved LES in this thesis to investigate the representation and effects of small-scale processes on Sc. The thesis is structured into three major parts, which deal with specific research topics: model development and validation, process-level representation in Arctic Sc, and surface heterogeneity effects on Arctic Sc. The concluding Chapter 6 summarizes and synthesizes the results of the individual research objectives and provides an outlook on possible future research topics.

Model Development and Validation Chapter 2 presents the utilized LES model, which is also applied for the first time to simulations containing condensed water while simultaneously utilizing a horizontal resolution of only a few meters. The modified model and the, for the specific model, extreme setup demand validation preceding the main studies which is done in Chapter 3. The research objective of this part is:

> **O1: Can WRF-LES' simulate cloud-driving processes for mixed-phase Sc, and how are the results affected by horizontal resolution?**

Process-Level Representation of Arctic Stratocumulus Chapter 4 defines a semi-idealized Arctic mixed-phase Sc case, which is inspired by observations from ACLOUD and PASCAL. The case is simulated with three different horizontal resolutions. The corresponding analysis aims on the investigation of the processes determining CTE in mixed-phase Sc and their sensitivity towards horizontal resolution. The research objectives of this part are:

> **O2: Define and evaluate a semi-idealized mixed-phase Sc case during Arctic spring that is suitable for LES.**
>
> **O3: Which processes drive CTE in Arctic Sc?**
>
> **O4: Which processes cause sensitivity of Sc to horizontal resolution?**

Surface Heterogeneity Effects on Arctic Stratocumulus Chapter 5 investigates the effects structuring surface heterogeneity has on Arctic Sc. An algorithm for the creation of a structured surface pattern is developed. Two patterns which represent the limiting cases of surface heterogeneity structure cases are simulated, and corresponding effects on Arctic Sc and ABL are analyzed. The utilized case is loosely based on the formerly newly defined case of Arctic mixed-phase Sc. The research objective of this part is:

> **O5: How does surface heterogeneity affect Arctic Sc?**

Chapter 2

Numerical Setup

[6] Many atmospheric phenomena span spatially and temporally across multiple orders of magnitude (Fig. 6). Sc, for example, covers vast horizontal areas of up to tens of thousands of square kilometers. Simultaneously, its key processes act on scales of meters to millimeters (Section 1.2). If such small-scale processes are taken into account, numerical analysis and investigation of Sc require high resolution. However, the most extensive processes such as up- and downdrafts and individual cloud patches' interactions must not be neglected and demand a sufficiently large domain.

Process-level analysis of Sc requires highly resolved LES or even higher resolved DNS, whose approaches I outline in Section 2.1. Increasing the resolution and keeping the domain at a constant size usually comes with a leastwise cubic increase in computational costs. In turn, simulations demand vast computational resources if they represent large- and small-scale processes simultaneously. These resources can only be found on high-performance computing (HPC) systems.

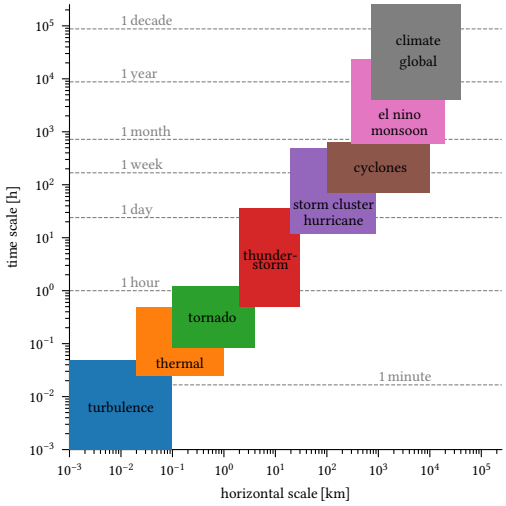

Figure 6: Atmospheric phenomena and their scales. Exemplary atmospheric phenomena are schematically related to their typical spatial and temporal scales.

[6] Parts of this chapter, especially Sections 2.2, 2.3.1, and the sub-grid scale paragraph of Section 2.2.2, are excerpts of Rauterkus and Ansorge (2020); see footnote 21.

All presented simulations were conducted at the *Juelich Supercomputing Center*. They utilize a modified version of the LES mode of *The Weather Research and Forecasting Model* (WRF) 4.0.3 (Skamarock et al., 2019), henceforth referred to as WRF-LES. A description of WRF-LES and its numerical scaling on the utilized HPC systems is given in Section 2.2. The initially required modification[7] to WRF-LES—the inclusion of large-scale subsidence—is outlined in Section 2.3.

2.1 Large-Eddy Simulation

The principal difficulty in atmospheric modeling lies in the non-linear effects and the broad spectrum of spatial and temporal scales observed in atmospheric phenomena (Fig. 6). The ratio between the largest and the smallest scale involved can easily exceed 10^6 for various atmospheric problems. For instance, thunderstorms may extend over kilometers, but also motion at the Kolmogorov microscale affects these storms and merely sizes millimeters or even less. Considering all scales of motion, DNS requires about $\mathcal{O}\left(10^{21}\right)$ grid points and a time step of $\mathcal{O}\left(10^{-4}\,\mathrm{s}\right)$ to simulate such a thunderstorm—optimistically estimated for a domain size of $10^8 \times 10^4\,\mathrm{m}^3$ and a maximum vertical velocity of $10\,\mathrm{m\,s}^{-1}$. Even on up-to-date HPC systems, the application of such a model is not possible.

LES offers a solution for this issue by coarsening the grid. A coarser grid still allows explicitly resolving the more extensive and thus most-dominant motions, frequently referred to as eddies. Such a simulation cannot explicitly account for eddies smaller than twice the grid spacing, whose corresponding wavenumber is referred to as cut-off wavenumber k_c. A sub-grid scale (SGS) model parameterizes the effects of non-resolved eddies. A common requirement of SGS models is k_c to lie within the so-called inertial subrange (Fig. 7), where theories exist on how turbulence cascades towards smaller scales and eventually dissipates (Kolmogorov et al., 1941, 1991).

The coarsening of the grid acts like low-pass filtering the prognostic equations. Below, the application of such a filter to the prognostic equation of the cartesian velocity $\mathbf{u} = (u_1, u_2, u_3)^T$ is described. The corresponding unfiltered equation reads

$$\partial_t u_i + \partial_{x_j} u_j u_i = F_{u_i} - \partial_{x_i} p \tag{2}$$

with p the moist air pressure, $\mathbf{x} = (x_1, x_2, x_3)^T$ the cartesian vector, and F_{u_i} summarizing

[7] More modifications are applied and presented in Appendix C. Additionally, the major changes are explained in this thesis.

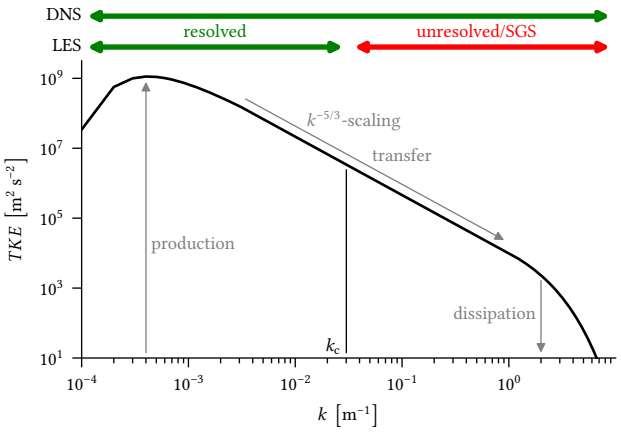

Figure 7: Energy cascade in idealized turbulent flows. An idealized spectrum of turbulence kinetic energy TKE is sketched and allows identifying the areas of production, dissipation, and the energy cascade where energy transfer from larger to smaller eddies dominates. Spectral bands are visualized at the top and symbolize the ranges large-eddy simulation (LES) and direct numerical simulation (DNS) resolve, based on the cut-off wavelength k_c.

all remaining source and sink terms contributing to u_i. Although this equation is a simplified version of the corresponding prognostic equations in WRF-LES (Eq. 17a–17c), the same methods can be analogously applied to all prognostic equations and yield similar but more complex expressions.

According to Leonard (1975), the filtered or resolved part $\overline{\psi}$ of an arbitrary quantity ψ is defined via convolution

$$\overline{\psi}(\mathbf{x}, t) = \int G(\mathbf{x} - \mathbf{r})\, \psi(\mathbf{r}, t)\, \mathrm{d}\mathbf{r} \tag{3}$$

with G the filter kernel and $\mathbf{r}$ an auxiliary cartesian vector for integration, corresponding to $\mathbf{x}$.[8] The corresponding unresolved part ψ' is defined as

$$\psi' = \psi - \overline{\psi}, \tag{4}$$

and the same definitions are valid for vectors. If a filter is applied to Eq. 2, the prognostic equation for the resolved part of u_i reads

$$\partial_t \overline{u}_i + \partial_{x_j} \overline{u_j u_i} = \overline{F}_{u_i} - \partial_{x_i} \overline{p} \tag{5}$$

where, according to Sagaut (2006), a homogeneous filter is assumed. Following Leonard (1975), it is shown that

$$\partial_{x_j} \overline{u_j u_i} = \partial_{x_j} \overline{\left(\overline{u}_j + u_j'\right)\left(\overline{u}_i + u_i'\right)} \tag{6}$$

$$= \partial_{x_j} \left[\overline{\overline{u}_j \overline{u}_i} + \overline{\overline{u}_j u_i'} + \overline{u_j' \overline{u}_i} + \overline{u_j' u_i'}\right] \tag{7}$$

[8] If $G = \begin{cases} 1/\Delta & \mathbf{x} - \mathbf{r} < \Delta \\ 0 & \text{else} \end{cases}$ with Δ the filter width, the filter acts like Reynolds filtering, and the same rules as for Reynolds averaging apply. Such a filter is commonly used in LES, also in WRF-LES.

$$= \partial_{x_j} \left[\overline{u}_j \overline{u}_i + \overline{\overline{u}_j \overline{u}_i} - \overline{u}_j \overline{u}_i + \overline{\overline{u}_j u_i'} + \overline{u_j' \overline{u}_i} + \overline{u_j' u_i'} \right] \tag{8}$$

where, according to Pope (2000), $C_{ij} = \overline{\overline{u}_j u_i'} + \overline{u_j' \overline{u}_i}$ is the cross stress representing interactions between resolved and unresolved eddies, $R_{ij} = \overline{u_j' u_i'}$ is the SGS Reynolds stress representing interactions of unresolved eddies, and $L_{ij} = \overline{\overline{u}_j \overline{u}_i} - \overline{u}_j \overline{u}_i$ is the Leonard stress representing interactions of resolved eddies.[9] Applying Eq. 7 results in

$$\partial_{x_j} \overline{u_j u_i} = \partial_{x_j} \left[\overline{u}_j \overline{u}_i + \left(\overline{u_j u_i} - \overline{u}_j \overline{u}_i \right) \right] \tag{9}$$

$$= \partial_{x_j} \left[\overline{u}_j \overline{u}_i + \tau_{ij} \right] \tag{10}$$

with τ_{ij} the SGS stress. Substituting (Eq. 10) into the prognostic equation for the resolved part of u_i (Eq. 5) yields

$$\partial_t \overline{u}_i + \partial_{x_j} \overline{u}_j \overline{u}_i = \overline{F}_{u_i} - \partial_{x_i} \overline{p} - \partial_{x_j} \tau_{ij}. \tag{11}$$

The task of the SGS model is to express the SGS stress τ_{ij} by resolved variables. This is commonly achieved by applying an eddy-viscosity model (Pope, 2000; Cottet et al., 2003; Schmitt, 2007), which relates τ_{ij} to the filtered rate of strain $\overline{S}_{ij}$ through the Boussinesq hypothesis

$$\tau_{ij} = -2\nu \overline{S}_{ij} + \frac{1}{3} \tau_{kk} \delta_{ij} \tag{12}$$

with ν the eddy viscosity coefficient and δ_{ij} the Kronecker delta. SGS models which apply the Boussinesq hypothesis define the filtered rate of strain by filtered velocities through

$$\overline{S}_{ij} = \frac{1}{2} \left(\partial_{x_j} \overline{u}_i + \partial_{x_i} \overline{u}_j \right). \tag{13}$$

The hypothesis is based on Boussinesq (1877) and implies in this form that small non-resolved scales have a purely dissipative effect on resolved scales. Substituting Eq. 12 into Eq. 11 yields

$$\partial_t \overline{u}_i + \partial_{x_j} \overline{u}_j \overline{u}_i = \overline{F}_{u_i} - \partial_{x_i} \overline{p} - \partial_{x_j} \left(-2\nu \overline{S}_{ij} + \frac{1}{3} \tau_{kk} \delta_{ij} \right) \tag{14}$$

$$= \overline{F}_{u_i} - \partial_{x_i} \left(\overline{p} + \frac{1}{3} \tau_{kk} \right) + 2\partial_{x_j} \left(\nu \overline{S}_{ij} \right) \tag{15}$$

$$= \overline{F}_{u_i} - \partial_{x_i} \tilde{p} + 2\partial_{x_j} \left(\nu \overline{S}_{ij} \right) \tag{16}$$

[9] In the case of Reynolds filtering L_{ij} and C_{ij} equal zero.

where $\tilde{p}$ is a modified pressure constrained by the continuity equation as a second equation. Thus, only ν remains to be determined by the SGS model (Section 2.2.2).

2.2 The Weather Research and Forecasting Model

WRF 4 solves the compressible non-hydrostatic prognostic equations for dry air surface pressure, moist potential temperature θ_m, geopotential ϕ, cartesian velocities u, v, and w, thus $\mathbf{u} = (u, v, w)^T$, and optionally various scalars χ, such as tracer or moisture mixing ratios. The prognostic equations are given in mass-coupled flux-form and read (Skamarock et al., 2019, their Eq. 2.8–2.14):

$$\partial_t \mu_\mathrm{d} u + \nabla \cdot \mu_\mathrm{d} \mathbf{u} u + \mu_\mathrm{d} \alpha \partial_x p + \alpha/\alpha_\mathrm{d} \partial_\eta p \partial_x \phi = F_{\mu_\mathrm{d} u} \tag{17a}$$

$$\partial_t \mu_\mathrm{d} v + \nabla \cdot \mu_\mathrm{d} \mathbf{u} v + \mu_\mathrm{d} \alpha \partial_y p + \alpha/\alpha_\mathrm{d} \partial_\eta p \partial_y \phi = F_{\mu_\mathrm{d} v} \tag{17b}$$

$$\partial_t \mu_\mathrm{d} w + \nabla \cdot \mu_\mathrm{d} \mathbf{u} w - g\left(\alpha/\alpha_\mathrm{d} \partial_\eta p - \mu_\mathrm{d}\right) = F_{\mu_\mathrm{d} w} \tag{17c}$$

$$\partial_t \mu_\mathrm{d} \theta_\mathrm{m} + \nabla \cdot \mu_\mathrm{d} \mathbf{u} \theta_\mathrm{m} = F_{\mu_\mathrm{d} \theta_\mathrm{m}} \tag{17d}$$

$$\partial_t \mu_\mathrm{d} + \nabla \cdot \mu_\mathrm{d} \mathbf{u} = 0 \tag{17e}$$

$$\partial_t \phi + \mathbf{u} \cdot \nabla \phi - g w = 0 \tag{17f}$$

$$\partial_t \mu_\mathrm{d} \chi + \nabla \cdot \mu_\mathrm{d} \mathbf{u} \chi = F_{\mu_\mathrm{d} \chi} \tag{17g}$$

Here, α and α_d represent the inverse densities of moist and dry air, g is the gravitational constant, and η is the vertical coordinate. The coordinate metric μ_d is in general proportional to the mass per grid cell. However, in WRF-LES, μ_d is proportional to the column mass due to the chosen coordinate system (Section 2.2.1). The terms F are the source and sink terms of their indexed quantity and arise, for example, from physical parameterizations (Section 2.2.2).

Although compressibility and some missing LES features count against the usage of WRF 4, it offers several advantages outweighing these drawbacks. In particular, WRF 4 is open-source and used by a large community. It runs and scales well across several computing architectures—including those present at the *Juelich Supercomputing Center* (Section 2.2.3—and provides the capability to simulate at the mesoscale. A transfer of results and parameterizations between LES and mesoscale simulation is therefore straightforward. WRF 4 also contains various well-established and documented physical parameterizations, especially for mixed-phase microphysics.

Doubly-periodic boundary conditions are applied for all simulations, as well as a fifth-order centered-differences advection scheme—except for the vertical scalar ad-

vection, where a complementary third-order scheme is applied. Following Pressel et al. (2017), the advection schemes are monotonic for all scalar variables to eliminate unphysical drying above the cloud layer, which is observed otherwise in all simulations. Time integration is carried out by a third-order Runge–Kutta scheme separating low-frequency meteorological from high-frequency acoustic modes with the help of a time-split integration as described by Wicker and Skamarock (2002).

2.2.1 Coordinate System

The prognostic equations are solved on a regular cartesian grid horizontally and utilize a hybrid sigma–pressure coordinate system in the vertical. Thereby, η follows the coordinate system proposed in Park et al. (2013). Thus,

$$p_\mathrm{d} = B(\eta)\,(p_\mathrm{s} - p_\mathrm{t}) + [\eta - B(\eta)]\,(p_0 - p_\mathrm{t}) + p_\mathrm{t} \tag{18}$$

with p_d the hydrostatic component of dry air pressure, and p_s and p_t representing its corresponding values at the surface and the model top. The function $B(\eta)$ describes the weighting between the terrain-following sigma coordinate system and the pressure coordinate system. Examples of the utilizable systems are sketched in Fig. 8.

$B(\eta) = \eta$ is applied in WRF-LES and produces a pure sigma coordinate system, as it is the case for WRF 3 (Skamarock et al., 2008, their Eq. 2.1). Doing so, Eq. 18 transforms to

$$\eta = \frac{p_\mathrm{d} - p_\mathrm{t}}{\mu_\mathrm{d}} \tag{19}$$

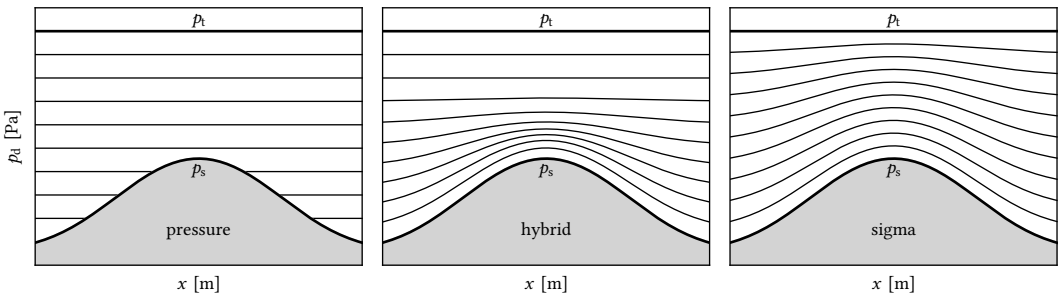

Figure 8: Realizations of different vertical coordinate systems. From left to right, a pure pressure coordinate system, a hybrid sigma–pressure coordinate system, and a pure sigma coordinate system are visualized. The gray shaded area symbolizes surface topography and the black lines represent the model levels on which the vertical coordinate η is constant. Thereby, η and the hydrostatic component of dry air pressure p_d, p_s and p_t represent its corresponding values at the surface and the model top, decrease from bottom to top. This figure is adapted from Skamarock et al. (2019).

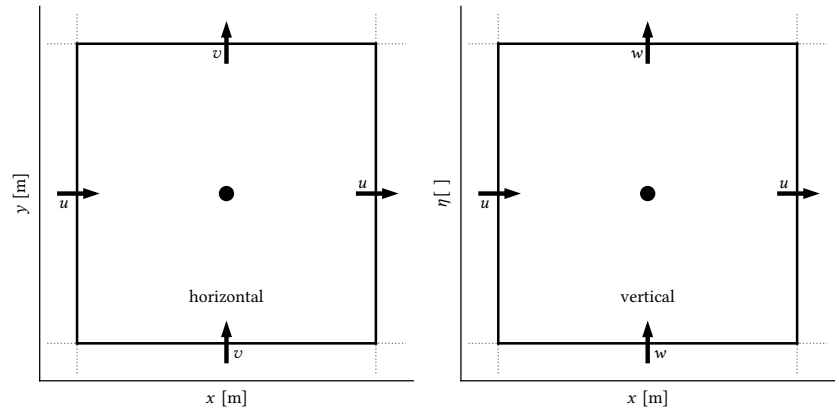

Figure 9: Visualization of horizontal and vertical C-grid staggering. Horizontal (left) and vertical (right) C-grid staggering in *The Weather Research and Forecasting Model*. The velocity components are staggered in space on the interfaces between two grid cells (lines). All prognostic non-velocity variables are stored in the middle of a grid cell, the so-called mass-points (dots). Geopotential takes on a special position and is also staggered vertically. This figure is adapted from Arakawa and Lamb (1977).

with the expression μ_d being the column mass per unit area

$$\mu_\mathrm{d} = p_\mathrm{s} - p_\mathrm{t}. \tag{20}$$

In the case of $B(\eta) = 0$, a pure pressure coordinate is applied. By default, WRF 4 utilizes a smooth transition from a pure sigma coordinate at the surface to a pure pressure coordinate above a certain level η_c (Skamarock et al., 2019). This transition is achieved through the definition of

$$B(\eta) = c_1 + c_2\eta + c_3\eta^2 + c_4\eta^3 \tag{21}$$

with the coefficients c_1, c_2, c_3, and c_4 being constrained by the boundary conditions

$$B(1) = 1, \quad \partial_\eta B(\eta) = 1, \quad B(\eta_\mathrm{c}) = 0, \quad \text{and} \quad \partial_\eta B(\eta_\mathrm{c}) = 0. \tag{22}$$

WRF-LES utilizes a staggered Arakawa C-grid (Arakawa and Lamb, 1977) in all dimensions to store its variables (Skamarock et al., 2019). Most variables, such as moist potential temperature or other scalars and the pressure, are stored on mass-points in the center of a grid cell. The cartesian velocities u, v, and w are staggered to the interfaces between two grid cells, offset in the respective velocity direction (Fig. 9).

2.2.2 Physical Parameterization

Parameterization is a standard method in atmospheric modeling: processes that are too small-scale or too complex to be explicitly represented are alternately expressed by

resolved physically relevant variables using empirical or ad-hoc relationships (Stensrud, 2007). Parameterizations rely heavily on how well the processes they represent are understood. Examples for such parameterizations include the interaction of radiation with aerosols or the descent of individual snowflakes. Frequently, parameterizations evolve from theoretical considerations or are estimated by observational data. Thus, often various parameterizations exist for one and the same problem. They are a natural cause of uncertainty in atmospheric modeling since they imply many assumptions and are often constrained to specific circumstances (Stensrud, 2007). LES already applies a resolution of a few tens of meters and below. Therefore, LES requires contrary to mesoscale models less parameterizations because the ABL and convective up- and downdrafts are explicitly represented on the model grid. However, some processes such as microphysics, radiation, SGS motions, and atmosphere–surface interactions still require parameterization.

Microphysics Microphysical parameterizations are divided into two categories: bin models and bulk models (Morrison et al., 2020). Bin models explicitly predict the evolution of the individual size distribution for each hydrometeor type. On the contrary, bulk models assume a fixed shape of the individual size distribution, such as

$$n(D) = n_0 d^{\mu} e^{\lambda d} \tag{23}$$

for cloud and rain droplets in Morrison et al. (2009). Here, n_0, λ, and μ are the intercept, slope, and shape parameters of the exponential distribution, and n and d are the droplet number concentration and diameter. While μ is specified for each hydrometeor type in the parameterization, n_0 and λ are derived by the corresponding droplet number concentration and mixing ratio. In turn, droplet number concentration and mixing ratio are parameterized based on the atmospheric state. As a result, bulk models are generally more numerical efficient than bin models (Harrington et al., 1999; Jiang et al., 2000).

The utilized microphysical parameterization is described in Morrison et al. (2005) and Morrison et al. (2009) and is a two-moment bulk model named *Morrison-2-Moment Scheme*. It predicts not only the mixing ratio of each hydrometeor type like most bulk models do, but it additionally estimates the particle number concentration of the respective hydrometeor type. The parameterization assumes the shape of all particles to be spherical and offers a prognostic supersaturation (Morrison et al., 2005, 2009). The prognostic mixing ratio and number concentration are simulated for five hydrometeor types (Fig. 10): cloud ice, snow, cloud water, rain, and graupel. In theory,

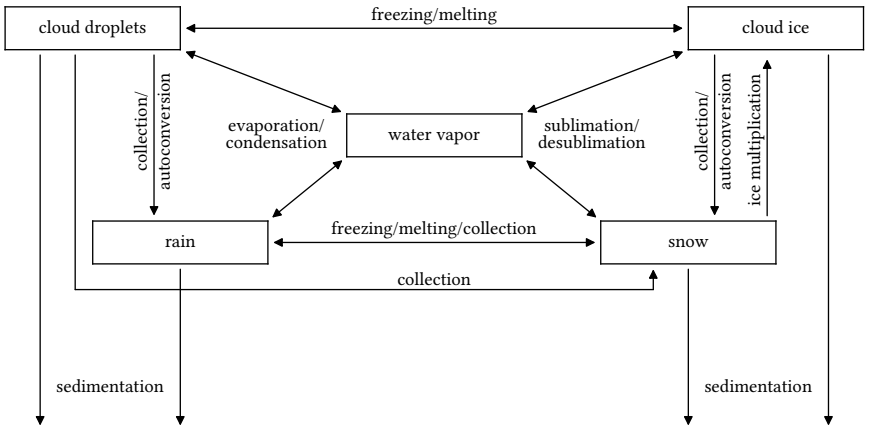

Figure 10: Hydrometeor types and their parameterized interactions. In the squared boxes, the hydrometeor types are shown, which the utilized parameterization predicts. The arrows mark parameterized processes causing changes between the corresponding hydrometeor types. This figure is adapted from Morrison et al. (2005).

the parameterization therefore adds ten prognostic variables, but Sc produces no graupel, and thus, the corresponding option is deactivated. Also, the parameterization's version implemented in WRF 4 offers only a prognostic cloud water particle number concentration if the chemistry module of WRF 4 is activated, which is not the case. Consequently, instead of ten prognostic variables, only seven are added. The parameterization can furthermore be constrained by a specific cloud droplet and ice nuclei number concentration. These parameters have a large impact on the parameterization by affecting the microphysical state (Morrison and Pinto, 2006; Morrison et al., 2008; Hines and Bromwich, 2017).

Radiation Radiative parameterizations estimate the radiative flux and the resulting temperature tendencies for the atmosphere. Thereby, they solve the radiative transfer equation for the whole radiative spectrum. It is possible to distinguish these parameterizations into two approaches: line-by-line models and spectral band models (Clough et al., 2005). Line-by-line models solve the radiative transfer equation for each frequency[10] for all atmospheric molecules. While such models might be suitable for comparison with instruments measuring only dedicated frequencies, they demand vast computational resources because of the broad range of frequencies and the number of molecules to consider.

Contrary, spectral band models divide the radiative spectrum into several broader frequency ranges, which are dominated by specific molecules. Although less molecules

[10] In line-by-line models, a specific frequency is, in fact, only a very narrow and nearly monochromatic frequency range.

are considered, their absorption coefficients β vary intensely and irregularly within the individual spectral bands and still demand vast computational resources for each considered frequency f (Goody and Yung, 1989). One can overcome this issue by sorting the absorption coefficients in ascending order. Doing so, the former irregular curve $\beta(f)$ becomes a smooth curve $\beta(\gamma)$ where $\gamma(\beta)$ is somewhat like a cumulative probability function of the absorption coefficients (Mlawer et al., 1997, their Fig. 1). With the radiative transfer equation being invariant to the arrangement, and the curve being smooth, only a few characteristic quadrature points have to be evaluated to solve the radiative transfer equation for the given spectral band (Goody et al., 1989; Mlawer et al., 1997). According to Pawlak et al. (2004), the required calculations reduce down to $\mathcal{O}\left(10^2\right)$ quadrature points for the whole radiative spectrum while still maintaining an accuracy comparable to line-by-line models.

I utilize the *RRTMG Scheme* (Iacono et al., 2008), which is based on the *RRTM* (Mlawer et al., 1997) and applies the above-mentioned correlated-k method. According to Iacono et al. (2008), the *RRTMG Scheme* was developed with the objective of a better performance for the inclusion into general circulation models but still providing comparable accuracy. Analogous to the *RRTM*, the *RRTMG Scheme* utilizes 16 spectral bands for longwave calculation and 14 spectral bands for shortwave calculation. In the shortwave, extinction is modeled for water vapor, carbon dioxide, ozone, methane, oxygen, nitrogen, aerosols, and Rayleigh scattering in the shortwave. Modeled longwave absorbers are water vapor, carbon dioxide, ozone, nitrous oxide, methane, oxygen, nitrogen, and halocarbons. The radiative transfer equation is solved by a two-stream solver described in Oreopoulos and Barker (1999). Consequently, the entire light field is separated into only one upward and one downward stream, which are weighted averages of their respective hemispheres. Furthermore, SGS cloud variability is considered by the *Monte Carlo Independent Column Approximation* (Pincus et al., 2003). It divides every cloudy grid cell into multiple sub-columns, which are filled with random cloud states—if possible, based on a known probability density distribution—and calculates their individual radiative fluxes. The weighted average of the individual radiative fluxes denotes the final radiative flux. Thereby, the higher the amount of sub-columns is, the lower is the method's stochastic error.

Sub-Grid Scale As outlined in Section 2.1, the main task of the SGS model is to parameterize the effects of non-resolved motion by defining an expression for ν. The utilized SGS model is based on the theories of Lilly (1962) and Smagorinsky (1963). This model is constrained by the Smagorinsky coefficient $C_S = 0.25$ and takes buoyancy

effects into account with the help of the Brunt–Väisälä frequency B_f. Thus, ν is calculated via

$$\nu = (C_\mathrm{S}\Delta)^2 \sqrt{\max\left(0, \overline{S}^2 - \frac{B_\mathrm{f}^2}{P}\right)} \tag{24}$$

with $P = \frac{1}{3}$ the turbulent Prandtl number and $\Delta = \sqrt[3]{\Delta_x \Delta_y \Delta_z}$ a length scale corresponding to resolution and filter width where Δ_x, Δ_y, and Δ_z are the resolutions along the cartesian coordinates. The characteristic filtered rate of strain $\overline{S}$ contains information on the velocity gradients and is defined by

$$\overline{S} = \sqrt{2\overline{S}_{ij}\overline{S}_{ij}} \tag{25}$$

with $\overline{S}_{ij}$ as in Eq. 13. Although the model applies Eq. 24, for the derivation below and the model output $\frac{B_\mathrm{f}^2}{P} \ll \overline{S}$ is assumed.

The expression in Eq. 24 provides no explicit information on the non-resolved turbulence kinetic energy (TKE), TKE_s—neither does WRF 4 for this parameterization. To assess the relative importance of unresolved turbulent mixing, below a spectral approximation of TKE_s, which is consistent with the assumptions of the utilized closure, is derived. It is possible to estimate TKE_s via

$$TKE_\mathrm{s} = \int_{k_\mathrm{c}}^{\infty} E(k)\, \mathrm{d}k \tag{26}$$

with E the energy spectrum of motion. In case k_c lies within the inertial subrange, a sufficient approximation of the energy spectrum is the Kolmogorov spectrum (Pope, 2000), thus

$$TKE_\mathrm{s} \approx \int_{k_\mathrm{c}}^{\infty} C\varepsilon^{\frac{2}{3}} k^{-\frac{5}{3}}\, \mathrm{d}k \tag{27}$$

$$= -\frac{3}{2} C\varepsilon^{\frac{2}{3}} k^{-\frac{2}{3}} \Big|_{k_\mathrm{c}}^{\infty} \tag{28}$$

$$= \frac{3}{2} C \left(\frac{\varepsilon}{k_\mathrm{c}}\right)^{\frac{2}{3}} \tag{29}$$

where ε is the dissipation rate and $C = 1.5$ the Kolmogorov constant. The filter width defines $k_\mathrm{c} = \frac{\pi}{\Delta}$, and it follows that

$$TKE_\mathrm{s} = \frac{3}{2} C \left(\frac{\varepsilon\Delta}{\pi}\right)^{\frac{2}{3}}. \tag{30}$$

In accordance with the underlying assumptions of the parameterization, it is assumed that dissipation and production P_r balance each other, that is, $\varepsilon = P_\mathrm{r}$. In the case of eddy-viscosity models, it is $P_\mathrm{r} = \nu\overline{S}^2$ (Pope, 2000) and substituting Eq. 24 in Eq. 12 finally yields

$$TKE_\mathrm{s} = \frac{3}{2} C \left(\frac{\Delta^3 C_\mathrm{S}^2 \overline{S}^3}{\pi} \right)^{\frac{2}{3}} . \tag{31}$$

All measures but $\overline{S}$ are known from the utilized model setup, and thus estimation of TKE_s only demands the storage of $\overline{S}$ to the output files, which is not provided by default. The corresponding measure is calculated at the end of routine *cal_deform_and_div (module_diffusion.F)*, which determines the individual deformation tensor components:[11]

```
sub_tke = 0.5 * (defor11*defor11 + defor22*defor22 + defor33*defor33 ) + &
          defor12*defor12 + defor13*defor13 + defor23*defor23
sub_tke(i,k,j) = sqrt(sub_tke)
```

The variable *sub_tke* contains the desired quantity but can not be written to the output files by this routine. First, a corresponding variable must be added to the *registry (Registry.EM_COMMON)*:[12]

```
state real rora_tke ikj misc 1 - - "DEFOR_TRACE" "deformation tensor trace" "m s-1"
```

This line adds a variable *rora_tke* to the *grid*, which is the output variable of WRF 4. The new variable is accessible via *grid%rora_tke* in all top-level routines of the model, such as the routine *first_rk_step_part2 (module_first_rk_step_part2.F)*, which calls the routine *cal_deform_and_div*. Passing *sub_tke* between both routines and storing it on the *grid* allows to provide the desired output.[13] An initialization of this variable is not required because it is purely diagnostic and has no effects on other model variables.

Surface All simulations apply a temporally constant surface to reduce complexity arising from atmosphere–surface interaction. Nevertheless, most of them require estimation of the non-constant surface fluxes to provide a lower boundary condition. Surface properties and surface fluxes are parameterized in WRF 4 by two different physical modules: a land-surface parameterization calculates the evolution of surface

[11] It is also possible to access the variable *temp* from the routine *smag_km (module_diffusion.F)*. This variable additionally contains the stability correction as prescribed in Eq. 24.

[12] WRF's registry defines all model variables and namelist parameters. Within the registry, it is possible, for example, to disable or enable the output of specific variables or to check default values of parameters. Every change within the registry requires a full recompilation of the model.

[13] I do not activate output of the variables in the registry. Instead, a dedicated output history stream file is utilized, which allows to change output variables without recompiling the whole model.

properties, and a surface-layer parameterization calculates the surface fluxes. The latter parameterizes not the atmosphere–surface interface but instead the so-called surface layer, which extends about the lowest 10 % of the ABL. Turbulent fluxes vary in the surface layer less than 10 %, and only the microlayer lies below it—extending a few centimeters and being dominated by molecular transport (Stull, 1988).

However, in atmospheric modeling, the surface-layer parameterization usually parameterizes merely the atmosphere below the lowest model level to provide the lower boundary condition. The corresponding distance might equal roughly the surface layer in mesoscale or climate models but is much less than the surface layer in LES. The presented simulations either provide afore known constant surface fluxes or apply the *Revised MM5 Scheme*. According to Jiménez et al. (2012), this parameterization estimates the surface fluxes of momentum τ, sensible heat SH, and latent heat LH as:

$$\tau = \rho C_\mathrm{d} U_\mathrm{a}^2 \tag{32}$$

$$SH = \rho c_\mathrm{p} C_\mathrm{h} U \left(\theta_0 - \theta_\mathrm{a}\right) \tag{33}$$

$$LH = L\rho M C_\mathrm{q} U \left(q_0 - q_\mathrm{a}\right) \tag{34}$$

Here, C_d, C_h, and C_q represent the transfer coefficients for momentum, heat, and moisture, ρ represents the moist air density, M is the soil moisture availability, and L and c_p are the latent heat of vaporization and the specific heat capacity at constant pressure. The parameterization requires temperature θ and moisture q scales at the surface, indexed by 0, and a value at the lowest model level, indexed by a. The surface layer wind speed U is also required and estimated from the horizontal wind speed of the lowest model level U_a, enhanced by a convective velocity (Beljaars, 1995) and an SGS velocity (Mahrt and Sun, 1995).

Estimation of the transfer coefficients is achieved by utilizing Monin–Obukhov similarity theory. First, the bulk Richardson number Ri_b is estimated via

$$Ri_\mathrm{b} = gz \frac{\theta_\mathrm{va} - \theta_\mathrm{v0}}{\theta_\mathrm{a} U^2}, \tag{35}$$

with θ_v0 and θ_va being the virtual potential temperatures at the surface and the lowest model level. The bulk Richardson number is a measure to estimate the stability of the surface layer: $Ri_\mathrm{b} < 0$ indicates free convection, $Ri_\mathrm{b} = 0$ indicates forced convection, $0 < Ri_\mathrm{b} < 0.2$ indicates damped mechanical turbulence, and $Ri_\mathrm{b} \geq 0.2$ indicates stable conditions (Jiménez et al., 2012). For each regime, various stability functions were estimated in the past to determine the transfer coefficients. According to Jiménez et al.

(2012), for unstable conditions, a weighted average of the stability functions proposed in Fairall et al. (1996) and Paulson (1970) is applied where the former represents highly unstable conditions and the latter considers conditions closer to neutral stability. For stable conditions, the formulation of Cheng and Brutsaert (2005) is adopted.

2.2.3 Parallelization and Scaling Efficiency

Simulations were performed on three different HPC systems at the *Juelich Supercomputing Center*: *juqueen*, *juwels*, and *jureca* (Tab. 1). The amount of computing processing units (CPUs) used on each system was typically $\mathcal{O}\left(10^3\right)$, and the utilized parallelization mechanisms applied shared memory (OpenMP) and distributed memory (MPI). Several scaling and performance tests considering numerical scaling and the composition of OpenMP and MPI were conducted ahead to achieve a certain degree of efficiency because computing resources of $\mathcal{O}\left(10^6\,\mathrm{CPU\,h}\right)$ were required. Before I analyze these performance tests below, a description of the parallelization approach in WRF 4 is given.

Parallelization Approach WRF 4 utilizes parallelization by a two-dimensional grid decomposition over the whole domain. The domain gets decomposed horizontally into a specific amount of patches equal to the amount of MPI tasks. If possible, these patches are of equal size to reduce unbalanced workload and, in turn, idle CPUs. The parallelization mechanism of WRF 4 forms the patches as quadratic as possible and ensures a rectangular shape. Each patch is simulated by an individual MPI process, and communication between individual patches is hindered. Every patch has a halo region surrounding it (Fig. 11) where it can read but not write information from the neighboring patch. The halo region is updated every iteration by calls to the parallel infrastructure, and its size depends on the utilized advection scheme to provide the required boundary conditions. For the presented studies, the halo region seizes five grid points on each side. Each patch is decomposed along the y-axis into as many tiles as OpenMP threads are available. The tiles are not quadratic but still as equally sized as possible to reduce idle time resulting from unbalanced workloads. All tiles of one patch share their memory and can communicate with each other directly.

Table 1: Characteristics of the utilized high-performance computing systems *juqueen*, *juwels*, and *jureca* where only computing nodes are considered. The configuration represents the utilized node configuration for the presented simulations, but other node configurations exist.

	juqueen	*juwels*	*jureca*
performance $\left[\mathrm{PFlop\,s^{-1}}\right]$	5.9	10.7	6.8
processors [CPU]	458 752	122 768	156 448
memory [TB]	448	268	444
configuration $\left[\mathrm{CPU\,node^{-1}}\right]$	16	48	24

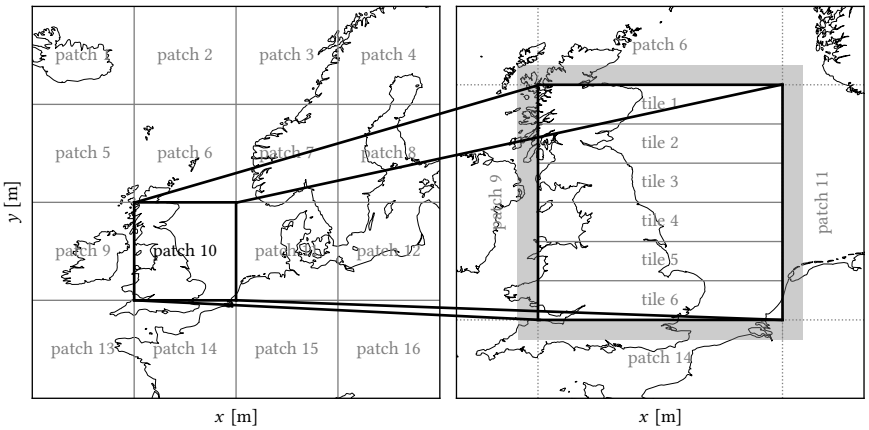

Figure 11: Horizontal domain decomposition for parallelization in *The Weather Research and Forecasting Model* 4. On the left, the domain is decomposed into individual patches, and on the right, one patch is decomposed into individual tiles. The halo region is exemplarily indicated for patch 10 by the gray shaded area.

Parallel Configuration With MPI tasks representing the calculation on patches and OpenMP threads representing the calculation on their tiles, WRF 4 offers a certain variability in its parallelization configurations. A pure MPI approach utilizing as many CPUs as possible seems at first glance to be the best choice. However, this choice is everything else but numerical efficient. In the case of a 4×4 domain with one MPI task, the CPU calculates 16 grid points. If four MPI tasks are utilized, each CPU calculates four grid points. If the MPI tasks are increased even further to 16, each CPU calculates only one grid point. A nearly linear speed-up is assumed because the workload per CPU reduces linearly besides the CPU distributing the MPI tasks. But, the CPUs apply distributed memory and can not access information from the grid points outside of their patch next to them. Suppose a halo region of only one grid point in each direction is applied, four MPI tasks demand 32 grid points to be communicated, and the even more parallelized case with 16 MPI tasks already demands 64 grid points to be communicated. Thus, the computation time per CPU reduces drastically, but also its idle time increases while communication is processed.

If communication slows the simulations, a pure OpenMP approach seems the perfect way to go. Indeed, if one MPI task with 64 OpenMP threads is applied, no computational resource loss due to communication occurs. However, only one CPU out of 16 accessible ones is utilized, which slows the simulation down due to physical limitations from the CPU architecture, such as limited connections to the memory. Also, the CPUs usually process only two or four OpenMP threads simultaneously what, in turn, causes idle times of OpenMP threads. Generally, both individual parallelization approaches underperform compared to a mixture of them. However, the specific ratio of MPI

Table 2: Performance of different parallel configurations on the utilized high-performance computing systems *juqueen*, *juwels*, and *jureca*. Within this table, MPI represents the number of tasks per node, and OpenMP represents the number of threads per MPI task. The average time required for an iteration of the simulation is given by T. An individual case is chosen for each system to represent the majority of its workload best. The utilized configuration per system is highlighted in bold.

juqueen			*juwels*			*jureca*		
MPI	OpenMP	T [s]	MPI	OpenMP	T [s]	MPI	OpenMP	T [s]
1	64	2.32	1	48	1.05	1	48	11.94
2	32	2.15	2	24	0.54	2	24	11.19
4	**16**	**2.07**	3	16	0.53	3	16	10.24
8	8	2.02	4	12	0.51	4	12	8.98
16	4	2.14	6	8	0.43	6	8	8.68
32	2	2.51	8	6	0.37	8	6	8.24
			12	**4**	**0.36**	**12**	**4**	**7.95**
			16	3	0.37	16	3	8.20
			24	2	0.41	24	2	8.56

tasks to OpenMP threads varies beyond different HPC systems, depending on the CPU architecture as well as other hardware characteristics, such as memory latency. Therefore, the first performance tests (Tab. 2) on the three utilized HPC systems aim on the identification of the optimal ratio between MPI tasks and OpenMP threads.

A performance boost of 20 % is commonly reachable compared to a somehow randomly chosen or default configuration. On *juqueen*, not the optimum regarding the time required for one simulation iteration is utilized (Tab. 2). Instead, a similar performant configuration with less MPI tasks is chosen, which takes considerably less time for reading and writing data and therefore is more performant overall. These performance tests are only exemplary, and the chose configuration is not necessarily the most performant configuration for each simulation conducted on the individual HPC system.

Numerical Scaling Numerical scaling is an important measure of how efficient a model runs on HPC systems and is divided into strong and weak scaling. To test strong scaling, different numbers of CPUs solve the same problem, here a given domain size s_0. Starting with the smallest number n_0 of CPUs that can work on this problem, an increase of the CPUs by the scaling factor κ should ideally result in a speed-up ξ_{strong} of the same factor for the iteration time T because the workload per CPU gets reduced. This statement is equivalent to a scaling efficiency $\varepsilon_{\text{strong}}$ equal to one

$$\xi_{\text{strong}} = \frac{T_{n_0}^{s_0}}{T_{\kappa n_0}^{s_0}} \quad \text{and} \quad \varepsilon_{\text{strong}} = \frac{T_{n_0}^{s_0}}{\kappa T_{\kappa n_0}^{s_0}}. \tag{36}$$

Table 3: Strong scaling efficiency $\varepsilon_{\text{strong}}$ on the utilized high-performance computing systems *juqueen*, *juwels*, and *jureca*. The setups and configurations from Tab. 2 are chosen and κ is the scaling factor.

juqueen		*juwels*		*jureca*	
κ	$\varepsilon_{\text{strong}}$	κ	$\varepsilon_{\text{strong}}$	κ	$\varepsilon_{\text{strong}}$
1	1.00	1	1.00	1	1.00
2	0.98	2	0.98	2	1.04
4	0.90	4	0.91	4	1.01
8	0.84	8	0.89	8	0.95
16	0.75	16	0.86	12	0.86
32	0.65	32	0.80		
64	0.51	64	0.75		
		96	0.73		

To test weak scaling, the workload per CPU, here the patch size, stays constant. Again, the number of CPUs increases by a factor of κ and, because the workload per CPU remains constant, the domain size increases proportionally. Ideally, the corresponding speed-up equals one like the scaling efficiency because of the unchanged workload.

Ideal strong and weak scaling can only be achieved for a program, which is completely parallelized and where communication happens instantaneously. But, the CPU architecture can even favor scaling efficiencies better than the ideal ones, for instance, caused by cached memory. Generally, weak scaling is achieved easier than strong scaling because it mainly depends on how much of the calculations are serial and how much are parallel. Contrary, for strong scaling, at some point communication overhead becomes an issue because data communication usually increases leastwise linearly to the number of CPUs. Thus, the time required for communication increases while the speed-up in calculation is also at best only linear.

Strong scaling efficiency is excellent for the chosen configurations up to $\kappa = 8$ (Tab. 3). Also, several higher scaling factors still show a good performance, especially considering that no further optimization is applied. While Tab. 3 gives an excellent overview of how the individual configurations scale, it offers no comparison between the different configurations because different setups and grids are used. To give such a comparison, in Fig. 12, the strong scaling is related to the number of grid points each CPU has to calculate. By this, the effects of grid size and utilized CPUs are excluded, which allows to estimate performance loss due to MPI communication and the computational overhead resulting from the halo grid points. Thereby, *juwels* performs best and shows a nearly linearly—though not perfect—strong scaling up to less than 1 000 grid points per CPU. Contrary to *juwels*, *juqueen* experiences a non-linear decrease in strong

scaling below about 10 000 grid points per CPU. A similar trend seems to start around 3 000 grid points per CPU on *jureca*, but it can not be confirmed because no further scaling is analyzed.

2.3 Inclusion of Subsidence

The LES mode of WRF 4 considers no large-scale subsidence as a parametric input. Instead, it offers nudging by dynamical downscaling from larger-scale simulations, for instance, via nesting or external input data (Skamarock et al., 2019). However, semi-idealized LES studies like the presented ones require information on this parameter and can not be driven by large-scale simulation. In agreement with earlier work (Yamaguchi and Feingold, 2012), I implemented such a corresponding parameter.

There are two options to implement the effects of large-scale subsidence: first, within WRFs dynamical core, and second, as a physical module. Both options come along with benefits and drawbacks. The modification of the dynamical core is prone to errors due to its complexity and various available advection schemes and modules. Also, keeping the core numerical efficient is important for efficient numerical simulation. Therefore, large-scale subsidence is implemented via a dedicated physical module. The major drawback of this method is that the resulting tendencies remain constant during the Runge–Kutta integration. However, this holds for all parameterization and shall produce only negligible uncertainties.

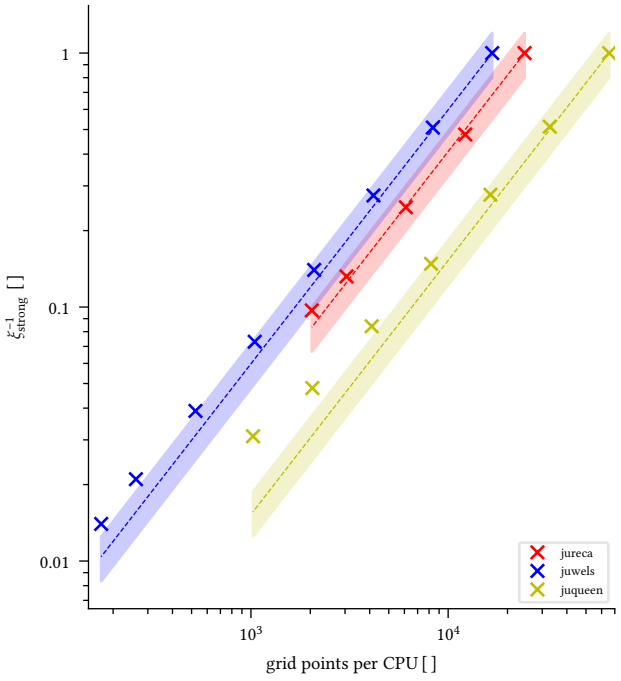

Figure 12: Strong scaling speed-up ξ_{strong} on the utilized high-performance computing systems *juqueen*, *juwels*, and *jureca*. The shaded area represents a corridor of 20 % from the ideal scaling in which the scaling is considered excellent.

Below, first, the necessary modifications to the prognostic set of equations of WRF 4 are presented (Section 2.3.1). Indeed, this part is valid for both options. Subsequently, the necessary numerical modifications to the source code are described (Section 2.3.2) as well as theoretical considerations of the newly implemented physical module, which is given in Appendix A. In the case of a dynamical implementation, a temporary modification of the vertical velocity during the advective integration is probably the way to go.

2.3.1 Physical Derivation

The inclusion of large-scale subsidence $\tilde{w}$ is achieved by adding it to the vertical cartesian velocity w in every prognostic equation (Eq. 17a–17g). Therefore,

$$w \mapsto w + \tilde{w} \tag{37}$$

is applied. Thus, the continuity equation (Eq. 17e),

$$\partial_t \mu_\mathrm{d} + \nabla \cdot \mu_\mathrm{d} \mathbf{v} = 0, \tag{38}$$

maps to

$$\partial_t \mu_\mathrm{d} + \nabla \cdot \mu_\mathrm{d} \mathbf{v} = -\mu_\mathrm{d} \partial_z \tilde{w} \tag{39}$$

because $\partial_z \mu_\mathrm{d} = 0$ for the pure sigma coordinate (Eq. 20).

All prognostic equations which utilize w only in a flux-advection term experience identical modifications to their source and sink terms caused by $\tilde{w}$. Below, these changes are exemplary derived for the prognostic equation of θ_m (Eq. 17d):

$$\partial_t \mu_\mathrm{d} \theta_\mathrm{m} + \nabla \cdot \mu_\mathrm{d} \mathbf{v} \theta_\mathrm{m} = F_{\mu_\mathrm{d}\theta_\mathrm{m}} \tag{40}$$

$$\overset{\text{Eq. 37}}{\longmapsto} \quad \partial_t \mu_\mathrm{d} \theta_\mathrm{m} + \nabla \cdot \mu_\mathrm{d} \mathbf{v} \theta_\mathrm{m} = F_{\mu_\mathrm{d}\theta_\mathrm{m}} - \partial_z \mu_\mathrm{d} \tilde{w} \theta_\mathrm{m} \tag{41}$$

$$\overset{\partial_z \mu_\mathrm{d} = 0}{\Longleftrightarrow} \quad \partial_t \mu_\mathrm{d} \theta_\mathrm{m} + \nabla \cdot \mu_\mathrm{d} \mathbf{v} \theta_\mathrm{m} = F_{\mu_\mathrm{d}\theta_\mathrm{m}} - \mu_\mathrm{d} \tilde{w} \partial_z \theta_\mathrm{m} - \mu_\mathrm{d} \theta_\mathrm{m} \partial_z \tilde{w} \tag{42}$$

$$\Longleftrightarrow \quad \mu_\mathrm{d} \partial_t \theta_\mathrm{m} + \mu_\mathrm{d} \mathbf{v} \cdot \nabla \theta_\mathrm{m} = F_{\mu_\mathrm{d}\theta_\mathrm{m}} - \mu_\mathrm{d} \tilde{w} \partial_z \theta_\mathrm{m} - \theta_\mathrm{m} \left(\partial_t \mu_\mathrm{d} + \nabla \cdot \mu_\mathrm{d} \mathbf{v} + \mu_\mathrm{d} \partial_z \tilde{w} \right) \tag{43}$$

$$\overset{\text{Eq. 39}}{\Longleftrightarrow} \quad \mu_\mathrm{d} \partial_t \theta_\mathrm{m} + \mu_\mathrm{d} \mathbf{v} \cdot \nabla \theta_\mathrm{m} = F_{\mu_\mathrm{d}\theta_\mathrm{m}} - \mu_\mathrm{d} \tilde{w} \partial_z \theta_\mathrm{m} \tag{44}$$

$$\overset{\text{Eq. 17e}}{\Longleftrightarrow} \quad \partial_t \mu_\mathrm{d} \theta_\mathrm{m} + \nabla \cdot \mu_\mathrm{d} \mathbf{v} \theta_\mathrm{m} = F_{\mu_\mathrm{d}\theta_\mathrm{m}} - \mu_\mathrm{d} \tilde{w} \partial_z \theta_\mathrm{m} \tag{45}$$

The last two steps apply first the modified continuity equation and afterward its

unmodified counterpart. While the former step is a physical transformation of the equation, the latter is only relevant for WRF's dynamics and can also be performed directly on the initally proposed equations, before the inclusion of subsidence, to transform them from flux-form to advection-form equations.

The prognostic equation of geopotential

$$\partial_t \phi + \mathbf{v} \cdot \nabla \phi - g w = 0 \tag{46}$$

is proposed as an advection-form equation. Substituting the modified vertical cartesian velocity results in

$$\partial_t \phi + \mathbf{v} \cdot \nabla \phi - g w = g \tilde{w} - \tilde{w} \partial_z \phi. \tag{47}$$

Although the prognostic equation for w

$$\partial_t \mu_\mathrm{d} w + \nabla \cdot \mu_\mathrm{d} \mathbf{v} w - g \left(\alpha / \alpha_d \partial_\eta p - \mu_\mathrm{d} \right) = F_{\mu_\mathrm{d} w} \tag{48}$$

utilizes w only in its flux-advection term, it differs from the other advective-flux form equations because of a non-linear expression. Applying the modified vertical velocity (Eq. 37) yields

$$\partial_t \mu_\mathrm{d} \left(w + \tilde{w} \right) + \left(\nabla \cdot \mu_\mathrm{d} \mathbf{v} + \partial_z \mu_\mathrm{d} \tilde{w} \right) \left(w + \tilde{w} \right) - g \left(\alpha / \alpha_d \partial_\eta p - \mu_\mathrm{d} \right) = F_{\mu_\mathrm{d} w}. \tag{49}$$

Here, the modified continuity equation (Eq. 39) is applied two times: once multiplied by w and once multiplied by $\tilde{w}$. Large-scale subsidence is a parameter, which is constant in time and therefore $\partial_t \tilde{w} = 0$. In turn, the modified prognostic equation for w reduces to

$$\mu_\mathrm{d} \partial_t w + \mu_\mathrm{d} \mathbf{v} \nabla w - g \left(\alpha / \alpha_d \partial_\eta p - \mu_\mathrm{d} \right) = F_{\mu_\mathrm{d} w} - \mu_\mathrm{d} \mathbf{v} \nabla \tilde{w} - \tilde{w} \partial_z \mu_\mathrm{d} w - \tilde{w} \partial_z \mu_\mathrm{d} \tilde{w}. \tag{50}$$

Recapping that $\partial_z \mu_\mathrm{d} = 0$ and assuming $\partial_x \tilde{w} = \partial_y \tilde{w} = 0$ yields

$$\mu_\mathrm{d} \partial_t w + \mu_\mathrm{d} \mathbf{v} \nabla w - g \left(\alpha / \alpha_d \partial_\eta p - \mu_\mathrm{d} \right) = F_{\mu_\mathrm{d} w} - \mu_\mathrm{d} \left(w \partial_z \tilde{w} + \tilde{w} \partial_z w + \tilde{w} \partial_z \tilde{w} \right). \tag{51}$$

The assumption of the absence of horizontal advection of $\tilde{w}$ is only an approximation. Indeed, the assumption is correct for a cartesian height coordinate but not for the applied sigma coordinate, which follows the terrain. However, the terrain is assumed to be flat in the presented studies, and therefore, the assumption shall be valid. Never-

theless, WRF 4 adjusts the model level heights during the simulations, which leads to negligible uncertainties. Applying the initially proposed continuity equation (Eq. 17e), as it is done for the prognostic equation for θ_m, results in the final expression

$$\partial_t \mu_\mathrm{d} w + \nabla \mu_\mathrm{d} \mathbf{v} w - g\left(\alpha/\alpha_d \partial_\eta p - \mu_\mathrm{d}\right) = F_{\mu_\mathrm{d} w} - \mu_\mathrm{d}\left(w\partial_z \tilde{w} + \tilde{w}\partial_z w + \tilde{w}\partial_z \tilde{w}\right). \tag{52}$$

To summarize, the modifications to the prognostic equations (Eq. 17a–17g) are written as:

$$F_{\mu_\mathrm{d} u} \longmapsto F_{\mu_\mathrm{d} u} - \mu_\mathrm{d} \tilde{w}\partial_z u \tag{53}$$

$$F_{\mu_\mathrm{d} v} \longmapsto F_{\mu_\mathrm{d} v} - \mu_\mathrm{d} \tilde{w}\partial_z v \tag{54}$$

$$F_{\mu_\mathrm{d} w} \longmapsto F_{\mu_\mathrm{d} w} - \mu_\mathrm{d}\left(w\partial_z \tilde{w} + \tilde{w}\partial_z w + \tilde{w}\partial_z \tilde{w}\right) \tag{55}$$

$$F_{\mu_\mathrm{d} \theta_\mathrm{m}} \longmapsto F_{\mu_\mathrm{d} \theta_\mathrm{m}} - \mu_\mathrm{d} \tilde{w}\partial_z \theta_\mathrm{m} \tag{56}$$

$$\partial_t \mu_\mathrm{d} + \nabla \cdot \mu_\mathrm{d} \mathbf{v} = -\mu_\mathrm{d} \partial_z \tilde{w} \tag{57}$$

$$\partial \phi + \mathbf{v} \cdot \nabla \phi - g w = g\tilde{w} - \tilde{w}\partial_z \phi \tag{58}$$

$$F_{\mu_\mathrm{d} \chi} \longmapsto F_{\mu_\mathrm{d} \chi} - \mu_\mathrm{d} \tilde{w}\partial_z \chi \tag{59}$$

The existing source terms are modified by adding the tendencies arising from $\tilde{w}$.

Frequently, no explicit expression or measure for $\tilde{w}$ is given. Analogous to Stevens et al. (2005), $\tilde{w}$ is defined here by assuming incompressibility and a constant horizontal divergence D_ls over the whole domain

$$D_\mathrm{ls} = \partial_x u + \partial_y v = -\partial_z \tilde{w} \quad \Longleftrightarrow \quad \tilde{w} = -\int_0^z D_\mathrm{ls}\,\mathrm{d}z' = -D_\mathrm{ls} z. \tag{60}$$

2.3.2 Numerical Implementation

Analogous to the implementation of a measure for $\overline{S}$ to the output files (Section 2.2.2), implementation of the effects of $\tilde{w}$ first demands a definition of the corresponding variables within the *registry (Registry.EM_COMMON)*:

```
state real rora_mu  ikj misc 1 - r "RORA_MU"  "mu tendency"  "Pa s-1"
state real rora_th  ikj misc 1 - r "RORA_TH"  "th tendency"  "K s-1"
state real rora_ph  ikj misc 1 - r "RORA_PH"  "ph tendency"  "m2 s-3"
state real rora_u   ikj misc 1 - r "RORA_U"   "u tendency"   "m s-2"
state real rora_v   ikj misc 1 - r "RORA_V"   "v tendency"   "m s-2"
state real rora_w   ikj misc 1 - r "RORA_W"   "w tendency"   "m s-2"
state real rora_qv  ikj misc 1 - r "RORA_QV"  "qv tendency"  "kg kg-1 s-1"
state real rora_qc  ikj misc 1 - r "RORA_QC"  "qc tendency"  "kg kg-1 s-1"
state real rora_qr  ikj misc 1 - r "RORA_QR"  "qr tendency"  "kg kg-1 s-1"
state real rora_qi  ikj misc 1 - r "RORA_QI"  "qi tendency"  "kg kg-1 s-1"
state real rora_qs  ikj misc 1 - r "RORA_QS"  "qs tendency"  "kg kg-1 s-1"
```

```
state real rora_qg  ikj misc 1 - r "RORA_QG"  "qg tendency"  "kg kg-1 s-1"
state real rora_qrn ikj misc 1 - r "RORA_QRN" "qrn tendency" "kg-1 s-1"
state real rora_qin ikj misc 1 - r "RORA_QIN" "qin tendency" "kg-1 s-1"
state real rora_qsn ikj misc 1 - r "RORA_QSN" "qsn tendency" "kg-1 s-1"
state real rora_qgn ikj misc 1 - r "RORA_QGN" "qgn tendency" "kg-1 s-1"
rconfig real rora_div namelist,physics 1 0.0 h "rora_div" "divergence [s-1]"
rconfig real rora_thg namelist,physics 1 0.0 h "rora_thg" "theta gradient [K m-1]"
```

These variables encompass changes to all prognostic equations (Eq. 17a–17g) with χ representing mixing ratios of water vapor, cloud water, rain, cloud ice, snow, and graupel and number concentrations of rain, cloud ice, snow, and graupel. The last two lines represent two parameters, which are added to the namelist[14] and can be accessed in top-level routines, for example, via *config_flags%rora_div*. They allow modifying D_{ls} and the model's upper potential temperature gradient without recompiling the model. While the former is an integral part of the parameterization, the latter is required to provide an upper boundary condition. Similar boundary conditions are, in principle, also necessary for the other variables, but those experience no considerable gradients at the model top in the presented studies and thus are ignored.

At the start of each simulation, the variables demand initialization because otherwise, their initial values are uncontrollable and might cause wrong initial tendencies. Initialization is done in the routine *phy_init(module_physics_init.F)* by calling the routine *rora_subsidence_init* of the new module(Appendix A). Both routines are no top-level routines, and the variables have to be passed through them to the top-level routine *start_domain_em (start_em.F)*, which calls the routine *phy_init*.

The routine *rora_subsidence* (Appendix A) fills the variables with their tendency values. It is called by the top-level routine *first_rk_step_part1 (module_first_rk_step_part1.F)*, which allows the corresponding variables to be stored on the *grid*. The routine *rora_subsidence* calculates and returns mass-decoupled physical tendencies of the individual prognostic variables and utilizes the Euler forward method for spatial discretization of each variable Ψ

$$-\tilde{w}\partial_z\Psi_{k_\mathrm{i}} = \frac{\Psi_m - \Psi_n}{z_m - z_n} Dz_{(m+n)/2} \quad \text{where } (m,n) = \begin{cases} (k_\mathrm{i}+1, k_\mathrm{i}) & D \geq 0 \\ (k_\mathrm{i}, k_\mathrm{i}-1) & \text{else} \end{cases} \tag{61}$$

with k_i the vertical level index. In the case of large-scale ascension, surface boundary conditions are required and kept zero because large-scale subsidence $\tilde{w}$ is negligi-

[14] WRF's namelist allows to set parameters for the simulation. These parameters include, among others, dynamic options, information on the domain size, and settings of the physical parameterizations. Changes in the namelist require no recompilation of the model but apply only for simulations (re-)started after the corresponding change.

bly small at the surface. Contrary, in the case of large-scale subsidence, boundary conditions at the top of the model are required. LES commonly estimates the free troposphere as a constant layer. Thus, the vertical gradients of the cartesian velocities u, v, and w as well as the vertical gradients of the moisture variables such as mixing ratios and number concentrations are kept zero, and only the vertical gradients for potential temperature and ϕ are required. The former is given by the namelist parameter *rora_thg*, and the latter is estimated as

$$\frac{\phi_{k+1} - \phi_k}{z_{k+1} - z_k} = \partial_z \phi = g. \tag{62}$$

The applied boundary conditions are only valid under the given circumstances, which are confirmed for the presented studies but not for general LES.

Within the top-level routine *first_rk_step_part2 (module_first_rk_step_part2.F)*, the here calculated tendencies get coupled to mass by a call to the routine *calculate_phy_tend (module_em.F)* and summed up with the other physical tendencies via a call to the routine *update_phy_ten (module_physics_addtendc.F)*. Both called routines are no top-level routines and demand the corresponding variables to be passed to them. The calculations in the routines are identical to the calculations other variables experience and require no further discussion.

Chapter 3

Model Evaluation by a Case of Subtropical Stratocumulus

The application of WRF-LES to a newly defined case implies many uncertainties at once. It complicates the identification and the analysis of inconsistencies, issues, and results because they can arise from the model, the implemented modifications, or the chosen case and how it is set up. I simulate and evaluate in this study a case that is already investigated in detail what allows model validation because uncertainties are limited to the model and the performed modifications. The case is based on the first research flight of the *Dynamics and Chemistry of Marine Stratocumulus Phase II* (DYCOMS-II) field campaign (Stevens et al., 2003a), henceforth called the DYRF01 case, and more straightforward than most Arctic Sc cases because of three reasons. First, turbulence is of a larger scale and more intense because surface fluxes over the warm Pacific Ocean are more than one order of magnitude stronger than those over ice and the ocean in the Arctic. Second, the lack of sunlight reduces the number of required physical parameterizations. Third, the absence of frozen hydrometeors and a non-precipitating Sc simplify the utilized microphysical parameterization. Several LES studies (Yamaguchi and Feingold, 2012; Matheou and Chung, 2014; Heinze et al., 2015; Pedersen et al., 2016; Pressel et al., 2017; Mellado et al., 2018) investigate the DYRF01 case and are based on the setup described in Stevens et al. (2005). They allow a detailed comparison and reveal if WRF-LES' outcomes yield a reasonable state of the investigated Sc.

The main objective of this study is to evaluate the capabilities of WRF-LES when applied to the DYRF01 case with varying horizontal resolution up to only a few meters. While it is possible to investigate sensitivities in process-level representation related to horizontal resolution or to perform a detailed comparison with other simulations, these are not topics of this study. However, the results of the sensibility study are comparable to those presented in Section 4.3. I strife for a rough comparison between

the individual resolved simulations and the results of Stevens et al. (2005). This comparison allows to identify fundamental issues of WRF-LES, arising, for instance, from the high horizontal resolution of only a few meters, the chosen combination of the utilized parameterization, or the implemented modifications. I start this chapter with a brief description of the DYRF01 case (Section 3.1) and present afterwards further modifications to WRF-LES, which are necessary to counteract erroneous behavior and to provide additional input parameters and output variables (Section 3.2). Concluding, I conduct a sensitivity study in Section 3.3, which covers one magnitude in horizontal resolution. The horizontal resolution sensitivity study allows to identify and counteract resolution-dependent model issues much easier for the presented case than for a newly defined case because the extensive amount of studies provide profound knowledge—not only on the case setup or its physical description (Stevens et al., 2005; Matheou and Chung, 2014; Heinze et al., 2015), but also on its process representation related to resolution (Pedersen et al., 2016; Mellado et al., 2018), specific peculiarities of WRF, or numerics in general (Yamaguchi and Feingold, 2012; Pressel et al., 2017).

3.1 Campaign and Case Description

The DYCOMS-II field campaign was carried out between the 7th and 28th of July, 2001, off the coast of southern California, and focused on the investigation of Sc CTE. Its objective was also to provide a suite of test cases for corresponding subsequent LES. Secondary objectives were testing a new technique for large-scale divergence measurements and evaluating effects of aerosols and precipitation on the cloud structure (Stevens et al., 2003a). Nine flights were performed during the DYCOMS-II field campaign of which most focused on CTE and followed the basic pattern described below. Seven of these flights were performed during the night, which greatly simplifies the dynamics and forcings of the ABL.

In-situ observations were conducted with the help of the *NCAR Hercules C130* and provide atmospheric state parameters as well as several trace gas, aerosol, and microphysical quantities. A lidar, radar, and radiometer were additionally equipped for remote sensing, as well as dropsondes (Stevens et al., 2003b). The flights investigating CTE followed a dedicated pattern (Stevens et al., 2003a, their Fig. 2) with long individual legs to reduce uncertainties due to sampling errors of turbulence quantities. The flight pattern consisted of several circular legs in and above the ABL, which were roughly 30 km in radius, and flown in opposing directions, each for about a half hour. Between these circular legs, profiles were flown within the ABL to gain information

on its vertical structure. In total, there were about eight circular legs and four to six profiles for each research flight (Stevens et al., 2003a).

The DYRF01 case is based on the first research flight performed on the 10$^{\text{th}}$ of July, 2001. A strengthening pacific high with a core pressure higher than 1025 hPa dominated the synoptic situation. In the upper atmosphere, the study area was influenced by the frontal zone of a weak trough whose warm-air advection formed a strong temperature inversion of about 10 K (Stevens et al., 2003c, their Fig. 1). Resulting lower-atmospheric winds were north–north-westerly with a strength of about $8\,\mathrm{m\,s^{-1}}$. The synoptic development can be tracked in Stevens et al. (2003a) and led to increasing ABL height and weakening temperature inversions throughout the following days. An intense decrease in moisture of about $-7.5\,\mathrm{g\,kg^{-1}}$ was observed above the ABL (Stevens et al., 2003c, their Fig. 1), which was caused by the combination of oceanic moisture source and strong large-scale subsidence induced by the pacific high.

The interest of the scientific community into the DYRF01 case is large, mainly because of two reasons. First, the thermodynamic atmospheric state and the sea surface temperature stayed remarkably constant, which suits semi-idealized numerical studies and robust observational statistics. Second, the observed Sc thickened while the environmental conditions favored cloud dissipation due to the strong moisture inversion and resulting buoyancy reversal instability (Stevens et al., 2003c). Stevens et al. (2005) define initial and boundary conditions for semi-idealized LES of this case. Their carefully designed LES intercomparison study holds as a reference for many subsequent studies. A two-layer structure is assumed for total water mixing ratio r_t and liquid-ice potential temperature θ_li where the ABL is well-mixed:

$$\theta_\mathrm{li} = \begin{cases} 289.0\,\mathrm{K} & z \le z_\mathrm{i} \\ 297.5\,\mathrm{K} + (z - z_\mathrm{i})^{1/3}\ \mathrm{K} & z > z_\mathrm{i} \end{cases} \tag{63}$$

$$r_\mathrm{t} = \begin{cases} 9.0\,\mathrm{g\,kg^{-1}} & z \le z_\mathrm{i} \\ 1.5\,\mathrm{g\,kg^{-1}} & z > z_\mathrm{i} \end{cases} \tag{64}$$

Here, $z_\mathrm{i} = 840\,\mathrm{m}$ is the estimated ABL height. My initial cloud profile is a purely diabatic approximation calculated from these profiles because no further information is given in Stevens et al. (2005).[15] The geostrophic wind is approximated with a single-layer structure and denotes $(u, v) = (7, -5.5)\ \mathrm{m\,s^{-1}}$. Further parameters such as surface

[15] The cloud profile is iteratively calculated by condensing and evaporating water and, in turn, adjusting the atmospheric temperature accordingly. The amount of condensation and evaporation is estimated via the current saturation water vapor pressure.

Table 4: Initialization and forcing parameters for the DYRF01 case and their reference or source. Although the surface roughness length is defined as an output variable, it is, in fact, a forcing parameter. But, its values are adjusted via Charnock's relation during the simulation. They are not known afore, which is why the presented values are estimated from the model output of case #03.5m (Tab. 5).

quantity	value	reference/source
surface albedo	0.08	surface property in WRF 4
surface temperature	292.5 K	Stevens et al. (2005)
surface roughness length	14×10^{-5} m	simulation output
mean sea level pressure	1017.8 hPa	Stevens et al. (2005)
latent heat flux	115 W m^{-2}	Stevens et al. (2005)
sensible heat flux	15 W m^{-2}	Stevens et al. (2005)
large-scale divergence	3.75×10^{-6} s^{-1}	Stevens et al. (2005)
cloud droplet concentration	150 cm^{-3}	Stevens et al. (2003a)

properties or the large-scale divergence are summarized in Tab. 4.

3.2 Model Adjustments

The initial modifications to the model account only for the missing feature of large-scale subsidence (Section 2.3). I encountered two additional problems while studying the DYRF01 case, which are discussed here: missing turbulence initialization at cloud top and occurence of numerical instability if time steps $\Delta t \ll 1$ s are applied. This section presents not only strategies for the avoidance and solution of both problems. Furthermore, it describes the inclusion of additional input parameters and output variables that simplify analysis and allow the model to utilize fixed surface heat fluxes as the lower boundary condition.

Turbulence Initialization at Cloud Top The default turbulence-seeding layer of the LES mode of WRF 4 adds a pseudo-randomized temperature perturbation field with values in the range of ±0.05 K to the four lowest model levels. This perturbation is constant within each column. It takes about 20 to 30 minutes for the shear-driven turbulence initiated at the surface to notably affect the whole ABL, and, only after one hour, the ABL can be considered to be well-mixed. Without additional turbulence seeding in the cloud, the cloud top may experience substantial artificial cooling due to radiation and thickening until shear-driven turbulence initiated at the surface reaches the cloud. In nature or a well-mixed state of the model, this phenomenon is counteracted by turbulent mixing due to the cloud-top instability. Two adjacent levels in the initialization file are modified to counteract this artificial behavior. These levels

are located within the upper half of the cloud. A second turbulence-seeding layer is added to one of them by adding a pseudo-randomized temperature perturbation field with values in the range of ±0.1 K. Additionally, the same perturbation with the opposite sign is added to the other level to approximately conserve the column mean temperature and the resulting amount of condensed water. This additional turbulence seeding causes the development of convectively driven turbulence in the cloud within a few minutes and does not falsify the outcomes of the simulation.[16]

Numerical Instability of Small Time Steps The highest resolved simulation applies $\Delta t \approx 0.1$ s. For such small time steps, the simulation aborts after a short execution period due to violation of the Courant–Friedrichs–Lewy (CFL) condition (Courant et al., 1967). Several tests on this phenomenon, for example minor changes to the time steps or different initial conditions, yield varying execution periods until abortion but can not overcome the phenomenon. Thereby, the execution periods vary by a factor much larger than and independent of the proposed changes.[17] A detailed look at the simulation data reveals a wave-like structure evolving in the x–z and y–z planes for various variables. This structure has a wavelength of only a few grid points and is visible already after a few seconds. It intensifies with advancing simulation until it forces abortion due to violation of the CFL condition.

These phenomena are an evidence of numerical instability and can arise for many reasons. Tests indicate the instability to crop up only if a microphysical parameterization is active.[18] A more detailed analysis discloses frequent calls to the microphysical parameterization to induce density–pressure waves, which intensify until they violate the CFL condition. These waves originate from the frequent changes in hydrometeor species and temperature and occur only for time steps much smaller than one second. For such small time steps, assumptions underlying most microphysical parameterizations become questionable. The time-split integration method (Section 2.2) enhances this problem because the fiercely varying information on hydrometeors and temperatures are not only kept constant throughout a Runge–Kutta integration cycle, but they are also estimates from the preceding time step.

[16] The corresponding code is added to WRF-LES' initialization routine by implementing two namelist parameters. It is also possible to directly modify the input files, which is why no additional discussion on the implementation is provided.

[17] For instance, reducing the time step aborts the simulation faster, but a further reduction of the time step prolongates the abortion of the simulation.

[18] The instability arises for all tested microphysical parameterizations (namelist options 1, 3, 4, 7, 10) and indicates a general problem. However, I neither tested all parameterizations before nor after the implemented fix.

The occurence of numerical instability caused by the described issue can only be avoided if the microphysical parameterization is called less frequent. WRF 4 provides no distinct microphysical time step. The only option is to apply a larger model time step, which is, in turn, constrained via the CFL condition. Together, both constraints allow no horizontal resolution on the order of a few meters. In turn, I modify WRF-LES and add a distinct microphysical time step that acts similar to the already existing radiative time step. This is not done here to speed up the calculation but to keep the simulation in a stable numerical regime. The microphysical time steps for these very highly resolved cases are similar to those used in a compressible LES code or that are routinely used in other time-split codes (Heinze et al., 2017). The modifications are performed within the last third of the top-level routine *solve_em (solve_em.F)* and demand addition of a namelist parameter *rora_dtmp* to the *registry (Registry.EM_COMMON)*:

```
rconfig real rora_dtmp namelist,physics 1 0.0 h "rora_dtmp" "time step for mp [s]"
```

The newly added namelist parameter contains information on the distinct microphysical time step. The modifications in the routine *solve_em* read:

```
...
if ( (grid%itimestep == 1) .OR. (config_flags%rora_dtmp <= 0.0) .OR.          &
   (mod(grid%itimestep,max(nint(config_flags%rora_dtmp/dtm),1)) == 1) ) then
  if(config_flags%rora_dtmp > 0.0) then
    rora_temp = config_flags%rora_dtmp
  else
    rora_temp = dtm
  end if
  || call to microphysical routines with rora_temp instead of dtm as time step ||
end if
...
```

The variables *dtm* and *rora_temp* are the model time step and a dummy variable containing the microphysical time step. The modified code encompasses all calls to the microphysical routines and overwrites the time step they work with. Although I expect the fix to work for all microphysical parameterizations, it is only tested for the utilized one. The first if-condition determines if the microphysical parameterization shall be called and is adapted from its radiative counterpart. The microphysical parameterization is called in three cases: if it is the first model time step (*itimestep=1*), if the default or a negative value of *rora_dtmp* is set, or if the time given by *rora_dtmp* has passed since the last call to the microphysical parameterization. The second if-condition sets the model's microphysical time step. If the default or a negative value for *rora_dtmp* is set, the microphysical parameterization is called every time step. Thus, the model time step and the microphysical time step equal each other. In all other cases, the microphysical time step equals the corresponding namelist parameter.

Input Parameter and Output Variables Stevens et al. (2005) provide distinct surface heat fluxes, which constrain the lower boundary condition of the simulations. Although WRF 4 provides a namelist option to utilize such a boundary condition, this option is not intuitive and allows only the definition of the heat transfer coefficients. I add a similar option to WRF-LES, which allows definition of the surface heat fluxes directly and utilizes the given information for calculations of the surface-layer parameterization (Section 2.2.2). The used *RRTMG Scheme* provides radiative fluxes for each model level. But, these variables are not stored in the output files and have a different dimension than other three-dimensional variables because they also store values for the surface and the top of the model. The radiative fluxes, however, provide helpful information on Sc–surface interactions and for the process-level understanding of CTE, which is why I add corresponding variables to the output.

The corresponding changes to the model code are straightforward compared to the implementation of the parameterization of large-scale subsidence (Section 2.3.2) and are only roughly outlined here.[19] Again, all variables require definition within the *registry (Registry.EM_COMMON)*:

```
state real rora_swu ikj misc 1 - - "SWUPFLX" "sw upward radiative flux" "W m-2"
state real rora_swd ikj misc 1 - - "SWDNFLX" "sw downward radiative flux" "W m-2"
state real rora_lwu ikj misc 1 - - "LWUPFLX" "lw upward radiative flux" "W m-2"
state real rora_lwd ikj misc 1 - - "LWDNFLX" "lw downward radiative flux" "W m-2"
rconfig integer rora_flx namelist,physics 1 0   h "rora_flx" "switch for fluxes []"
rconfig real    rora_lh  namelist,physics 1 0.0 h "rora_lh"  "latent heat [W m-2]"
rconfig real    rora_sh  namelist,physics 1 0.0 h "rora_sh"  "sensible heat [W m-2]"
```

Here, the first four lines add variables containing the radiative fluxes, and the last three lines provide namelist parameters that allow the definition of constant surface heat fluxes to constrain the lower boundary condition. The parameter *rora_flx* is a switch to enable or disable utilization of the provided heat fluxes.

The namelist parameters are passed from the top-level routine *first_rk_step_part1 (module_first_rk_step_part1.F)* through intermediate routines to the routine *sfclayrev1d (module_sf_sfclayref.F)* where the calculated heat fluxes are optionally overwritten by the corresponding namelist parameters.

The radiative flux variables are filled based on their larger-dimensionalized counterparts in the routines *rrtmg_swrad (module_ra_rrtmg_sw.F)* and *rrtmg_lwrad (module_ra_rrtmg_lw.F)*. Subsequently, the variables get passed through intermediate routines to the top-level routine *first_rk_step_part1*.

[19] The implemented changes work only with the specific parameterization selection described in Section 2.2.2.

3.3 Results

I present four cases of the DYRF01 case (Tab. 5). Three of them apply different horizontal resolutions—covering one magnitude from the lowest, which is 35 m, to the highest, which is 3.5 m. The fourth case also applies the lowest horizontal resolution of 35 m but quadruples the horizontal domain size in each direction. The main objective of this study resembles a feasibility study: evaluation of WRF-LES' capabilities to simulate Sc under well-known circumstances with settings which are similar to those applied in the later stages of this thesis. I focus on a comparison between the cases simulated with WRF-LES and the results presented in Stevens et al. (2005), henceforth referred to as benchmark ensemble. Their results are easily accessible and act as a benchmark for most simulations of the DYRF01 case. The comparison between both data is performed utilizing time-slab averaged measures of the third simulated hour. My data is calculated from full three-dimensional snapshots, which are stored every five minutes.[20] I also consult other studies and observations whenever reasonable.

3.3.1 Bulk Evolution of the Simulations

Here, I focus on the three different resolved cases with identical domain sizes. All cases produce, regardless of their horizontal resolution, appropriate atmospheric states with a non-precipitating Sc. Even more, the results of the individual cases vary only marginally among each other for most zero- and first-order quantities. Usually, they lie within or close to the corresponding standard deviation of the benchmark ensemble. The discussion below is limited to a selection of non-cloud quantities and cloud quantities, but the presented results fall in line with those which can be obtained by considering other quantities.

Table 5: Simulation settings and liquid water path LWP for the DYRF01 case. For the simulation settings $\Delta_{x,y}$ is the horizontal resolution, $N_{x,y} \times N_z$ are the number of grid points, and Δt_{ACC}, Δt, Δt_{MP}, and Δt_{R} are the time steps for the acoustic mode, fast physics, microphysics, and radiation.

	$\Delta_{x,y}$	$N_{x,y} \times N_z$	Δt_{ACC}	Δt	Δt_{MP}	Δt_{R}	LWP
#35.0m	35 m	$128^2 \times 207$	1/16 s	3/4 s	1.5 s	5.0 s	58.7 g m^{-2}
#10.0m	10 m	$448^2 \times 207$	1/56 s	1/4 s	1.0 s	3.0 s	53.3 g m^{-2}
#03.5m	3.5 m	$1280^2 \times 207$	1/168 s	1/12 s	0.5 s	2.0 s	54.8 g m^{-2}
#35.0m_l	35 m	$512^2 \times 207$	1/16 s	3/4 s	1.5 s	5.0 s	57.7 g m^{-2}

[20] Time series of the corresponding slab-averaged first three statistic moments and full three-dimensional snapshots at the initialization and end are accessible by contacting r.rauterkus@posteo.net

Non-Cloud Quantities The quantities θ_{li} and r_{t} are some of the major constraints to the initial atmospheric state. The simulated Sc heavily relies on them because they determine the amount of condensable water. Their profiles fit well to those of the benchmark ensemble for all cases and show the same main features (Fig. 13a,b). It is hard to distinguish between the individual cases, which indicates independency from horizontal resolution for the presented case. The results of WRF-LES differ from those of some benchmark ensemble members. For example, WRF-LES produces no dry bulge immediately above the ABL, as the light gray area indicates for some ensemble members in Fig. 13a at an altitude of about 900 m. This bulge also arises in my simulations if a non-monotonic advection scheme is utilized (Section 2.2), which indicates the bulge to be a purely numerical artifact as it is discussed by Pressel et al. (2017). If the bulge arises, a slight reduction of the simulated Sc is observed resulting from artificial drying of the ABL. Another feature separating the results of WRF-LES from the benchmark ensemble is that $\partial_z r_{\mathrm{t}}$ is closer to zero than its counterpart of the benchmark ensemble (Fig. 13a). The same feature is also marginally visible for $\partial_z \theta_{\mathrm{li}}$ (Fig. 13b) and indicates the ABL to be more turbulent than in the benchmark ensemble. However, these features are only barely visible and likely occur also in the results of individual benchmark ensemble members.

Contrary to θ_{li} and r_{t}, u and v show notable but small variations among the individual

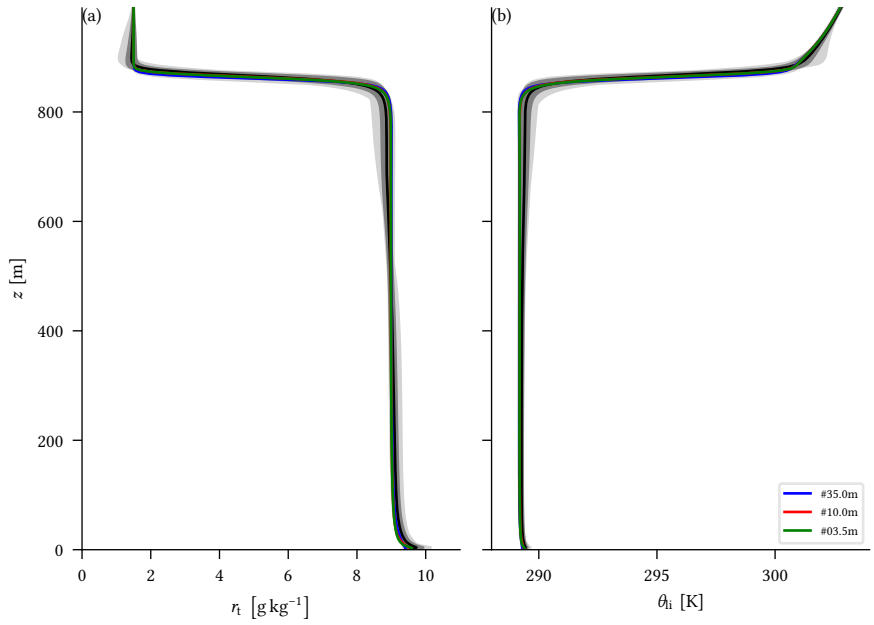

Figure 13: Comparison of total water mixing ratio r_{t} and liquid-ice potential temperature θ_{li} between the cases simulated by WRF-LES and the results presented in Stevens et al. (2005). The light gray area encompasses all values from the benchmark ensemble members, the dark gray area corresponds to their standard deviation, and the black line represents their mean.

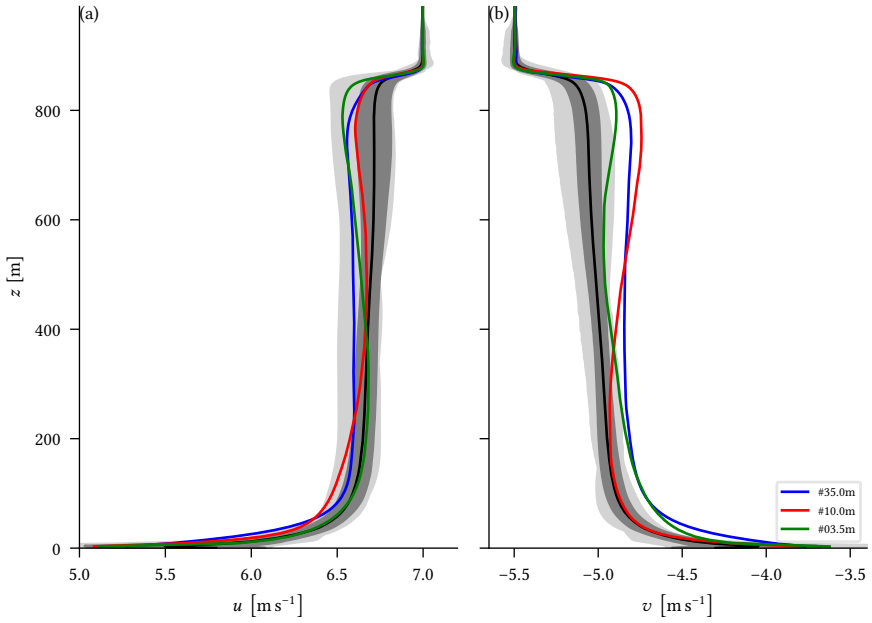

Figure 14: Comparison of zonal wind u and meridional wind v between the cases simulated by WRF-LES and the results presented in Stevens et al. (2005). The light gray area encompasses all values from the benchmark ensemble members, the dark gray area corresponds to their standard deviation, and the black line represents their mean.

cases (Fig. 14a,b). I expect these variations not to be a sign of dependence on the resolution here. The variations measure less than 10 % of their value, and I assume them to arise from slightly different structures of the circulation in the individual cases. The variations possibly weaken with advancing simulation or might average out over more extended periods. Different realizations of cloud or turbulent structures may cause them and are in the nature of LES. For instance, similar variations also occur if multiple simulations with the identical horizontal resolution are initialized with different turbulence initializations. Contrary to the variations among the individual cases, a distinct difference between all cases and the benchmark simulation is that the velocity jump at the ABL top is about two times larger in my simulations.

The last quantity I analyze in detail is TKE which I differentiate in an SGS and resolved part, TKE_s and TKE_r. Contrary to the quantities investigated so far, TKE is of second-order and more sensitive to changes in the model or resolution. However—with the exception of TKE_s in case #35.0m at the top of the ABL—once more, all cases show reasonable results and reproduce the main features simulated by the benchmark ensemble (Fig. 15). TKE increases with advancing simulation more in WRF-LES than in the benchmark ensemble (Fig. 15a). This higher TKE is caused by the turbulent evolution of the whole ABL and supports the observed weaker gradients of θ_li and q_t. In agreement with the benchmark ensemble, also in the presented cases, TKE_s

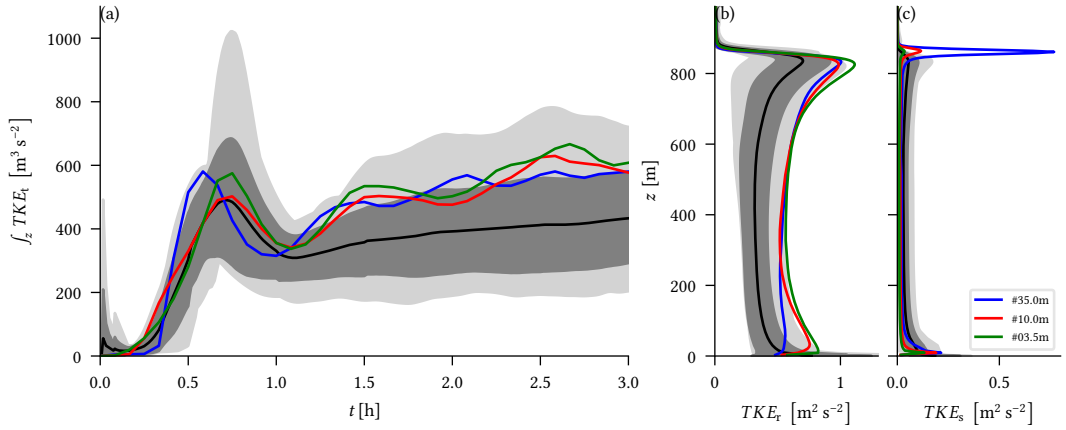

Figure 15: Comparison of the temporal evolution of vertically integrated total turbulent kinetic energy $\int_z TKE_t$ and profiles of its resolved part TKE_r and its sub-grid scale part TKE_s between the cases simulated by WRF-LES and the results presented in Stevens et al. (2005). The light gray area encompasses all values from the benchmark ensemble members, the dark gray area corresponds to their standard deviation, and the black line represents their mean.

accounts for most altitudes only for the minor fraction of TKE (Fig. 15b,c). Though, the share of TKE_s increases near the surface and is maximal at the interface between ABL and the free troposphere where the cloud top is located.

The maxima at the surface and top of the ABL in TKE_r and TKE_s and the increased share of TKE_s are a consequence of turbulence production due to strong vertical gradients on the one hand and suppression of turbulence by thermodynamic stability on the other hand. Although both phenomena counteract each other to a certain degree, their combination explains the observed characteristics: strong vertical and horizontal gradients produce turbulence, especially close to the surface and at the cloud top; the enhanced turbulence production causes in general more TKE; at the surface and the top of the ABL thermodynamic stratification hinders turbulent eddies to explicitly propagate and mix the layered atmosphere; the still persistent gradients, in turn, enhance SGS turbulence production and explain its increased share at these locations. The amount of TKE_s of case #35.0m at the top of the ABL deviates intensely from the other cases and the benchmark ensemble. The exact reasons for this deviation remain elusive at this point. Still, because the amount of TKE_r is comparable with the remaining data, the most likely cause is erroneous behaviour of the SGS parameterization. Considering the low horizontal resolution of 35.0 m and the assumptions and constraints of the utilized SGS parameterization (Section 2.2.2), indeed, indicate problems here.

Cloud Quantities Similar to the non-cloud quantities, WRF-LES also reproduces the main features of the benchmark ensemble for the investigated cloud quantities

(Fig. 16), for example, the absence of precipitation and persistence and thickening of the Sc. All cases produce a considerably thicker Sc than most of the benchmark ensemble members. The resulting liquid water mixing ratio η_l even exceeds the corresponding standard deviation of the benchmark ensemble for most altitudes but lies within the benchmark ensemble's extrema (Fig. 16b). The difference in cloud thickness appears throughout the whole simulation period and is roughly constant after the spin-up process (Fig. 16a). Thus, the thicker Sc in my results is likely a consequence of to an offset introduced at the beginning of the simulation. Similar offsets, positive and negative, also appear among individual benchmark ensemble members and arise from their initial cloud profiles, which are not defined by Stevens et al. (2005).

During the spin-up process, the Sc first thickens due to artificial radiative cooling at the cloud top, which is not counteracted by turbulence (Section 3.2). In turn, a temporary peak forms in the liquid water path LWP after about 20 minutes. Once cloud-induced turbulence sets in, caused by strong cloud-top instability, LWP decreases rapidly with time and approaches its natural state (Fig. 16a). I address the resulting artificial cooling in combination with and arising from the varying initial cloud profiles and microphysical parameterizations to be the main reason for the observed offsets in LWP. Once the Sc is turbulent, the observed offsets remain constant among all considered simulations.

WRF-LES simulates a sharper cloud-top boundary than the benchmark ensemble. Furthermore, the cloud maximum is located slightly lower. While the former is caused by the observed higher shear at the ABL's top (Fig. 14), the latter is a consequence of barely noticeable deviations between the thermodynamic states of WRF-LES and the

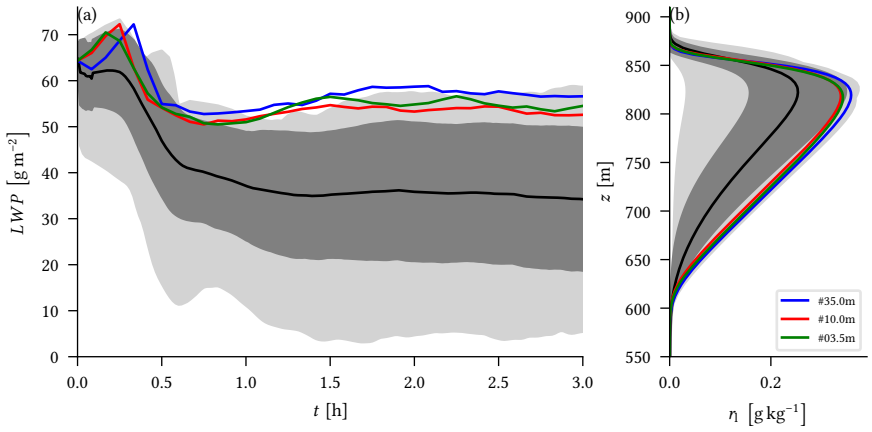

Figure 16: Comparison of the temporal evolution of liquid water path LWP and profiles of liquid water mixing ratio η between the cases simulated by WRF-LES and the results presented in Stevens et al. (2005). The light gray area encompasses all values from the benchmark ensemble members, the dark gray area corresponds to their standard deviation, and the black line represents their mean.

benchmark ensemble. A more detailed analysis of the simulations reveals θ_{li} and r_{t} to determine the observed differences. They are in the cloud layer, due to weaker vertical gradients, slightly colder and moister in WRF-LES than in the benchmark ensemble (Fig. 13). The corresponding differences are barely visible but strengthen exponentially for cloud quantities by adiabatic relations such as the Clausius–Clapeyron equation. Although most cloud quantities are extrema, compared to the reference ensemble, the overall atmospheric state is still reasonable. Even more, my simulations fit the observations better than those of the reference ensemble (Stevens et al., 2005) and also agree with the observed slight thickening of the Sc (Stevens et al., 2003a).

The evolution of cloud quantities differs between case #35.0m and the higher resolved cases #10.0m and #03.5m (Fig. 16b). This difference is present throughout the whole simulation period and increases with time (Fig. 16a), resulting in a decrease of about 8 % in LWP (Tab. 5). The decrease arises due to a slightly drier and warmer ABL in the higher resolved cases (Fig. 13). Again, while the thermodynamic differences are barely visible, they strengthen exponentially for cloud quantities. Below a horizontal resolution of $\Delta_{x,y} = 10\,\mathrm{m}$, my simulations indicate that the cloud quantities remain nearly constant, which is a sign for convergence of zero- and first-order quantities. Other quantities converge already at an even lower resolution in terms of their accuracy. I observe similar features also in the investigated Arctic case in Chapter 4, where I analyze their reasons and relate them to enhanced cloud-top entrainment. Here, however, such an analysis exceeds the scope of this study.

3.3.2 Sensitivity on Domain Size

The averaged cloud patch, a contiguous updraft region, seizes for all presented cases after a simulation period of 1.5 hours between one-fourth and half of the domain size.

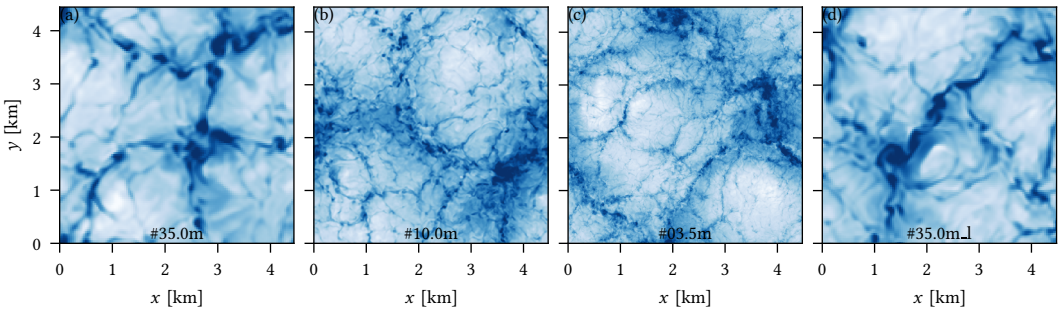

Figure 17: Instantaneous snapshots of liquid water path [$0\,\mathrm{g\,m^{-2}}$ (blue) to $100\,\mathrm{g\,m^{-2}}$ (white)] after three hours of simulation. From panel (a) to panel (c), the horizontal resolution increases. Panel (d) visualizes a corresponding dimensionalized cutout of case #35.0m_l that has increased domain size (Tab. 5).

These individual cloud patches are visible in Fig. 17 as contiguous white to white-blueish areas, surrounded by line-like deep blue structures. With advancing simulation, the averaged cloud patch size increases, if at all, only marginally (Fig. 17a–c). The stagnating average cloud patch size may result from constraints of the domain size. Indeed, the domain size hinders further growth because cloud patches can not be represented once they exceed the domain size. However, the stagnating average cloud patch size may also arise from physical reasons, such as the size of up- and downdrafts. If the average cloud patch size stagnates because of a physical or numerical reason is of general relevance. In the latter case, important cloud processes such as the largest up- or downdrafts are likely not captured by the corresponding simulation and cause erroneous results and physical misrepresentation.

To ensure this is not the case here, I provide case #35.0_l, which applies the coarsest resolution of 35 m and a domain size quadrupled into each direction. Similar studies for the finer resolved cases are possible as well but come with intense computational costs due to the finer grid spacing and the smaller time steps. Such studies provide only little additional knowledge to this topic because the effects resulting from the largest scales are investigated. Fig. 17d indicates that the stagnating average cloud patch size arises for physical reasons because the cloud patches in case #35.0 (Fig. 17a)

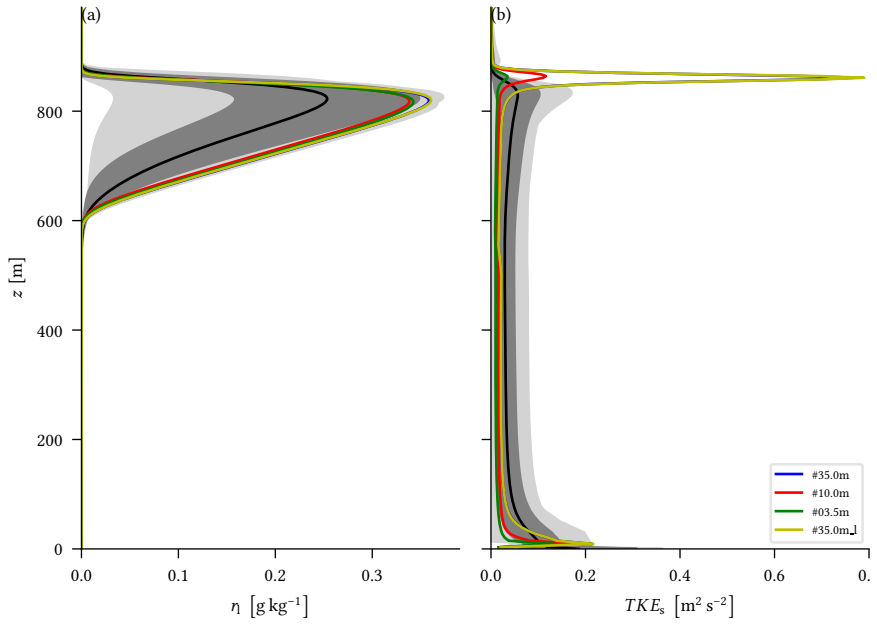

Figure 18: Comparison of liquid water mixing ratio η and sub-grid scale turbulent kinetic energy TKE_s between the cases simulated by WRF-LES and the results presented in Stevens et al. (2005). The light gray area encompasses all values from the benchmark ensemble members, the dark gray area corresponds to their standard deviation, and the black line represents their mean. The cases #35.0m and #35.0m_l share the horizontal resolution, but the latter has an increased domain size compared to all other cases (Tab. 5).

and case #35.0_l (Fig. 17d) seize roughly the same. Furthermore, also for the larger domain the average cloud patch size changes only marginally after 1.5 hours. If the domain size would be the limiting factor to the cloud patch size, this stagnation would occur later in time when the cloud patches are larger. This observation is supported by the profiles zero-, first-, and higher-order quantities that differ less than 1 % between the identical resolved cases #35.0 and #35.0m_l as Fig. 18 exemplifies for the highly sensitive quantities r_l and TKE_s.

Chapter 4

Process-Level Representation of Arctic Stratocumulus

[21] Chapter 3 demonstrates that the modified WRF-LES is not only capable of simulating maritime liquid-only Sc during night—even at resolutions of only a few meters. Indeed, the model reproduces the results of former studies of the DYRF01 case and thereby indicates higher horizontal resolution to intensify CTE. The reasons for the intensified CTE are not further investigated in that study. However, its sensibility to horizontal resolution indicates that driving processes are underrepresented or non-resolved on too coarse horizontal grids. Here, I extend the investigations described in Chapter 3 in three ways: I transfer the idea of applying highly-resolved isotropic grids to an Arctic Sc case, investigate if CTE also shows a resolution dependence for this case, and perform a detailed analysis of the processes driving CTE.

To achieve these objectives, I define a new benchmark case of Arctic Sc over ice during spring. While the chosen case is inspired by observations from two recent campaigns, ACLOUD and PASCAL, a best-possible reconstruction of these observations is not the primary goal of this work. Instead, I strive for a realistic setup that can be used as a benchmark case—and that can in principle be validated by observation—wherein to study cloud-driving processes. I start this chapter with a description of the benchmark case, henceforth called ACRF13 case. Next, I discuss further modifications implemented to WRF-LES (Section 4.2). These modifications are rather small because the model is developed and debugged in the preceding chapters. The applied modifications are limited to the inclusion of additional variables to allow for a more detailed investigation of CTE. Concluding, I conduct and analyze a resolution-sensitivity study for the ACRF13 case similar to the one performed in Section 3.3.

[21] Large parts of this chapter, especially Sections 4.1 and 4.3 and its subsections, are excerpts of Rauterkus and Ansorge (2020). As the first author, I simulated and evaluated the presented cases. Also, the major work on the manuscript was performed by me—discussions of the presented results and the manuscript, as well as guidance in day-to-day work, were provided by Cedrick Ansorge.

4.1 Campaign and Case Description

The campaigns ACLOUD and PASCAL were carried out near Svalbard between May 23rd and June 26th, 2017, and focused on the Arctic ABL, in particular on clouds and their interaction with the surface. The Variety and topicality of these observations set an ideal basis to define a benchmark case for the investigation of Arctic mixed-phase Sc. I use here data from two research aircraft (*Polar 5*, *Polar 6*), one research vessel (*RV Polarstern*), and ground-based observations. Wendisch et al. (2019) give a summary of the first results and more detailed information on both campaigns and the instruments used. The radiosounding and aircraft data used in this work are described by Ehrlich et al. (2019), and aircraft data on mean and turbulent meteorological quantities are made available by Hartmann et al. (2019). Knudsen et al. (2018) complement this campaign overview with a summary of the observed synoptic development.

I define the benchmark case based on June 05th, 2017 (Wendisch et al., 2019, their Fig. 18). It covers the period between two radiosoundings (Schmithüsen, 2017a,b), launched around 11 UTC and 17 UTC from *RV Polarstern*. The case lies within the second synoptic key period, as identified by Knudsen et al. (2018). *Polar 5* and *Polar 6* performed the research flight ACLOUD RF13 and flew multiple parallel triangular patterns close to *RV Polarstern* within, beneath, and above the cloud around 12 UTC (Ehrlich et al., 2018a,b). Fig. 19 sets the observations in relation to the position of RV Polarstern and gives more detailed information about the location and time of the measurements I refer to. Further, it shows the low-level cloud deck in the ERA5 reanalysis (European Centre for Medium-Range Weather Forecasts, 2017) which observations confirm and identify as mostly liquid mixed-phase Sc between 100 m and 500 m altitude.

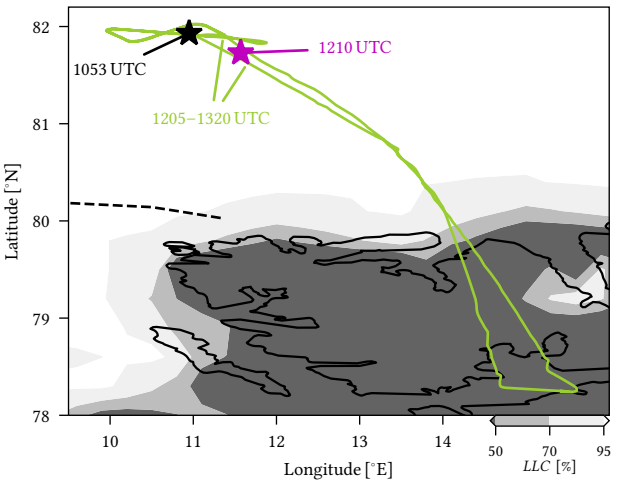

Figure 19: Study area and flight path of Polar 6 during ACLOUD RF13. The shading represents low-level cloud cover [white > 95 %, dark grey < 50 %], and the dashed line contours 50 % sea-ice coverage (where coverage increases northward), both derived from ERA5 at 11 UTC. The observations shown in Fig. 20 are also symbolized: the green line represents the flight track of *Polar 6*, the pink star marks the coordinates of the dropsonde (started from *Polar 5*), and the black star marks the coordinates of *RV Polarstern* where the radiosoundings were started and my simulation is placed.

As mentioned above, a best-possible convergence to the observations is not the objective of this study. Instead, I rather focus on the representation and sensitivity of processes driving Sc under realistic conditions. Thus, the initialization profiles of liquid-ice potential temperature θ_{li} and total water mixing ratio r_{t} are an idealized approximation of the 11 UTC radiosounding, also taking other observations into account:

$$\theta_{\mathrm{li}} = \begin{cases} 268.65\,\mathrm{K} & z \leq z_{\mathrm{i}} \\ 271.95\,\mathrm{K} + \left(\frac{z - z_{\mathrm{i}}}{1\,\mathrm{m}}\right)^{0.33}\,\mathrm{K} & z > z_{\mathrm{i}} \end{cases} \tag{65a}$$

$$r_{\mathrm{t}} = \begin{cases} 2.6\,\mathrm{g\,kg^{-1}} & z \leq z_{\mathrm{i}} \\ 1.8\,\mathrm{g\,kg^{-1}} & z > z_{\mathrm{i}} \end{cases} \tag{65b}$$

where $z_{\mathrm{i}} = 470\,\mathrm{m}$ is the estimate for ABL height.

Fig. 20 illustrates observed potential temperature θ and water vapor mixing ratio r_{v} as compared to those calculated from Eq. (65a)–(65b) assuming a moist-adiabatic cloud and well-mixed ABL. The radiosounding indicates weak horizontal wind in the lowest kilometer of the atmosphere whose components I approximate as $u = 1.5\,\mathrm{m\,s^{-1}}$ as the zonal and $v = -0.6\,\mathrm{m\,s^{-1}}$ as the meridional component. The surface properties of the simulated cases are given in Tab. 6, along with a reference or data source, respectively. Contrary to the other parameters in this table, the latent and sensible heat fluxes are not input parameters but instead calculated via the surface parameterization mentioned in Section 2.2.2. They vary locally and temporally throughout the simulations and also show slight differences between each simulation. However, these differences are less than $1\,\mathrm{W\,m^{-2}}$ and can be estimated from the data provided in Rauterkus and Ansorge (2019). Observational data of atmospheric heat fluxes is described by Egerer et al. (2019) (their Fig. 11) and supports the weak positive surface fluxes.

Table 6: Initialization parameters and their reference or source for the ACRF13 case.

quantity	value	reference/source
surface albedo	0.85	Stapf et al. (2019)
surface temperature	272.05 K	Stapf et al. (2019)
surface roughness length	10^{-3} m	surface property in WRF
mean sea level pressure	1022 hPa	Schmithüsen (2017a)
latent heat flux	$11.5\,\mathrm{W\,m^{-2}}$	simulation output
sensible heat flux	$11.1\,\mathrm{W\,m^{-2}}$	simulation output
large-scale divergence	$1.3 \times 10^{-5}\,\mathrm{s^{-1}}$	ERA5 output

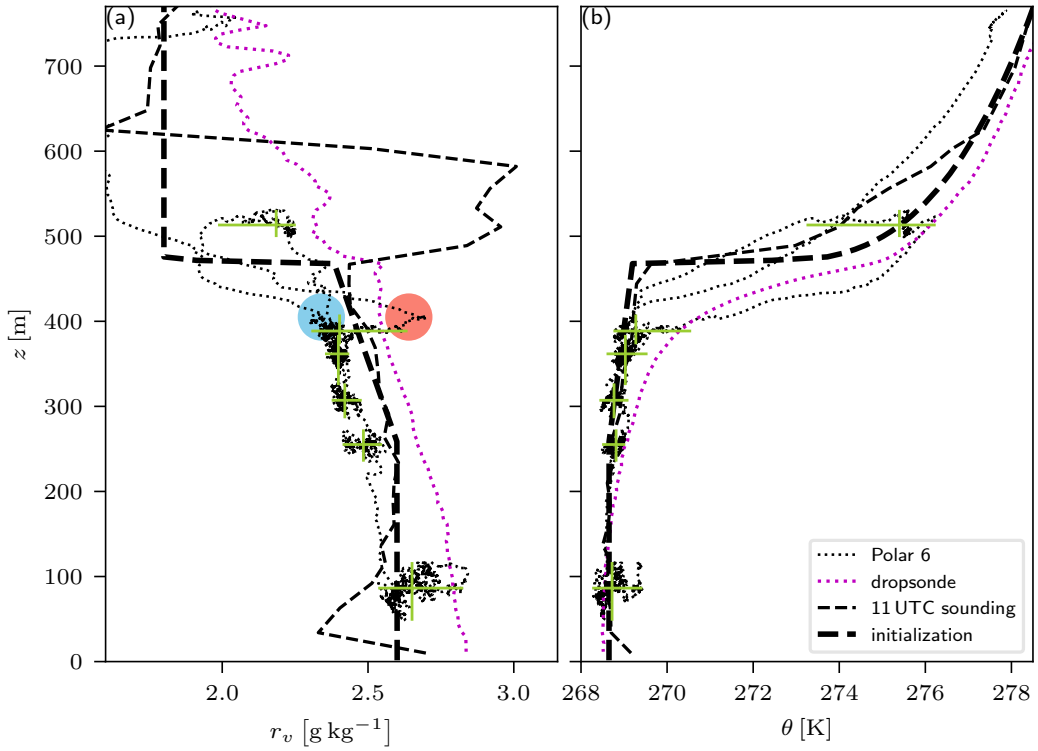

Figure 20: Observations and initial profiles of (a) water vapor mixing ratio r_v and (b) potential temperature θ. The green error bars mark the minimum and maximum of individual *Polar 6* flight legs (lowest leg below cloud, highest leg above cloud, other legs within cloud). The transparent red and blue dot encircle ascents or descents where the moisture inversion was observed or not observed by *Polar 6*. The measurements from *Polar 6* are not single-valued due to multiple ascents and descents in the flight pattern.

Measurements are ambiguous regarding the presence of a moisture inversion above or near the top of the ABL. Even data of single methods do not allow for a definite conclusion regarding the existence or absence of such an inversion (red and blue dot in Fig. 20a). It thus remains open whether or not the moisture inversion (around $z \approx 400\,\mathrm{m}$ in airplane data and around $z \approx 500$–$600\,\mathrm{m}$ in the radiosounding) is an observational artifact (Dirksen et al., 2014), a local-, or a large-scale phenomenon as it may occur in the Arctic (Naakka et al., 2018). Recent LES studies indicate that a moisture inversion may evolve when Sc decouples from the surface. In this decoupled state of Sc, precipitation may lead to a drying of the ABL and, therefore, may form a moisture inversion above (Neggers et al., 2019). However, all observations related to the ACRF13 case and my corresponding simulations indicate a well-mixed ABL up to the cloud top. This well-mixed state ensures vertical propagation of air masses from the surface to the Sc and, therefore, outlines the coupling between both. Thus, I decide to proceed without a specified moisture inversion in the initial condition, which is consistent with several *Polar 6* samples and the dropsonde.

I do not expect this interpretation of observational data to affect the results on process-level representativity. While I do expect different moisture fluxes, LES of Arctic Sc seems to differ at the quasi-equilibrium state only if no moisture source is available at all (Solomon et al., 2014). In this benchmark case, however, the surface latent heat flux provides moisture, and the Sc is located much closer to the surface than the one studied in Solomon et al. (2014). Additionally, Mellado et al. (2017) showed analytically for a cloud-free convective ABL that the moisture flux through the entrainment layer needs to be of similar magnitude and opposite sign to the one at the surface to have a drying effect on the ABL. This is not the case here because, in this benchmark case, the magnitude of the moisture flux at the inversion is much smaller due to the relatively small moisture jump.

Analogous to Chapter 3, I simulate three cases that differ in horizontal resolution to investigate the benchmark case. Also, here, the time steps—fixed in each simulation—are changed according to satisfy the CFL condition, and the number of grid points is adapted such that the domain size remains constant (Tab. 7). All three cases apply doubly-periodic lateral boundary conditions and have an identical vertical resolution of $\Delta_z < 3\,\mathrm{m}$ in and right above the ABL. In the non-turbulent region above the ABL, I gradually increase the vertical resolution to about $\Delta_z \approx 20\,\mathrm{m}$ at the domain top at about $z_{\mathrm{top}} \approx 850\,\mathrm{m}$.

Table 7: Simulation settings and cloud and turbulence properties averaged over the last hour of each simulation for the ACRF13 case. For the simulation settings $\Delta_{x,y}$ is the horizontal resolution, $N_{x,y} \times N_z$ are the number of grid points and Δt_{ACC}, Δt_{MP}, and Δt_{R} are the time steps for the acoustic mode, fast physics, microphysics, and radiation. For the horizontally averaged properties, $\max\left(\overline{TKE}_{\mathrm{s}}/\overline{TKE}_{\mathrm{t}}\right)$ is the maximum share of subgrid-scale turbulent kinetic energy, LWP and IWP denote the liquid and ice water paths, $\overline{d_{\mathrm{v}}/d_z}$ is the cloud void fraction, and d_z denotes the cloud depth.

id	$\Delta_{x,y}$	$N_{x,y} \times N_z$	Δt_{ACC}	Δt	Δt_{MP}	Δt_{R}
#35.0m	35 m	$128^2 \times 207$	1/16 s	3/4 s	1.5 s	5.0 s
#10.0m	10 m	$448^2 \times 207$	1/56 s	1/4 s	1.0 s	3.0 s
#03.5m	3.5 m	$1280^2 \times 207$	1/168 s	1/12 s	0.5 s	2.0 s

id	LWP	IWP	$\overline{d_{\mathrm{v}}/d_z}$	d_z	$\max\left(\overline{TKE}_{\mathrm{s}}/\overline{TKE}_{\mathrm{t}}\right)$
#35.0m	$20\,\mathrm{g\,m^{-2}}$	$0.90\,\mathrm{g\,m^{-2}}$	0.16 %	171 m	85 %
#10.0m	$18\,\mathrm{g\,m^{-2}}$	$0.80\,\mathrm{g\,m^{-2}}$	0.53 %	160 m	48 %
#03.5m	$18\,\mathrm{g\,m^{-2}}$	$0.81\,\mathrm{g\,m^{-2}}$	0.65 %	161 m	19 %

4.2 Model Adjustments

A detailed analysis of CTE benefits from additional output variables that give information on the temperature tendencies arising from the individual processes. These temperature tendencies may induce changes in the atmospheric stability, for instance, they might produce or hinder buoyant turbulent motions at the cloud top. I explain in this section the inclusion of temperature tendency outputs arising from six processes: radiation, microphysics, advection, large-scale subsidence, SGS, and numerics such as metric and acoustic terms. The complexity of this inclusion varies from being rather simple and straightforward changes within the *registry (Registry.EM_COMMON)* to fundamental source code analysis and variable tracking.

Registry Modifications Output for the tendencies arising from radiation, microphysics, and large-scale subsidence requires the *registry* to be modified. Thus, the corresponding variables *RTHRATEN*, *H_DIABATIC*, and *RORA_TH* need to be added to the history stream. I also add new variables to the corresponding file because no related variables exist for the other tendency components:

```
state real rora_dif_th ikj misc 1 - h "TH_DIF" "th tendency (dif)" "K s-1"
state real rora_adv_th ikj misc 1 - h "TH_ADV" "th tendency (adv)" "K s-1"
state real rora_tot_th ikj misc 1 - h "TH_TOT" "th tendency (non-split)" "K s-1"
```

These variables are not used in any calculation of WRF-LES and hence do not require initialization.

Advection Tendency The advection tendency can be directly accessed in the routine *rk_tendency (module_em.F)*. This is possible because the corresponding variable *t_tend* gets initialized during its calculation. The modifications of the routine *rk_tendency* read:

```
| | call to advection routines | |
rora_adv_th = t_tend / (c1h*mut+c2h) * msfty
```

The last line is required because the variable *t_tend* is at this stage of the model already coupled to the air mass and map factor. As the final step, the variable *rora_adv_th* needs to be passed to the top-level routine *solve_em (solve_em.F)*. Here, it can be finally stored on the *grid*, which is the output variable.

Sub-Grid Scale Tendency The SGS tendency is added to the variable *t_tendf* in the top-level routine *first_rk_step_part2(first_rk_step_part2.F)*, and it is accessed and stored from there. A temporary dummy initialization is required because the effects of the SGS parameterization are added directly to the already existing variable *t_tendf*:

```
grid%rora_dif_th = t_tendf
|| call vertical_diffusion_2 ||
|| call horizontal_diffusion_2 ||
grid%rora_dif_th = t_tendf - grid%rora_dif_th
grid%rora_dif_th = grid%rora_dif_th / (c1h*mut+c2h)
```

In analogy to the advection tendency, the last line is included to uncouple the variable *t_tendf* from air mass and map factor.

Numeric Tendency The numeric tendency arises from multiple processes which are added in various sections of the source code. Since all physical tendencies are stored explicitly, I decided not to search for all occurrences of tendencies arising from numerics and thereby risk missing one of them. Instead, I store the total tendency after the Runge–Kutta integration is finished—the sum of all individual tendencies. Therefore, again the variable *t_tend* is accessed in the routine top-level routine *solve_em (solve_em.F)*:

```
|| integration routines accessing t_tend ||
...
grid%rora_tot_th = t_tend / (c1h*mut+c2h) * msfty
```

Once more, the last line is included to uncouple the variable *t_tend* from air mass and map factor. With all the variables stored, it is possible to determine the residual tendency arising from numerics by subtracting all other tendency components from the total tendency.[22]

4.3 Results

I cover with the three cases one order of magnitude in horizontal resolution and simulate for the first time an Arctic Sc using an isotropic grid at the meter-scale. Therefore, I focus on aspects that benefit from such high resolution (Section 1.2): representation of turbulence (Section 4.3.2), representation of observed cloud and atmospheric state properties (Section 4.3.3), and scale-dependence of individual processes of CTE (Section 4.3.4). Before I commence with the process-level analysis based on this high-resolution dataset, I assess the data from the perspective of representativity in the context of observations that were used to define the setup (Section 4.3.1). The simulation data consists of instantaneous three-dimensional snapshots every five minutes. Time series of the corresponding slab-averaged first three statistic moments

[22] Although, one has to keep in mind that the total tendency considers the microphysical tendency from the preceding time step earlier due to the utilized time-split integration scheme.

and full three-dimensional snapshots at the initialization and end are made accessible by Rauterkus and Ansorge (2019).

4.3.1 Representativity of the Results

I use here time-slab averaged profiles of the simulation data like for the DYRF01 case described and analyzed in Chapter 3. Contrary to the simulation data, the observations considered are point measurements representing a limited period and a finite volume. Furthermore, this benchmark case is idealized (Section 4.1). In particular, wind profiles are constant with altitude, the large-scale divergence is constant in time, initialization profiles are smooth, and double periodic lateral boundary conditions prevent external lateral forcing of the ABL. All these aspects require careful analysis and explanation of how the simulation results are related to the utilized observations from (1) radiosoundings and (2) *Cloudnet* data.

(1) Two radiosoundings (11 UTC and 17 UTC) are used to initialize the simulation (Section 4.1) and compare the evolution of humidity, temperature, and wind between observation and simulation. They provide temporally and locally highly resolved data. However, they are instantaneous point measurements and are thus affected by turbulent motion and local conditions. Both are filtered out when using time-slab averages as commonly done in the analysis of LES data. For comparison between model and radiosounding, I average over the last hour of each case, which corresponds to the period from 16 UTC to 17 UTC. I do so because the model is forced by a large-scale divergence averaged over the whole simulation period. Therefore, I expect the ABL height and related properties to match the observations best at the end of the simulation.

(2) *Cloudnet* is an algorithm that provides various cloud properties based on observational data, such as data from Doppler cloud radar, microwave radiometer, and lidar (Illingworth et al., 2007). I use the derived liquid- and ice-water content, LWC and IWC. *Cloudnet* output consists of time series and is provided by the *Leibniz Institute for Tropospheric Research* for the PASCAL campaign. Provided are point measurements in time and space, averaged over 30 s. However, *Cloudnet* data still exhibit a large temporal variability (Fig. 21a), manifesting, for instance, in gaps between clouds (e. g. around 1330 UTC) and periods with lower liquid water path LWP (e. g. from 1630 UTC on). Time-slab averages from my LES do not capture this variability. While, for the large amount of data, I do not enable similar temporally resolved output for the LES, I

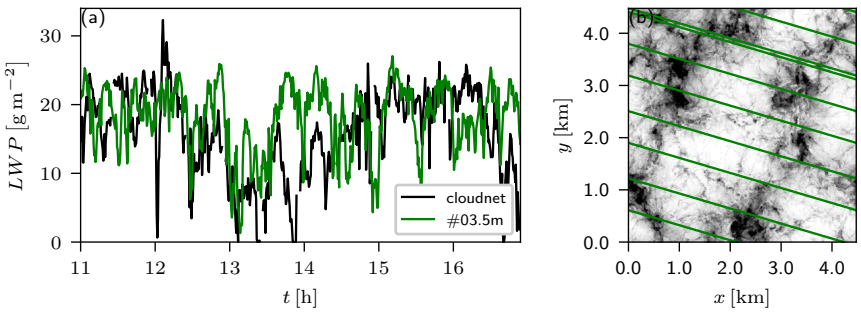

Figure 21: Panel (a) shows the observed liquid water path LWP compared to simulated LWP. For the simulated signal, I apply Taylor's frozen-turbulence hypothesis. Therefore, I create a hypothetical trajectory (green line) through the instantaneous snapshot of LWP at the end of case #03.5m (Panel (b)) by considering a domain-averaged convection velocity of $(u, v) = \left(1.54\,\mathrm{m\,s^{-1}}, -0.44\,\mathrm{m\,s^{-1}}\right)$ and double periodic boundary conditions. Along this trajectory, I print the LWP, averaged analogous to the observations over 30 s.

can use Taylor's frozen-turbulence hypothesis (Taylor, 1938; Moin, 2009) and convert a streamwise-sampled line from a horizontal slice to a time series using the height-local mean wind as advection velocity (Fig. 21b). I, thus, demonstrate that the simulation and the *Cloudnet* data share the same statistical behavior regarding their variability. Since simulation and *Cloudnet* data have comparable averaged LWP for the period from 1430 UTC to 1530 UTC, I perform my comparison between both data series for that period.

4.3.2 Representation of Turbulence

As discussed in Section 2.1, the general idea of LES is to resolve eddies up to the inertial subrange of turbulent motion where theories exist on how turbulence behaves and eventually dissipates. Thus, LES requires to explicitly resolve the eddies that carry most of the TKE. The smallest eddies are filtered by low-pass filtering the governing equations, which drastically reduces the computational costs. Thereby, TKE can be separated into a filtered or resolved part, TKE_r, and a non-resolved or SGS part, TKE_s. The larger the contribution of TKE_s is, the more important become the choices regarding the SGS model. The Smagorinsky model applied here simulates the SGS dissipation based on the stratification, resolved strain tensor, and equilibrium assumptions on the cascade of energy through the inertial subrange (Section 2.2.2). That is, it requires a finite scale range of the largest scales in the inertial subrange to be explicitly resolved throughout the simulated domain.

In most altitudes, TKE_r contributes to about 95 % of the total TKE, TKE_t (Fig. 22c). This does, however, not hold for the cloud-top region where the amount of TKE_r

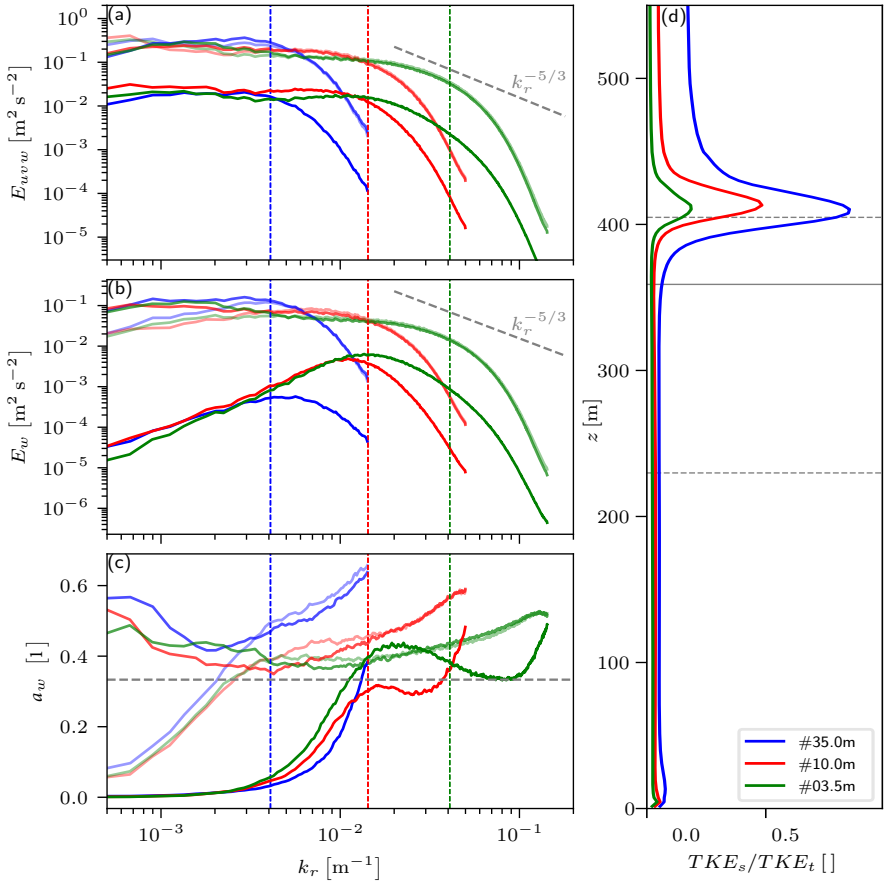

Figure 22: Energy spectrum of twice the resolved turbulent kinetic energy E_{uvw} (a), resolved turbulent vertical velocity (b) E_w and anisotropy of the vertical component $a_w = E_w/E_{uvw}$ (c). Different altitudes are marked by increasing transparency from top to bottom: 415 m (solid), 220 m (semi-transparent), and 60 m (transparent). Profiles of the contribution of sub-grid scale turbulent kinetic energy TKE_s to total turbulent kinetic energy TKE_t are shown in Fig. (d). The one-dimensional energy spectra are calculated by radial integration of the horizontal two-dimensional spectra of the perturbation velocities. The dashed gray line marks the Kolmogorov inertial power-law scaling, and the colored vertical lines mark the length scales of $7\Delta_{x,y}$ for each case. Dashed horizontal lines in (d) symbolize cloud bottom, and the solid horizontal line is the cloud maximum for case #03.5m, according to their definitions in Eq. 66.

accounts for only about 19 % of the total TKE in case #35.0m and reaches a maximum of about 85 % in case #03.5m (Tab. 7). These values illustrate the substantial contribution of the SGS model to the simulated atmospheric state. Therefore, I assess whether or not the assumption of a resolved part of the inertial subrange is met for the three cases by analyzing their spectra of kinetic energy, given in Fig. 22a and Fig. 22b.

The wavelength beyond which numerical dissipation notably affects turbulent motion is—in accordance with Skamarock (2004)—about seven times the grid resolution for both the total and the vertical energy spectrum (dashed lines in Fig. 22a,b). Both energy spectra indicate that case #35.0m does not resolve the inertial subrange while

case #03.5m resolves parts of it at wavenumbers $k \approx 0.03\,\mathrm{m}^{-1}$, close before numerical dissipation gets notable. Case #10.0m resolves the inertial subrange, if at all, only barely with the inertial −5/3 power-law scaling being a tangent at wavenumbers around $k \approx 0.02\,\mathrm{m}^{-1}$. In this range of wavenumbers, numerical dissipation starts to act, and thus, I cannot finally decide whether the beginning of the inertial subrange arises for physical or numerical reasons.

Fig. 22a and Fig. 22b inidcate that the share of the vertical motion within the boundary layer varies about 40.0% (37.8%–47.5%) for the three cases and two heights (60 m and 220 m above ground) investigated. This large share—if compared to isotropic motion—illustrates the convective nature of the benchmark case, despite the relatively weak surface forcing. Near the cloud top, this fraction exhibits a distinct minimum that differs among the three cases: for case #35.0m, vertical motions contribute only about 3.6 % to TKE_r, increasing to about 16.3 % for case #10.0m, and up to 29.6 % for case #03.5m. Although the suppression of turbulent motion is larger at small wavenumbers (large eddies) when compared to horizontal motion, it affects the whole spectrum. It is caused by the strong stratification at the cloud top, which suppresses turbulence, especially in the vertical and for large scales.

The surpression intensity of vertical motions is nicely illustrated by the wavenumber dependence of anisotropy a_w of TKE (Fig. 22c). I find a peak in the relative role of vertical motion in the spectrum around $k \approx 0.02\,\mathrm{m}^{-1}$ to $k \approx 0.05\,\mathrm{m}^{-1}$, thus, for scales on the order of 20–50 m. This range of scales can only be simulated explicitly for the cases #10.0m and #03.5m. The presence of vertical mixing is crucial for turbulence at the cloud-top. The maximum in this range of scales underlines the role of small-scale turbulence in supporting vertical penetration through the strongly stratified cloud-top interface. It shows that the resolved scales seem to properly feature the physical behavior only for case #03.5m. However, note that this seemingly crucial scale range is explicitly resolved for case #10.0m, too, which may already help because it suppresses inappropriate, for instance, diffusive effects of the SGS parameterization at this scale.

4.3.3 Bulk Evolution of the Simulations

Despite the indications that the SGS model cannot be fully trusted for the two lower-resolved cases, their profiles of atmospheric state variables evolve alike the ones of case #03.5m. Especially the profiles of potential temperature θ and water vapor mixing ratio r_v show no notable spread amongst each other (Fig. 23). Over time, the ABL moistens slightly and shrinks in height, as it is also indicated by the observational trend. The cloud layer remains coupled to the underneath ice, and a moisture inversion

does not form over the simulation period. Thus, my choice to not specify a moisture inversion is consistent with the relations used for initialization (Eq. 65a and Eq. 65b) and the evolution of profiles over the course of the simulation.

While θ and r_v agree well with the observations, there is a discrepancy between simulated and observed wind. For instance, its simulated strength is about 50 % smaller than the strength measured by the radiosonde, which is about 3 m s^{-1}. Furthermore, the observed wind is mainly westerly while the simulated wind is north-westerly. These discrepancies arise for two reasons. First, I compare instantaneous and local observations with time-slab averaged profiles from LES. Second, my simulation is idealized and at the beginning of a warm-air advection period. This large-scale phenomenon is not represented in my set-up and is the main reason for the different wind patterns between simulation and observations. During the simulation period, the warm-air advection sets in, and the mean wind turns from north-westerly to southerly, and increases from around 2 m s^{-1} to around 3 m s^{-1} within the ABL. Since the effect of warm-air advection is cumulative and merely sets in, the differences in thermodynamic variables between observation and simulation remain small (Knudsen et al., 2018, their Fig. 4).

The primary ice particle formation takes place within the first hour and consumes

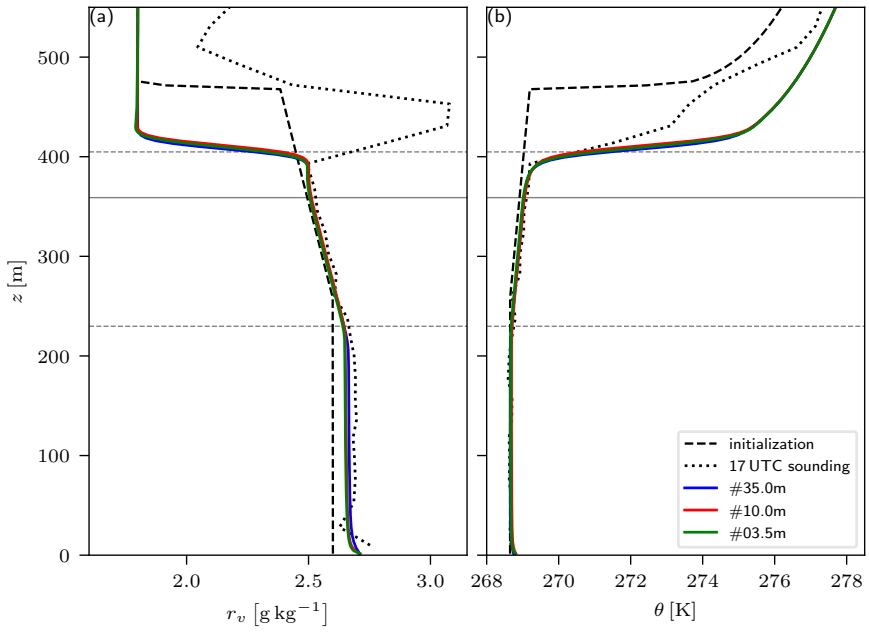

Figure 23: Radiosounding of water vapor mixing ratio r_v and potential temperature θ compared to profiles of the three simulations #35.0m, #10.0m, and #3.5m. Dashed horizontal lines symbolize cloud boundaries, and the solid line is the cloud maximum for case #03.5m, according to their definitions in Eq. 66.

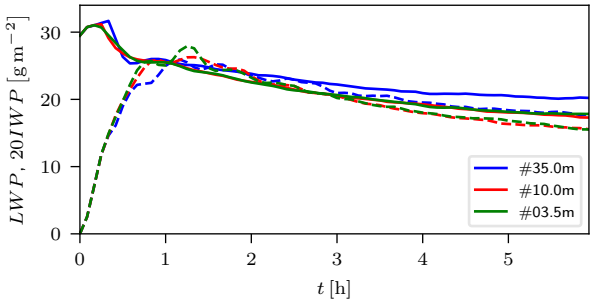

Figure 24: Temporal evolution of horizontally averaged simulated liquid and ice water path, LWP (solid) and IWP (dashed) for the three simulated cases #35.0m, #10.0m and #03.5m.

water from the initialized liquid Sc (Fig. 24). This process is a consequence of my initial condition that does only specify the total water mixing ratio in the form of liquid water instead of partitioning water to individual hydrometeor classes. It results in a simulated mixed-phase Sc that has a liquid mass fraction of about 95 %. This fraction is a consequence of constraints from the atmospheric state and is also indicated by *Cloudnet* data. Over the course of the simulation, LWP and the ice water path IWP decrease slowly in all three cases. This decrease is, however, not a sign of dissolving cloud here but results from decreasing ABL and cloud height as a consequence of the large-scale subsidence. The strength of the decrease directly results from my choice for intense large-scale subsidence and is in accordance with the 17 UTC radiosounding. All three cases show the same general evolution of the cloud quantities with advancing simulation: the cloud thickness decreases, the cloud subsides, and a nearly identical share and distribution between liquid and solid cloud particles arises—with the exception between case #35.0m and the higher resolved cases which is discussed below. Furthermore, all simulated amplitudes of LWC and IWC match *Cloudnet* data in general (Fig. 25). They, however, differ substantially below 150 m, where *Cloudnet* data indicates near-zero IWC while all three cases predict ice particles reaching the surface. Reasons for this discrepancy can evolve from the idealized set-up or the microphysical parameterization, such as a too high fall speed or a too slow melt process of ice particles. Although, the simulated precipitation rate (liquid and solid) is less than 0.003 mm h^{-1} and thus very likely too low for detection by the *Cloudnet* procedures. Therefore, I conclude the low IWC to be an in-principle correct process of slow ice-particle sedimentation since it is a common feature of Arctic Sc.

The vertical positioning of the Sc shows a small vertical offset between the simulated LWC and IWC profiles and the corresponding *Cloudnet* data. The offset manifests in an about 20 to 30 m downward shifted simulated cloud compared to the observational *Cloudnet* data. However, it seizes only one to two grid points given the vertical resolution of *Cloudnet* and thus likely results from grid-resolution uncertainties. It is also an averaging artifact because the cloud-top parameter derived from *Cloudnet* is

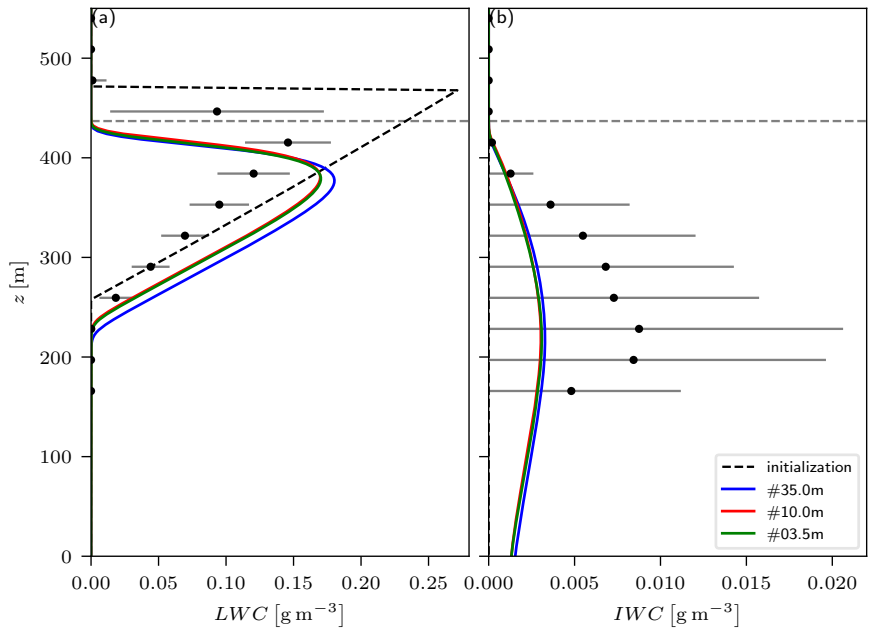

Figure 25: Liquid and ice water content, LWC and IWC, derived from *Cloudnet* data and simulation results. The dashed horizontal line marks *Cloudnet* cloud-top height, gray solid horizontal lines mark the standard deviation, and black dots mark the average of the *Cloudnet* data from 1430 UTC to 1530 UTC.

much closer to the simulated cloud top (dashed horizontal lines in Fig. 25). Another potential cause for this offset is the idealized set-up, especially considering large-scale subsidence to be constant with time.[23]

Comparing the different cases among each other, the evolution of the cloud quantities diverges between case #35.0m and the higher resolved cases #10.0m and #03.5m. This difference increases more the longer the simulation takes (Fig. 24). It illustrates the delicacy of process-level representation in CTE: while the profiles temperature and humidity are to zero-order and first-order constrained by the ABL energetics, an accurate cloud representation requires a realistic coverage of the scales where the CTE occurs. This delicacy is an inherent problem when looking at ABL clouds as they only exist in the extreme range of saturation from an averaged ABL perspective. After six hours of the simulation, the difference results in a decrease of about 10–15 % in LWP and IWP. This decrease in the cloud water and ice is caused by a slightly drier and warmer ABL in the higher resolved cases. While differences in the profiles of temperature and humidity are minimal and barely visible in Fig. 23, the non-linear relation to cloud quantities enhances them in the profiles of LWC and IWC in Fig. 25.[24]

[23] In the observations, large-scale subsidence is strong at the beginning and gets weaker towards the end of the simulation.

[24] One of the most-known relations is the Clausius–Clapeyron approximation used to calculate the saturation vapor pressure.

Below a horizontal resolution of $\Delta_{x,y} = 10\,\mathrm{m}$, I find that the cloud profiles stay nearly constant, which indicates convergence in zero- and first-order statistics. Other profiles, such as temperature and humidity, already converge at an even lower resolution.

4.3.4 Cloud-Top Entrainment

While tiny given the precision of even the most recent observational tools, the reduction in cloud thickness (about 10–15 % in LWP and IWP, and 4–6 % in LWC and IWC) from case #35.0m to the higher resolved ones constitutes a substantial difference in cloud dynamics. This difference may cause dissipation of the cloud or formation of drizzle where this should not happen. Such misrepresentation would have an enormous impact on ABL dynamics in a prognostic setting which warrants further investigation. As stated in Section 4.3.3, the reduction in condensed water is related to a slightly warmer and drier ABL. I show in this section that this warming and drying of the ABL is due to enhanced CTE of air from above the ABL. This results in a slightly higher ABL, notable in all variables.

The main processes contributing to CTE are wind shear, radiative, and microphysical cooling (Mellado, 2017). In this section, I analyze which of them causes the difference in CTE due to resolution and why this is so. Schulz and Mellado (2018) analyze in which situations wind shear is a driver of CTE. Since my benchmark case is convectively driven and has only a weak jump in wind velocity of about $0.2\,\mathrm{m\,s^{-1}}$ at the ABL top, I focus here on the radiative and microphysical cooling component of CTE, in the form of their corresponding cooling rates R and E. I also follow Matheou (2018) to analyze the cloud structure and define cloud depth d_z and void depth d_v within a cloud:

$$d_\mathrm{z} = z_\mathrm{t} - z_\mathrm{b} \tag{66a}$$

$$d_\mathrm{v} = \sum_{k}^{z_\mathrm{b} \le z(k) \le z_\mathrm{t}} a\,(k)\,\Delta z\,(k) \quad \text{with } a\,(k) = \begin{cases} 0 & r_\mathrm{l} + r_\mathrm{s} \ge 0.01\,\mathrm{g\,kg^{-1}} \\ 1 & \text{else} \end{cases}. \tag{66b}$$

Here, Δz is the considered vertical grid spacing, and z_t and z_b are the column cloud-top and cloud-bottom altitude, where I use the condition $r_\mathrm{l} + r_\mathrm{s} \ge 0.01\,\mathrm{g\,kg^{-1}}$ for the existence of a cloud with r_l and r_s the liquid and solid water mixing ratios respectively. Cloud depth is zero in the absence of a cloud, and void depth is one. Their ratio $d_\mathrm{v}/d_\mathrm{z}$ is a measure of how much dry air is engulfed within the cloud as a consequence of CTE.

Profiles of R and E show that microphysical cooling occurs immediately at the cloud

top while radiative cooling and microphysical heating occur below, namely within the uppermost cloud region (Fig. 26a). Besides the microphysical heating, this is in excellent agreement with theoretical considerations by Mellado (2017) and even more pronounced when considering the vertical coordinate $z - z_{\varepsilon,\mathrm{t}}$, for instance, when using height relative to the cloud top as vertical coordinate (Fig. 26c):

$$z_{\varepsilon,\mathrm{t}} = \max(0\,\mathrm{m}, z) \quad \text{where } r_\mathrm{l} + r_\mathrm{s} \geq \mathrm{EPS}(1.0)\ \mathrm{g\,kg^{-1}} \approx 10^{-7}\,\mathrm{g\,kg^{-1}}, \tag{67}$$

with EPS (1.0) the machine epsilon for a single-precision floating-point number. Columns with $z_{\varepsilon,\mathrm{t}} = 0\,\mathrm{m}$ are not considered in the statistic moments and account for far less than one percent across all three cases.

Using the relative coordinate $z - z_{\varepsilon,\mathrm{t}}$, I avoid averaging values at the cloud top with values from the middle of or outside the cloud. In consequence, the profiles averaged this way better reflect the local processes and peak more intensely. Notably, the profile of the microphysical cooling increases by a factor of about eight and sharpens, while the radiative cooling profile increases only by about 25 % and keeps its shape (Fig. 26a and Fig. 26c). This different behavior among both processes results from their differing physical mechanisms. Microphysical cooling and heating occur where hydrometeor phase changes take place: condensation and evaporation are locally often biased at the cloud boundaries due to up-, and downdrafts. For example, in updrafts condensation dominates the lower cloud boundary and evaporation the upper one. Contrary, effects due to hydrometeor phase changes tend to balance within the cloud (Fig. 27). Therefore, averaging values from different positions relative to the cloud top drastically weakens the resulting microphysical cooling at the cloud interface. Radiative cooling, on the contrary, is linked to the optical thickness of the cloud and thus not an interfacial process. It starts to act at the cloud top interface but strengthens the first meters within the cloud to a maximum of $-2\,\mathrm{K\,h^{-1}}$ at $z - z_{\varepsilon,\mathrm{t}} = -12\,\mathrm{m}$, because the cloud optical thickness increases since each cloud layer transmits, reflects, and emits radiation. This leads to a much smoother local vertical profile of radiative cooling in comparison with that of microphysical cooling. Except for a local maximum of about $0.35\,\mathrm{K\,h^{-1}}$ directly above the Sc, related to mostly frozen cloud fractions above the main part of the cloud, my radiative cooling profile follows the well-known shape of this quantity (Stevens et al., 2005; Mellado, 2017). However, compared to lower-latitude Sc, its peak is less pronounced, and the radiative cooling occurs over a deeper layer of the Sc. I attribute both phenomena to the LWP, which is lower than for low-latitude Sc, where cloud-optical thickness is higher. This illustrates a particular peculiarity of Arctic

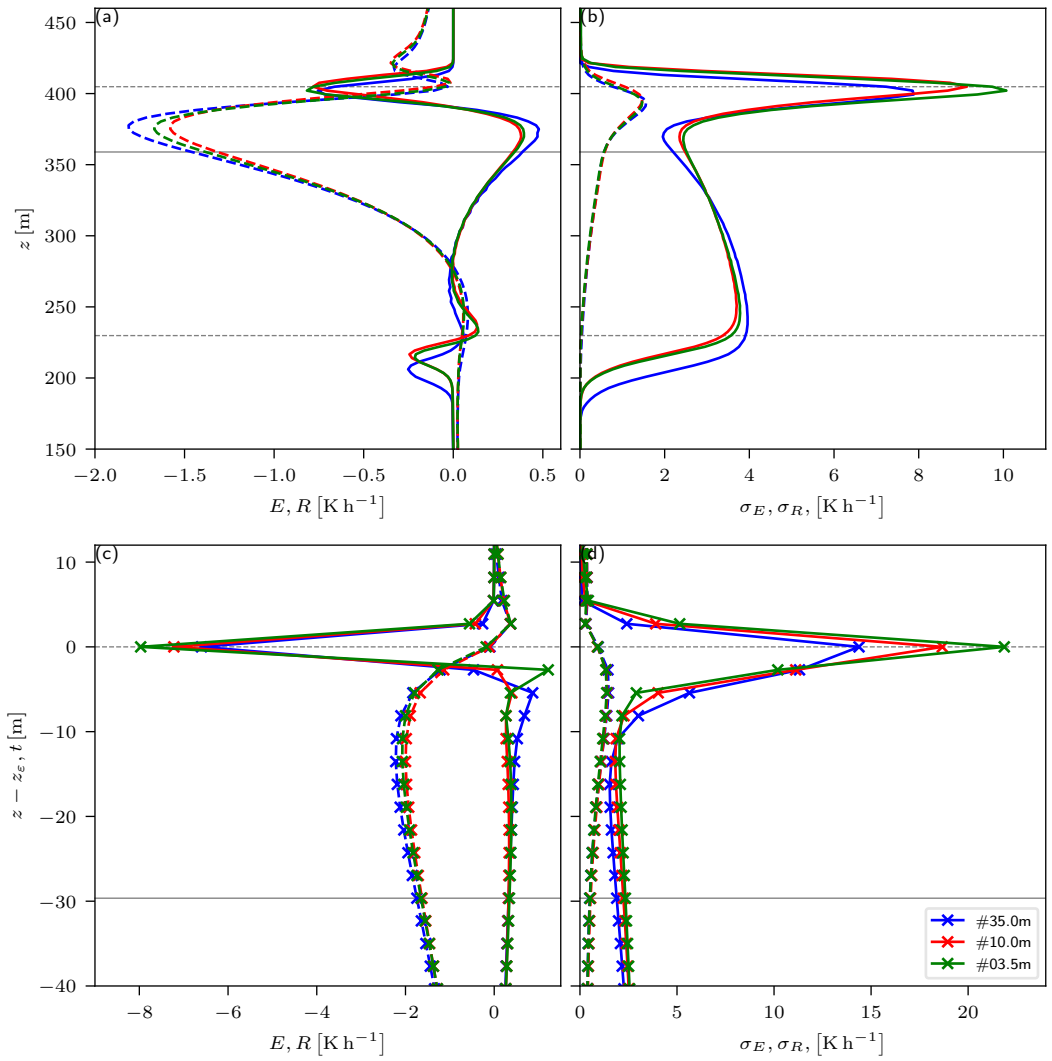

Figure 26: Horizontal mean and standard deviation of radiative (dashed) and microphysical (solid) cooling rates R and E. Regular height levels are used in (a) and (b), while (c) and (d) apply a coordinate relative to cloud-top height. The dashed horizontal lines mark cloud bottom and top and the solid one the cloud maximum for case #03.5m, according to their definitions in Eq. 66.

Sc, manifesting in strong dynamic differences when compared to low-latitude Sc. It highlights the importance of dedicated studies investigating the dynamics of these clouds.

Increasing horizontal resolution from case #35.0m to #10.0m results in intensified microphysical cooling (up to $-0.8\,\mathrm{K\,h^{-1}}$ due to higher resolved gradients) and weakened radiative cooling (up to $+0.2\,\mathrm{K\,h^{-1}}$ due to less cloud thickness). That means, higher resolution tends to intesify the cooling at the cloud top and, therefore, the resulting cloud-top instability from buoyancy reversal (Mellado et al., 2009). Thereby, the corresponding differences between the cases #10.0m and #03.5m are similar-sized to the ones between cases #35.0m and #10.0m and for radiation of opposite sign. I,

therefore, doubt that all processes are sufficiently resolved in case #10.0m, although its time-slab averaged zero- and first-order statistics do not differ from the ones of case #03.5m. A non-linear interaction between turbulence and microphysics on scales around $\Delta_{x,y} = 10\,\mathrm{m}$ that is not parameterized must cause the opposite sign in radiation and the ongoing increase in microphysical cooling at cloud top.

For further investigation of this feature, I turn to the investigation of spatial variability and microphysics. Instantaneous values of microphysical cooling at the cloud top locally reach values of up to $E \ll -100\,\mathrm{K\,h^{-1}}$ (Fig. 28a). These values are strongly variable in time and space and occur in all three cases. They result from different microphysical processes in up- and downdrafts, where vertical velocities reach values of about $\pm 1\,\mathrm{m\,s^{-1}}$, in combination with the time 'lag' of the microphysical parameterization. In updrafts, the lag intensifies the supersaturation of an air parcel being lifted until it enters the temperature inversion above the cloud (Fig. 27). Thus, in the uppermost cloud layer, supersaturation is largest and causes microphysical warming immediately below the cloud top. In the inversion, all condensed water evaporates and causes intense cooling. Air masses being engulfed from above into the cloud are warm and also enhance evaporation locally. Thus, they also contribute to the microphysical cooling maximum at the cloud top. At lower altitudes, the microphysical time-slab averaged tendencies are about one order of magnitude smaller, and the diabatic cooling in downdrafts tends to balance the diabatic heating in updrafts (Fig 27). The radiative cooling is almost constant within the middle and lower cloud layers and exhibits only small spatial variation compared to microphysical cooling within

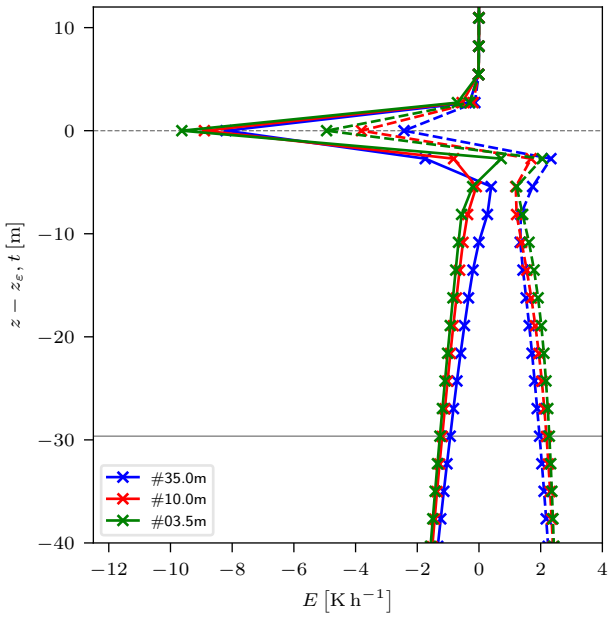

Figure 27: Microphysical cooling rate E conditioned to updrafts (positive vertical velocity, dashed) and downdrafts (negative vertical velocity, solid). The dashed horizontal line symbolizes cloud top, and the solid one is cloud maximum for case #03.5m, according to their definition in Eq. 66.

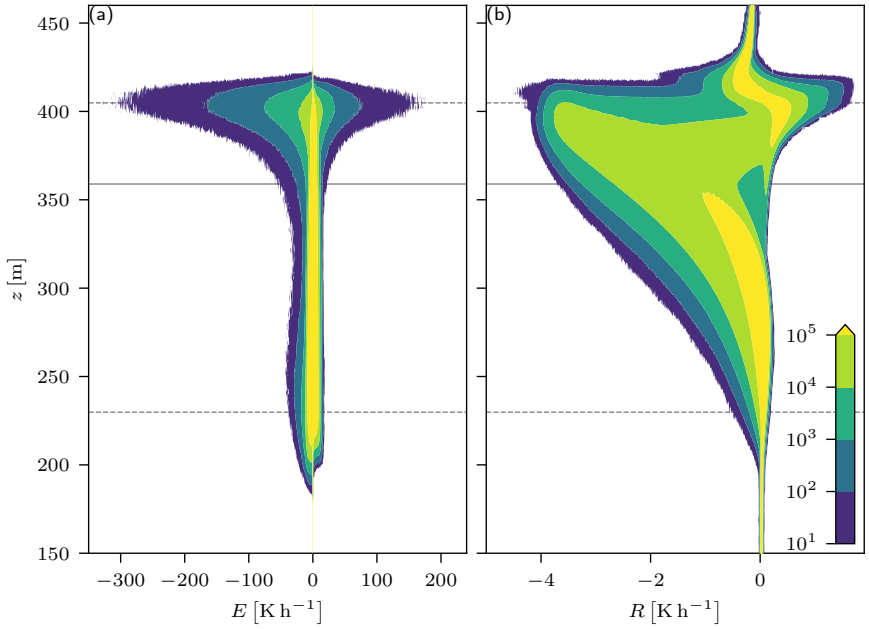

Figure 28: Probability distributions in absolute numbers of radiative and microphysical cooling rates R and E from case #03.5m, accumulated over the last hour of simulation. The bin sizes for R and E are 0.00625 $\left[\mathrm{K\,h^{-1}}\right]$ and 0.667 $\left[\mathrm{K\,h^{-1}}\right]$, respectively. The dashed horizontal lines symbolize cloud bottom and top, and the solid one is cloud maximum for case #03.5m, according to their definitions in Eq. 66.

the upper cloud layers (Fig. 28). In Section 4.3.2, I discuss the requirement of high resolution to resolve the energy spectrum sufficiently. The same holds for the spatial variability of cloud-top cooling (Fig. 26b, Fig. 26d, and Fig. 28), which in turn triggers turbulent motion. The higher the horizontal resolution is, the larger are horizontal gradients and in-plane variance. This effect is of particular importance at the cloud top, where a strong stratification suppresses turbulence and thus requires intense eddies to break through it and induce CTE (Garcia and Mellado, 2014). The same process also takes place at lower heights. However, the ABL is neutrally stratified and well-mixed in these altitudes. Thus, higher variability in cooling may induce or enhance eddies but is of no benefit for the CTE since the turbulence in the well-mixed layer is of larger scale and already more intense.

Considering the energy spectra (Fig. 22) and void-depth ratio (Fig. 29b) altogether reveals another reason for increased CTE with higher resolution. Assuming an eddy to require about seven grid points (Section 4.3.2; Skamarock, 2004), case #35.0m can only resolve eddies that are larger than about 250 m while case #03.5m resolves eddies down to about 25 m. The encroachment[25] of air above the ABL into the Sc occurs to a

[25] Entrainment describes the exchange of air masses, for example, due to diffusion and turbulent mixing. Contrary, encroachment contributes to entrainment but describes the enclosure of a larger (free tropospheric) air parcel (within the cloud).

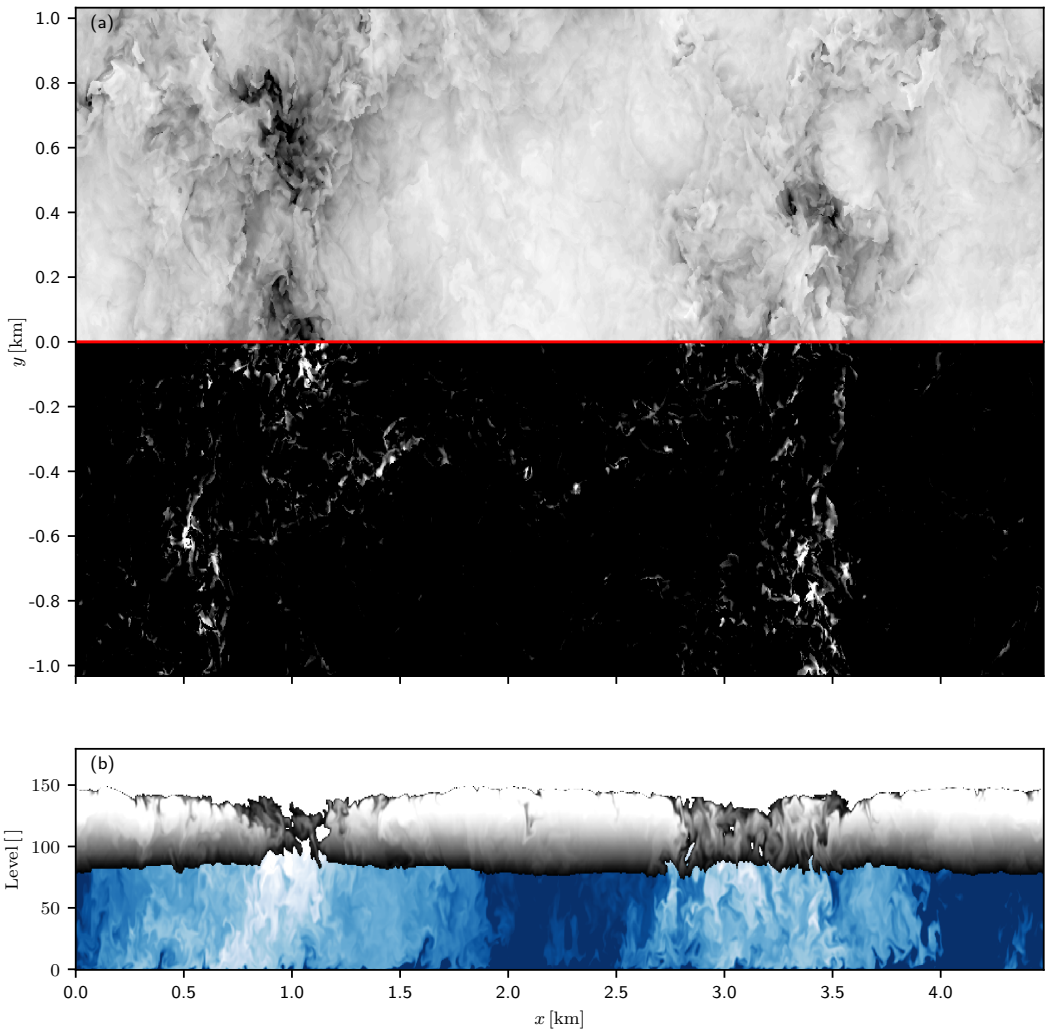

Figure 29: Instantaneous snapshots (a) of cloud thickness d_z above the red line (60 m (light) up to 200 m (dark)) and void fraction d_v/d_z below the red line (0 % (dark) up to 25 % (light)) at the end of case #03.5m. The red line marks the position of the slide shown in (b). There, I show an instantaneous snapshot at the same time of total water mixing ratio r_t [2.6 g kg^{-1} (white) up to 2.68 g kg^{-1} (blue)] and condensed water mixing ratio $r_s + r_l$ [0.01 g kg^{-1} (gray) up to 0.15 g kg^{-1} (white)].

large part in very localized and small regions at the cloud edges, which often span only a few tens of meters (Fig. 29). Since CTE is the only process that can trigger this encroachment, I suggest that resolving these regions is of particular importance to resolve CTE.

To analyze if and how strong encroachment depends on the horizontal resolution, I consider the production terms of θ'^2, which is the production of temperature variance:

$$\partial_t \theta' = R' + E' + A' + D' + S' + N' \tag{68}$$

$$\Leftrightarrow \quad \frac{1}{2}\partial_t \theta'^2 = \frac{1}{2}\partial_t \sigma_\theta^2 = \theta' R' + \theta' E' + \theta' A' + \theta' D' + \theta' S' + \theta' N'. \tag{69}$$

Henceforth, ψ' denotes the horizontal deviation of the variable ψ from its slab mean, and R, E, A, D, S, and N refer to the cooling rates induced by radiation, microphysics, advection, large-scale subsidence, the SGS model, and numerics such as metric and acoustic terms respectively. I give the corresponding profiles in Fig. 30, not showing the profiles related to large-scale subsidence S and numerics N. Large-scale subsidence is the strongest contributor to $\partial_t \theta$ and also contributes notably to $\partial_t \theta'^2$. It is, however, externally prescribed and thus relatively insensitive to horizontal resolution when compared to the other terms. The term N is estimated as a residuum and also shows only a weak sensitivity towards horizontal resolution.

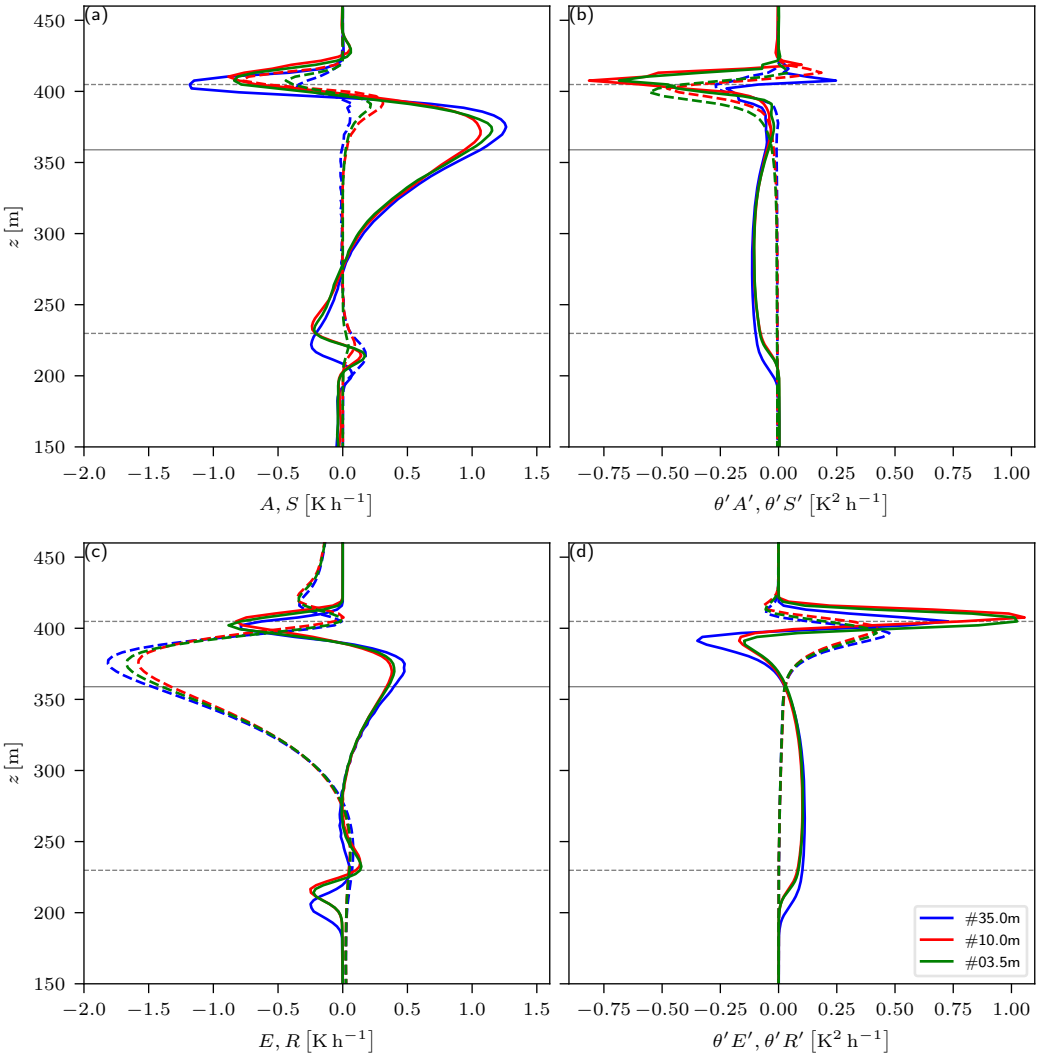

Figure 30: Cooling rates due to (a) Advection A (solid) and SGS S (dashed) as well as (c) Microphysics E (solid) and radiation R (dashed). Furthermore, Fig. (b) and (d) show the corresponding temperature variance production terms. The dashed (solid) horizontal lines symbolize cloud bottom and top (cloud maximum) for case #03.5m, according to their definitions in Eq. 66.

As discussed before, microphysical and radiative cooling produce temperature variance in heights around 400–420 m and 370–410 m, respectively. This production is for both processes close to cloud top, but it is only the microphysical process, which shows a strong sensitivity to horizontal resolution. Fig. 30 shows that both advection and the SGS consume temperature variance by mixing air masses, thus reducing vertical gradients at the cloud top. The mixing of air masses into the ABL is called encroachment and is dominated by vertical motion in my benchmark case. Further, advective and SGS elimination of temperature variance show high sensitivity towards horizontal resolution. Since the sensitivity is of opposite sign and comparable magnitude to the one of microphysical temperature variance production, I conclude that it is the microphysical cooling that causes enhanced entrainment by encroachment on both the resolved scales and the parameterized SGS. In a quantitative sense, I find an approximately three-fold increase of averaged void-depth ratio $\overline{d_v/d_z}$ from case #35.0m to case #10.0m and a further approximately 20 % increase from case #10.0m to case #03.5m (Tab. 7). Given the approximately constant geometric increase, I interpret the much smaller difference from #10.0m to #03.5m as an indication of convergence. All three cases show a cloud cover exceeding 99 %, and thus the increase in cloud-void ratio illustrates that the process is only marginally represented in the low-resolved case #35.0m. My results show that, although the time-slab averaged profiles of many atmospheric quantities converge for a horizontal resolution of $\Delta_{x,y} = 10$ m and below, the simulation does not converge in terms of process-representativity. Indeed, processes have to be taken into account at such high resolutions that are not resolved for lower resolutions. Thereby I observe a beginning process-level convergence around my finest resolved case #03.5m since the changes from case #35.0m to case #10.0m are much more intense than the ones from case #10.0m to case #03.5m.

Chapter 5

Surface Heterogeneity Effects on Stratocumulus

LES studies extensively investigate the effects of surface heterogeneities on the Arctic ABL (Weinbrecht and Raasch, 2001; Esau, 2007; Stoll and Porté-Agel, 2009; Wenta and Herman, 2019; Michaelis et al., 2020). Indeed, the Arctic offers suitable conditions for such studies: persistent ABLs that experience a less rapid diurnal cycle than those in lower latitudes and distinct differences in surface fluxes and albedo between ice sheets and oceanic water. The lack of complex local topography also suits (semi-)idealized LES. Many of these studies are limited to the investigation of Arctic leads[26] and their effects on the cloud-free ABL (Glendening and Burk, 1992; Glendening, 1994; Weinbrecht and Raasch, 2001; Esau, 2007; Lüpkes et al., 2008a; Michaelis et al., 2020). Studies of irregularly structured surface heterogeneity–still limited to cloud-free ABLs—are rare but indicate that restructuring surface types[27] may have large effects on turbulence evolution, surface fluxes, and circulation patterns due to the formation of secondary circulations. The knowledge gained from these studies is limited to specific cloud-free ABL cases and based on relatively coarse resolution (Wenta and Herman, 2018, 2019) or rather small domains with stable ABLs (Stoll and Porté-Agel, 2009; Mironov and Sullivan, 2015). Their results are supported by similar studies performed for convective ABLs in lower latitudes (Raasch and Harbusch, 2001; Prabha et al., 2007; Maronga and Raasch, 2013; Liu et al., 2017).

The ABL determines the cloud-driving quantities. Therefore, changes in its structure, quantities, or circulation are likely to cause changes in the simulated Sc. Nevertheless, to my knowledge, no LES studies exist which investigate such effects of surface heterogeneity on Arctic Sc which warrants further investigation. I extend the setup introduced in Chapter 4 to a highly-resolved Sc over a heterogeneous Arctic surface consisting of oceanic water and ice sheets. To this end, I modify the ACRF13 case to

[26] Leads are mostly linear open-water channels surrounded by ice with varying lengths and widths.

[27] Restructuring surface types affects not the bulk surface properties. Thus, studies considering the structure of surface types distinguish clearly from traditional Arctic lead studies, which investigate the effects of additional energy input by the Arctic lead.

enhance the differences between both surface types, such as their heat fluxes, and simplify the analysis (Section 5.1). For the latter reason, I also add the individual components of the water vapor tendency to the output of WRF-LES (Section 5.2). The test suite, which reduces the computational demand for this study and allows the creation, implementation, and investigation of varying reproducible surface patterns is presented in Section 5.3. In Section 5.4, the differences arising from the application of individual surface patterns are investigated in conjunction with constant bulk surface properties. The outlined methods are not limited to this case, especially the test suite and pattern creation algorithm. They are not limited to the Arctic but can be applied instead to other regions with different surface types.

5.1 Setup Description

The ACRF13 setup describes a good case for investigating mixed-phase Sc during Arctic spring (Chapter 4). However, I focus here on the investigation of the effects resulting from structuring heterogeneity in the surface pattern. Therefore, I modify the ACRF13 setup (Section 4.1) of case #03.5m—to simplify analysis and strengthen differences between the utilized surface types. These modifications are required because the signals investigated here are otherwise too weak, and the considered statistic measures are calculated over extensive periods, which causes uncertainties due to the strong large-scale subsidence. The modifications include rotation of the geostrophic forcing, reduction of the large-scale divergence, and reduction of the surface temperature. Furthermore, the surface is no longer a homogeneous ice surface but consists of a pattern from ice sheets and oceanic water (Section 5.3). All these modifications affect the results of the simulations compared to the original ACRF13 case. Additionally, I adjusted the horizontal resolution to $\Delta_{x,y} = 3\,\mathrm{m}$ and the domain size accordingly to $N_{x,y} \times N_z = 1530^2 \times 207$ grid points. The vertical resolution is approximately $\Delta_z = 3\,\mathrm{m}$ within and closely above the ABL and increases to about $\Delta_z = 16\,\mathrm{m}$ at the model top. The time steps remain the same as the ones for case #03.5m of the ACRF13 case. Thus, although the case here is based on the ACRF13 case, it is not quantitatively comparable.

Rotation of the Geostrophic Forcing The goal of rotating the geostrophic forcing is to provide an almost zonal horizontal motion close to the surface. The new geostrophic wind vector is $(u, v) = (1.6, -0.18)\ \mathrm{m\,s^{-1}}$. The rotation has no influence on the results compared to the original ACRF13 case because the simulations are idealized—especially the initial and boundary conditions are homogeneous and pe-

riodic for the whole domain. The same effect can be provided by rotating the grid after the simulation. The rotation simplifies analysis because it allows to directly calculate relevant measures parallel and perpendicular to the mean wind direction. This simplification is only valid close to the surface due to the rotation of the wind with height. Indeed, even at the surface, the motion is not purely, but merely closely, zonal.

Reduction of the Large-Scale Divergence The ACRF13 case is affected by intense large-scale subsidence, causing a reduction of the ABL height about multiple tens of meters throughout the simulation. The persistent shrinking of the ABL height complicates analysis because statistics calculated over one hour or even longer are affected by variations of the ABL height and cloud position. To attain an approximately steady ABL height, I reduce large-scale divergence D_{ls} to 5×10^{-6} s—a reduction to about half the original value. This modification causes differences in the results compared to the original ACRF13 case.

Reduction of Surface Temperature The reduction of the surface temperature is necessary to enhance signals arising from surface heterogeneity. If merely the surface type is changed from ice to water, an effect is if at all only barely visible and mainly a consequence of changes in albedo. Consequently, I cool the ice sheets down to 261.35 K, which is ten Kelvin cooler than the utilized oceanic water temperature of 271.35 K. The chosen difference of 10 K, thereby, lies well within the threshold of observed temperature differences (Lüpkes et al., 2008b). Further, I keep the air mass as warm as in the ACRF13 case. Thus, the chosen setup describes a synoptic case where a relatively warm maritime air mass overpasses Arctic ice sheets.

5.2 Model Adjustments

Section 4.2 describes how all potential temperature tendency components are added to the output of WRF-LES in order to achieve a better understanding of the processes leading to cloud-top entrainment. These variables are of great value for in-depth analysis of processes driving the Sc. For physical completeness, I add all tendency components of the water vapor mixing ratio to the output of WRF-LES. These tendency components can help to understand how water vapor propagates through the atmosphere. Together with the tendency components of potential temperature, such analysis offers quantitative insight into the physical causes of latent and sensible heat

fluxes. Modifications to the source code are similar to those described in Section 4.2 and briefly outlined in the paragraphs below.

Registry Modifications Output for the water vapor tendency components arising from microphysics and large-scale subsidence is achieved by registry modification. The corresponding variables *QV_DIABATIC* and *RORA_QV* need to be added to the history stream. I also add new variables to the registry because no corresponding variables exist for the other tendency components:

```
state real rora_dif_qv ikj misc 1 - h "QV_DIF" "qv tendency (dif)" "kg kg-1 s-1"
state real rora_adv_qv ikj misc 1 - h "QV_ADV" "qv tendency (adv)" "kg kg-1 s-1"
```

These variables are not used in any calculation of WRF-LES and hence do not require initialization. Contrary to its temperature-related counterpart, no total and residual tendency components are necessary because no other tendency components exist in WRF-LES. However, further physical tendency components should be added if additional parameterization schemes alter the respective tendencies, such as those for convection or the ABL.

Advection Tendency The advection tendency component is directly accessed and stored from the routine *solve_em (solve_em.F)*. This is possible because the corresponding variable *advect_tend* gets initialized during its calculation in the routine *rk_scalar_tend (module_em.F)*. The modifications of the routine *solve_em* read:

```
moist_variable_loop: DO im = param_first_scalar, num_3d_m
  ...
  CALL rk_scalar_tend(..., advect_tend, ...)
  IF (im == p_qv) THEN
    grid%rora_adv_qv = advect_tend / (c1h*mut+c2h) * msfty
  END IF
  ...
END DO moist_variable_loop
```

Like its temperature-related counterpart, the variable *advect_tend* is coupled to air mass and map factor and thus requires decoupling. The if-condition is necessary to ensure that only the water vapor mixing ratio is processed because the encompassing loop runs over all moisture variables.

Sub-Grid Scale Tendency The SGS tendency component is added to the variable *moist_tend* during the routine *first_rk_step_part2 (first_rk_step_part2.F)*, and it is accessed and stored from there. Analogous to its temperature-related counterpart, a dummy initialization is required because the SGS tendency component is added directly to the already existing tendency variable and not stored separately:

```
grid%rora_dif_qv = moist_tend
|| call vertical_diffusion_2 ||
|| call horizontal_diffusion_2 ||
grid%rora_dif_qv = moist_tend - grid%rora_dif_qv
grid%rora_dif_qv = grid%rora_dif_qv / (c1h*mut+c2h)
```

In analogy to the advection tendency, the value of *moist_tend* is decoupled from the air mass in the final line to attain the units required for quantitative comparison.

5.3 Test Suite

The test suite must provide definitions for reproducible surface patterns—providing the same bulk surface properties—that suit the idealized setup. Furthermore, also a procedure reducing computational demands is developed to avoid repetitive calculation of the spin-up period.

Pattern Creation All surface patterns share the same fraction of ice sheets (80 %) and oceanic water (20 %) to achieve the same bulk surface properties and thus to minimize the influence of a variation in the bulk boundary conditions on the simulation. The surface types have constant properties throughout all simulation periods. Most notably, their temperatures differ by about 10 K. Other surface parameters are given in Tab. 8. Thus, bulk surface properties are kept constant across the different cases while the arrangement or structure of ice sheets and oceanic water changes. The setup distinguishes substantial from the original ACRF13 case and demands a specific surface pattern to be defined as a reference. This reference pattern is called pattern #pat0, and its arrangement of ice sheets and oceanic water follows a pseudo-randomized structure (Fig. 31a). Thereby, each individual surface type patch encompasses at least a square of 9×9 grid points to ensure that the patches and their immediate interaction with the turbulent ABL are numerically resolved.

Table 8: Quantities of the utilized surface types. The roughness length over oceanic water varies depending on wind speed and stability and is given as an averaged value.

quantity	ice sheets	oceanic water
temperature	261.35 K	271.35 K
albedo	85 %	8 %
roughness length	10^{-3} m	3.3×10^{-5} m
moisture availability	95 %	100 %
emissivity	95 %	98 %

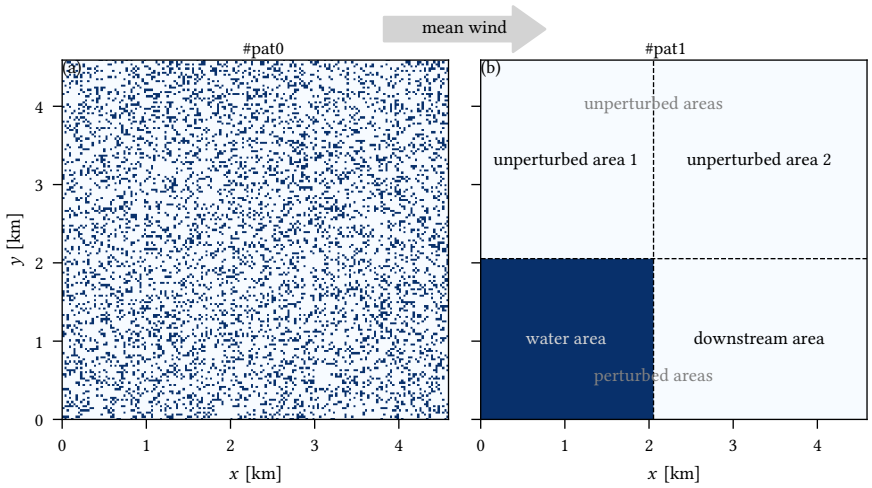

Figure 31: The utilized surface patterns consisting of two surface types: ice sheets (white) accounting for 80 % of the domain and oceanic water (blue) accounting for 20 % of the domain. The corresponding surface properties are given in Tab. 8. Pattern #pat0 visualizes a pseudo-randomized distribution of ice sheets and oceanic water where each surface type patch exceeds at least 9 × 9 grid points. Contrary, all of the oceanic water is accumulated at one quadratic area in pattern #pat1. The dashed lines in pattern #pat1 separate individual areas utilized for the discussion, and the gray arrow symbolizes near-surface wind direction.

The reference pattern #pat0 is as unstructured as possible. The second surface pattern, pattern #pat1, exhibits maximum structure by accumulating the oceanic water in one quadratic area (Fig. 31b). It is possible to define individual areas from pattern #pat1 based on their surface type and streamwise location. The *water area* encompasses the region where the oceanic water is accumulated, and the *downstream area* covers the region downstream. Locally, both areas can be considered to be directly perturbed by the oceanic water, which is why their sum is referred to as *perturbed areas*. Contrary, the *unperturbed area 1* and the *unperturbed area 2* are not perturbed directly by the oceanic water because they are located streamwise parallel to the *water area*. Hence, their sum is referred to as *unperturbed areas* (Fig. 31b).

The presented surface patterns #pat0 and #pat1 can be understood as limiting cases in terms of heterogeneity structure. A third limiting case would be a case similar to the frequently studied Arctic leads. The surface pattern of a traditional Arctic lead case (Glendening and Burk, 1992; Michaelis et al., 2020) is also structured as much as possible, but, compared to pattern #pat1, the accumulated water is structured more anisotropic. Due to the utilized periodic boundary condition, such a case is tough to investigate in the presented setup because the Arctic lead would periodically reappear. This is a consequence of the different approaches. Studies investigating Arctic leads usually investigate the effects additional energy, provided by the Arctic lead, has on the ABL. Contrary,the objective of my study is to investigate the effects of surface

heterogeneity structure where no additional energy shall be provided to the ABL among the individual surface patterns.

While the presented simulations are constrained to the limiting patterns #pat0 and #pat1, I develop and present in Appendix B an algorithm to create reproducible pseudo-randomized but still structured patterns. These patterns are especially useful for semi-idealized and idealized LES utilizing double-periodic boundary conditions and require only a dominating structure length scale as an input parameter. Therefore, the investigation of multiple surface patterns with varying dominating structure length scales might gain insight into which structure length propagates best through the atmosphere.

Simulation Procedure LES demands a decent simulation time before profound analysis can be performed. It is required to achieve a state of the simulation where the processes are in a physically reasonable state. This spin-up period is a consequence of an artificial initial condition, and it heavily depends on the domain size, stability of the atmosphere, and turbulence. For instance, a convective ABL reaches an appropriate state faster than a stable ABL due to more intense vertical propagation and vigorous initiation of turbulence.

A repetitive simulation of the spin-up period would waste a substantial amount of computational resources for periods where no analysis needs to be performed. For instance, suppose the spin-up period is expected to take about two hours, and analysis shall thus be performed only during the third hour. In that case, more than 65 % of the computational resources are utilized to reach an analyzable state of the simulation. Furthermore, suppose two surface patterns are simulated in such a simuation, and the first hour is simulated only once. In that case, only five instead of six hours are simulated—the more surface patterns are investigated, the larger the savings of computational resources. However, it should be noted that a restart of the simulation after the first hour is required because the surface patterns are changed. This change, indeed, demands another spin-up period, but this process is much faster than the former one as it is based on a realistic initial condition with respect to the turbulent state of the ABL.

In this study, the analysis is performed over the third and fourth hour of simulation period for each surface pattern. The first hour of the simulation period is performed only once on pattern #pat0, and after that hour, the individual patterns are implemented and simulated for three hours. The first hour after the restart is excluded from the analysis in order to build up the pattern-specific turbulence.

5.4 Results

I cover with the two presented surface patterns the limiting cases of heterogeneity structure. Hence, I expect the effects to be maximum compared to other surface heterogeneity structures with identical bulk surface properties. To access the corresponding heterogeneity-induced part ψ_{hi} of a quantity ψ, I define as in Maronga and Raasch (2013)

$$\psi_{\mathrm{hi}}(x, y, z, t) = \psi(x, y, z, t) - \psi_0(z, t), \tag{70}$$

where $\psi_0(z, t)$ denotes the corresponding slab average of the considered quantity for the reference pattern #pat0. Thus, ψ_{hi} allows dedicated analysis of changes arising due to variations in the surface patterns.

I analyze here the period between 13 UTC and 15 UTC, which are the third and fourth simulated hours. First, I describe the general atmospheric state which the modified case produces. Therefore, I limit the analysis to the bulk state, which pattern #pat0 produces (Section 5.4.1). Second, I analyze the effects of modifications to the surface heterogeneity structure on these bulk quantities (Section 5.4.2). Third, I examine how surface heterogeneity structure affects cloud-top entrainment and the organization of the Sc (Section 5.4.3). Fourth, I synthesize the results from the preceding sections and analyze in detail where the observed features originate from (Section 5.4.4). In Section 5.4.5, I outline which effects the surface experiences. If not stated differently, the analysis is performed on time-slab averaged quantities, calculated from full three-dimensional snapshots, which are stored every five minutes.[28]

5.4.1 Bulk Evolution of the Basic Pattern

The simulation utilizing the reference pattern #pat0 produces a well-mixed ABL in a neutral to a weakly stable state. With advancing simulation, the ABL cools and develops a temperature inversion above the surface (Fig. 32a) which is most intense in the early stages of the simulation (0.8 K over 20 m at 13 UTC) and gets weaker the longer the simulation takes (0.6 K over 20 m at 15 UTC). This weakening is a consequence of surface cooling and thus induced stability of the ABL. Hence, the ABL is less driven by the surface in comparison with the original ACRF13 case, which gives more importance to cloud-induced turbulence. The cooling of the ABL is roughly

[28] Time series of the corresponding slab-averaged first three statistic moments and full three-dimensional snapshots at the initialization and end are accessible by contacting r.rauterkus@posteo.net.

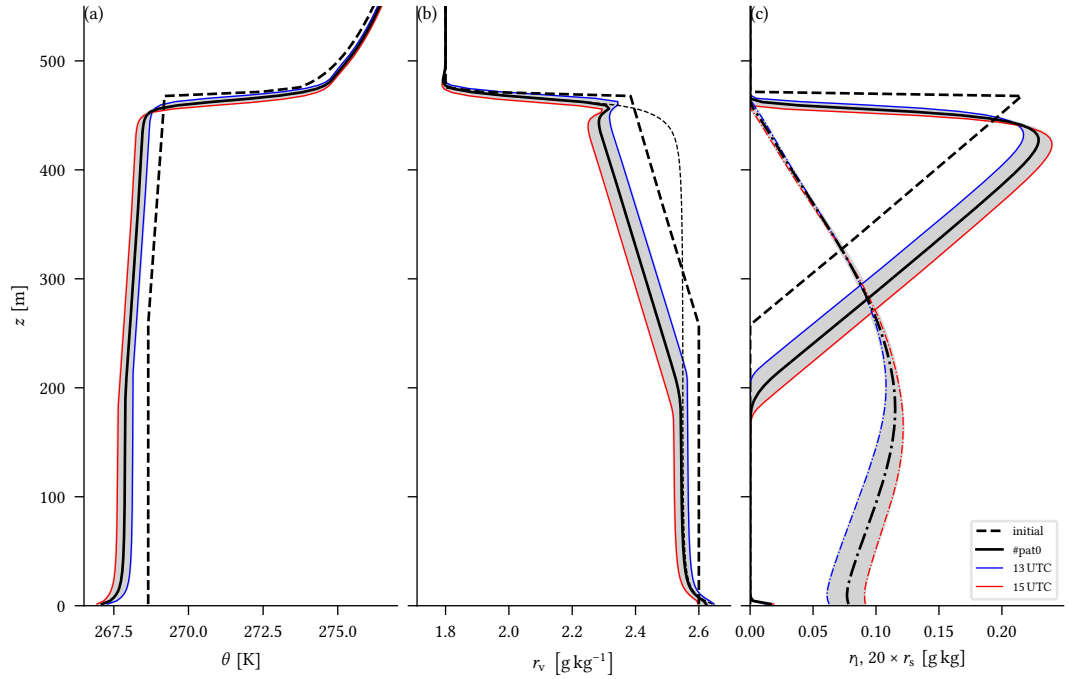

Figure 32: Time-slab averaged profiles of potential temperature θ, water vapor mixing ratio r_v, and liquid (solid) and solid (dash-dotted) water mixing ratios, η and r_s. The grey shading represents the corresponding instantaneous range of slab-averaged values occurring in the output files, which are stored every five minutes. The dashed line in panel (b) marks the time-slab average of the total water vapor mixing ratio.

monotonous throughout the simulation, as indiciated by the colored lines in Fig. 32a.

Similar to the potential temperature θ, also water vapor mixing ratio r_v decreases roughly monotonously with time (Fig. 32b), so does the total water mixing ratio r_t. Here, the surface is not the driver of the decrease. In fact, it counteracts the decrease by providing moisture to the ABL, which is indicated by increasing r_v near the surface resulting from its evaporation. Therefore, the decrease of moisture in the ABL is a consequence of precipitation and entrained dry air. While the bulk profile of θ follows a well-known shape which is, for example, roughly comparable to the ones presented in the DYRF01 and ACRF13 cases, the shape of the bulk profile of r_v deviates from the expected shape. At the interface between free atmosphere and ABL, two bulges are found. Within the free atmosphere, a small negative bulge forms with drier air mass. Contrary, at the top of the cloud, a large positive bulge forms with moister air mass. However, in the profile of r_t, only the dry bulge is observed. Thus, the lower wet bulge merely marks a different partition among the individual water species. At the top of the ABL, the temperature inversion drastically increases the saturation vapor pressure, and therefore the cloud evaporates, producing the observed bulge in r_v. The bulge within the free troposphere also appears in the profile of r_t and is caused by the

overall drying ABL due to water consumption of the Sc. Pressel et al. (2017) relate the appearance of a similar bulge to numerical phenomena, but this is not the case here because I utilize the same monotonic advection schemes as in the preceding studies that are stated to counteract these phenomena (Section 2.2; Pressel et al., 2017).

Both quantities indicate an approximately constant height of the ABL over the course the simulation as expected due to the reduced large-scale divergence. In terms of Sc development, the evolutions of θ and r_v counteract each other to a certain degree and result in a thickening of Sc in the solid and liquid phase, which also subsides slowly (Fig. 32c). The sedimentation is four to five times more intense than in the original ACRF13 case, depending on altitude, and more than 95 % solid phase. Although the precipitation is more intense and the share of simulated snow particles compared to simulated ice particles is larger than in the original ACRF13 case, the precipitation is still low ($0.01\,\mathrm{mm\,h^{-1}}$).

A dedicated peak is observable in the liquid water mixing ratio r_l within the lowest ten meters, which also contributes to the surface precipitation. This peak is not related to sedimentation of liquid or solid hydrometeors from higher altitudes but represents near-surface radiation fog. Sc and radiation fog are mostly of liquid phase with a share of about 95 %. This share slightly increases with time because liquid water path LWP increases more with advancing simulation than ice water path IWP (Fig. 33). Especially, the increase in IWP occurs not within the Sc but in sedimentation (Fig. 32c).

Contrary to the thermodynamic quantities, the dynamic quantities are stationary (Fig 34). The horizontal wind is in balance with the geostrophic forcing down to a height of approximately 50 m. Thus, wind shear at the interface of free troposphere and ABL is not considered further in this analysis. In the surface layer, below an altitude of 50 m, the wind rotates from 96° to 90° at the surface (Fig 34b) and its speed v_h approaches its surface boundary condition $v_h = 0\,\mathrm{m\,s^{-1}}$ where the value at the first grid point, 1.5 m above the surface, is $v_h = 1.2\,\mathrm{ms^{-1}}$ (Fig 34a).

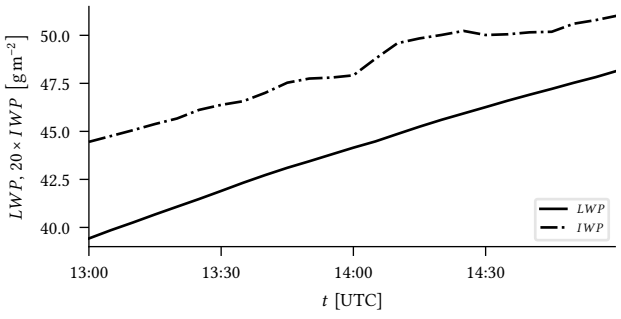

Figure 33: Temporal evolution of slab-averaged liquid and ice water path, LWP and IWP.

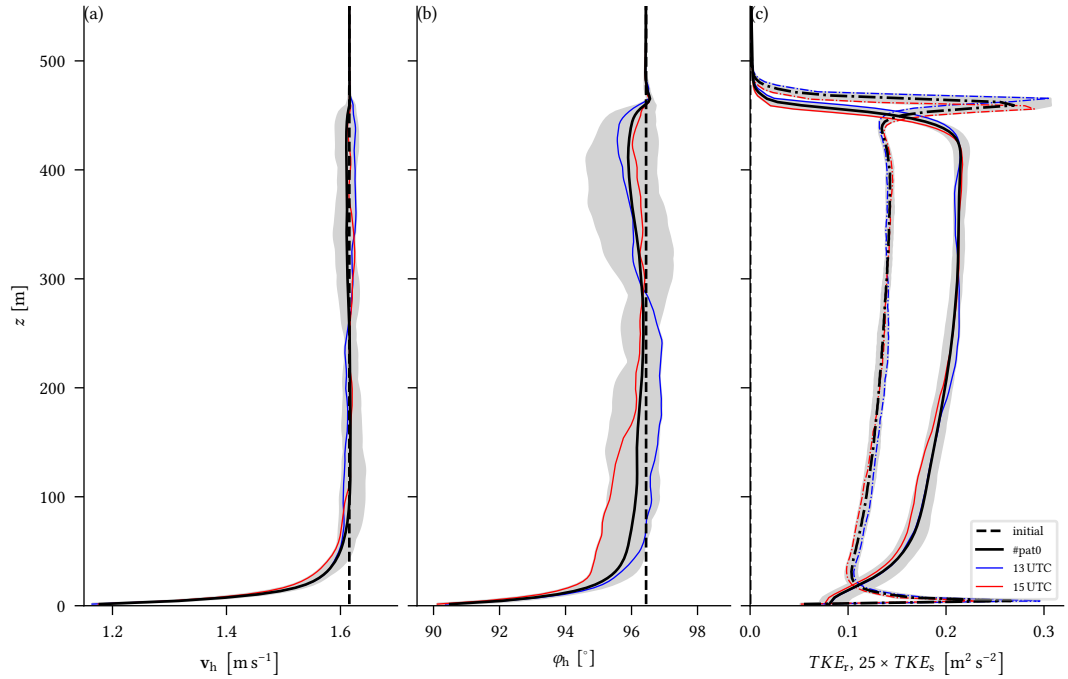

Figure 34: Time-slab averaged profiles of horizontal wind speed v_h, horizontal wind direction ϕ_h, and resolved (solid) and sub-grid scale (dash-dotted) turbulent kinetic energies, TKE_r and TKE_s. The grey shading represents the corresponding instantaneous range of slab-averaged values occurring in the output files, which are stored every five minutes.

As a consequence of the more stable layered atmosphere, turbulence is in the free ABL about 60 % weaker than in the ACRF13 case (Fig. 22a and 35a). The profiles of resolved and SGS TKE, TKE_r and TKE_s (Fig. 34c), and the corresponding energy spectrum

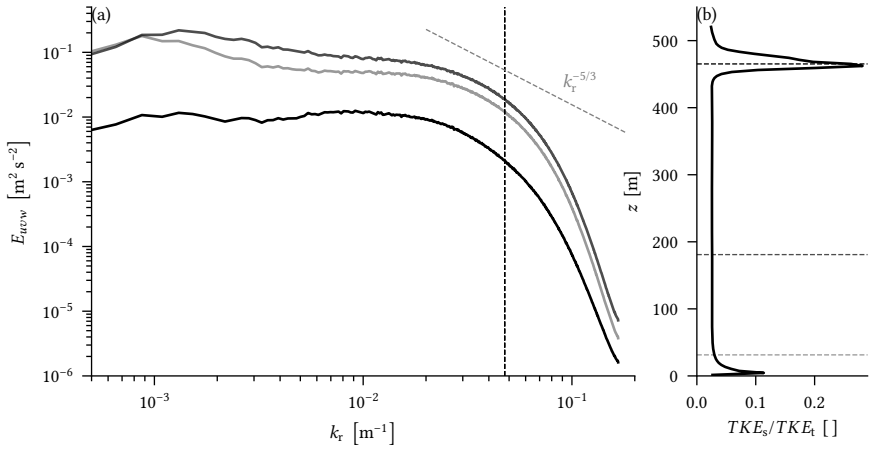

Figure 35: Time-slab averaged energy spectrum of twice the resolved turbulent kinetic energy E_{uvw} and the share of sub-grid scale turbulent kinetic energy to total turbulent kinetic energy, TKE_s/TKE_t. The one-dimensional energy spectra are calculated by radial integration of the horizontal two-dimensional spectra of the perturbation velocities. The shading in panel (a) represents three different heights, indicated by corresponding dashed lines in panel (b). The vertical dashed line in panel (a) marks the wave number of $7\Delta_{x,y}$.

(Fig. 35a) are nevertheless similar to the ones of the ACRF13 case (Section 4.3.2). Thereby, the share of TKE_s in the free ABL slightly increased from 0.25 % to 0.03 % compared to the ACRF13 case (Fig. 22d and 35b). This observation seems contradictory due to the higher horizontal resolution, but it is explained by the more stable layered atmosphere that suppresses turbulence.

5.4.2 Surface Heterogeneity Effects on the Atmospheric State

Studies (Maronga and Raasch, 2013; Mironov and Sullivan, 2015; Wenta and Herman, 2018) indicate that the effects of surface heterogeneity structure differ on zero- and first-order quantities and higher-order quantities which is why they are discussed in this section separately. Thereby, the effects are closely related to the underlying surface structure. Thus, a major focus is the analysis of how the air mass evolves over the four areas of pattern #pat1: the *water area*, the *upstream area*, and both *unperturbed areas* (Section 5.3).

Zero- and First-Order Profiles When the structured pattern #pat1 is used as a boundary condition instead of the reference pattern #pat0, the profiles of zero- and first-order bulk quantities change only marginally, as Fig. 36 demonstrates for selected thermodynamic variables. Indeed, outside the surface layer, neither the bulk profile of θ (Fig. 36a) nor the bulk profile of r_v (Fig. 36b) reveals any relevant differences—among both patterns but also among profiles of the individual areas in pattern #pat1. This is of general relevance for two reasons: first, I have discussed in Section 5.3 that all other surface patterns with the same bulk surface properties exert an even less intense effect; second, the small effect on the bulk profiles confirms that both surface patterns provide the same bulk energetic boundary conditions, which in turn allows me an isolated look on the effects of surface structure.

The *water area* and the *upstream area* are directly affected by the oceanic water either through air–surface interactions or by advection from the mean wind. The *unperturbed areas* are only on long-term perspective influenced. Contrary to the higher altitudes, distinct differences among the individual areas are observable in the surface layer (Fig. 36). Here, the profiles of the *unperturbed areas* differ only marginally among each other but can be clearly distinguished from the corresponding profile of the *water area*. The profile of the *upstream area* always lies between the other profiles, being closer to the *unperturbed areas* than to the *water area*. These differences bear immediate relation to the applied surface pattern, which naturally affects the surface layer stronger than higher altitudes. This also explains why the profiles of the *upstream area* are always

located between the other profiles: this area shares the same surface properties as the *unperturbed areas*, but it is also affected by air masses advected from the *water area*.

Within the surface layer, the profiles of the *unperturbed areas* are up to 0.2 g kg^{-1} drier and about 1 K cooler than their counterparts of the *water area*. This warming and humidification with respect to the *unperturbed areas* are due to the oceanic water's sensible and latent heat fluxes from the oceanic water. The profiles of the *water area* roughly equal their bulk counterparts of pattern #pat0 while the other profiles deviate notably. In turn, the corresponding bulk profiles of pattern #pat1 also deviate in the surface layer from the bulk profiles of pattern #pat0.

The condensed water mixing ratios show, like for the DYRF01 and ACRF13 cases, a higher but still small sensitivity to the applied changes than most of the other zero- and first-order bulk quantities. Adding structure to the surface pattern decreases the bulk liquid water mixing ratio r_l within the cloud by up to 6 % and the bulk solid water mixing ratio r_s—and therefore sedimentation—by up to 11.5 % (Fig. 36c). The corresponding decreases in LWP and IWP are 0.3 % and 9.1 %, respectively. The decrease over the *unperturbed areas* is more intense than over the *perturbed areas*. Indeed, the *downstream area* reveals a marginal increase in r_l as a consequence of additional moisture advected from the *water area*. The bulk amount of surface fog increases by about 30 %. This increase is visible in all areas except above the *water area* where—as a consequence of the increased temperature in the surface layer—surface fog nearly vanishes and occurs only at the streamwise leading boundary (not shown

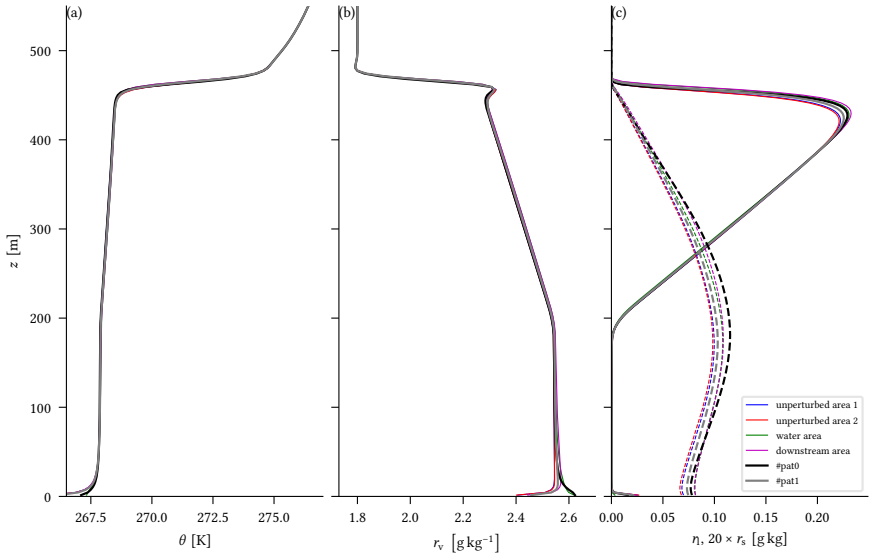

Figure 36: Time-slab averaged profiles of potential temperature θ, water vapor mixing ratio r_v, and liquid (solid) and solid (dash-dotted) water mixing ratios, r_l and r_s.

here). The particular behavior at the leading and trailing edges of the *water area* originates from internal boundary layers building up: over the *water area*, the surface layer is heated, and condensed water evaporates; cold air approaching the *water area*, in particular from the *downstream area* but also from the sides, is only cold enough to provide surface fog until the local temperature in the internal boundary layer reaches the dewpoint. More information on the development of internal boundary layers is given in Section 5.4.4 in the corresponding paragraph, and Fig. 47a visualizes the internal boundary layer. Although *SH* is shown in the figure, displaying *LH* produces the same internal boundary layer features that are also described above.

Higher-Order Profiles Most bulk profiles of higher-order quantities experience strong variations if the surface heterogeneity becomes structured (Fig. 37). I differentiate the effects here, according to the relative position in the ABL, to the surface layer, the cloud-free ABL, the cloudy ABL, and the cloud top. Adding structure to the surface heterogeneity increases the bulk standard deviation, a second-order measure, of most quantities. It is exemplified here by the standard deviations of potential temperature σ_θ and water vapor mixing ratio σ_{r_v}. In the surface layer, the differences in higher-order quantities between both patterns and the individual areas of pattern #pat1 are by far more intense than in all other altitudes. These differences are closely related to those in the profiles of zero- and first-order quantities. For instance, air masses over the *water area* experience strong heating from the surface. In turn, localized intense convection evolves, which produces variations due to the individual convective currents and simultaneously reduces them by turbulent mixing—resulting in "homogeneously distributed variations" compared to the other areas. The higher standard deviation results to a large extent from individual advected plumes, which distinguish intensely from their surrounding air masses.

Within the cloud-free part of the ABL, the large differences between the bulk profiles of both patterns generally reduce. For instance, σ_θ of both bulk profiles decrease relatively abruptly above the surface layer, drastically reducing their difference, and stay roughly constant within the rest of the cloud-free ABL (Fig. 37a). A detailed investigation, however, reveals that bulk difference of σ_θ among #pat0 and #pat1 increases again, barely notable, above about 100 m. Another example is σ_{r_v} which experience a slow but monotonous decrease with height (Fig. 37b). The individual areas of #pat1 experience all these changes with different intensities. For instance, in the profiles of the *unperturbed areas* σ_θ and σ_{r_v} reduce nearly immediately above the surface layer and remain roughly constant within the cloud-free part of the ABL. In

the *perturbed areas*, both decay slower with increasing height. Thereby, the decay with height above the *water area* is generally stronger than the decay over the *downstream area*. Again, this is a consequence of internal boundary layers that form along with the mean wind. They transport the "footprint" of the vertical inhomogeneity to higher altitudes downstream by mixing and vertical propagation of the signals emitted at the surface. This effect occurs not only from the *water area* to the *downstream area* but also vice versa.

At the lower cloud boundary, all investigated higher-order non-cloud quantities experience an intense and abrupt reduction. This reduction occurs in the bulk profiles and in the profiles related to the individual areas of pattern #pat1. It originates from cloud-internal turbulence and processes such as microphysics and radiation, which cause in-plane variations to reduce faster than in the cloud-free ABL. In the cloudy altitudes, all profiles roughly follow the same shape where all investigated higher-order bulk quantities still show higher values for pattern #pat1 than for pattern #pat0. However, the shapes are usually not exactly the same, and the differences between the corresponding bulk profiles of #pat0 and #pat1 generally reduce with increasing altitude.

It is possible to summarize that changing surface heterogeneity structure mainly affects the surface layer, and resulting signals weaken with increasing altitude by turbulent mixing, especially within the cloud. Nevertheless, at the cloud top, the signals are still present and even enhanced compared to the altitudes below. But,

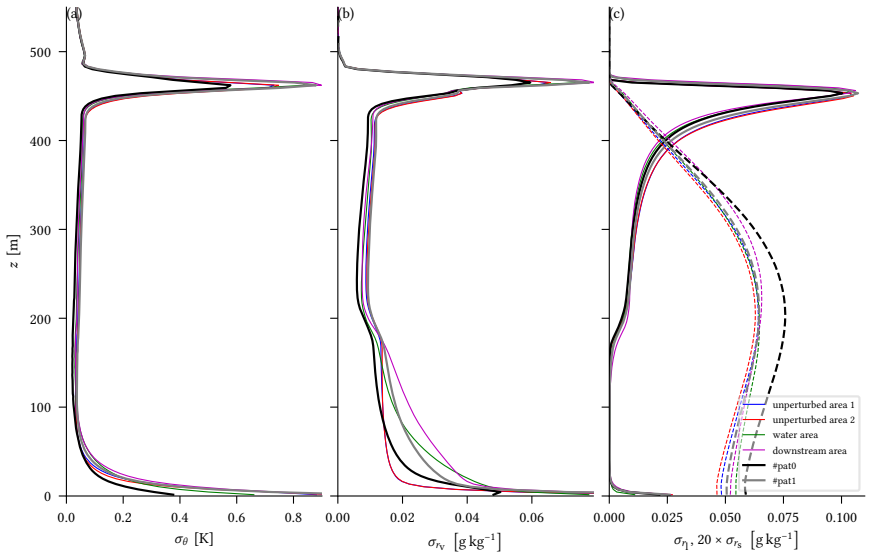

Figure 37: Time-averaged profiles of slab standard deviations of potential temperature σ_θ, water vapor mixing ratio σ_{r_v}, and liquid (solid) and solid (dashed) water mixing ratio, σ_{r_l} and σ_{r_s}.

it is important to note that here higher-order quantities generally show local maxima for three reasons: first, stable layering hinders turbulent mixing and therefore reduction of forming in-plane variations; second, the cloud top marks the interface between ABL and free troposphere, and thus at the corresponding altitudes different air masses are considered while estimating these quantities; third, a variety of non-linear processes—radiation, microphysics, and turbulence—intensely interact with each other and enhance and weaken existing signals extensively. Indeed, the relative difference between the particular area's bulk profiles of higher-order quantities is usually smaller than in the surface layer. More remarkably, at the cloud top, all considered profiles of higher-order quantities are barely distinguishable among both *perturbed areas*. But, they show notably higher values than their counterparts for the *unperturbed areas*, which also barely differ from each other (Fig. 37). Thus, I identify at cloud top a distinct difference between these two regions—though, this difference can also be spotted in other altitudes within the ABL. Therefore, the higher-order quanitity profiles indicate a streamwise elongated structure that affects the quantities differently above the *perturbed areas* and *unperturbed areas*.

Among all higher-order quantities, those related to the condensed water mixing ratios behave different (Fig. 37c). Especially the bulk and individual area profiles of the standard deviation of solid water mixing ratio σ_{r_s} does not reproduce the general features. For example, instead of having peaks in the surface layer and at the cloud top, its curves show no distinct peak but have a weak maximum in the middle of the cloud. Furthermore, the spread among the bulk profiles does not reduce with height. Instead, the bulk profile of pattern #pat1 shows a general decrease by about 25 % in all altitudes. This decrease can be partly explained by the bulk reduction in r_s that I find as a consequence of the structured surface heterogeneity. However, this effect does not account for the whole difference. Another large contributor to the atypical behavior is that cloud processes highly depend on non-linear processes, which might cause linearly compensating changes in the thermodynamic profiles to not necessarily translate to linearly compensating changes in the profiles of cloud quantities. Indeed, these non-linear interactions, generally, can cause the cloud quantities to be very sensitive to small changes in the thermodynamics.

5.4.3 Surface Heterogeneity Effects on Cloud-Top Entrainment and Cloud Structure

I argue in Chapter 4 that stronger gradients at the cloud top intensify CTE. Contrary, structuring surface heterogeneity increases gradients at the cloud top here (Fig. 37),

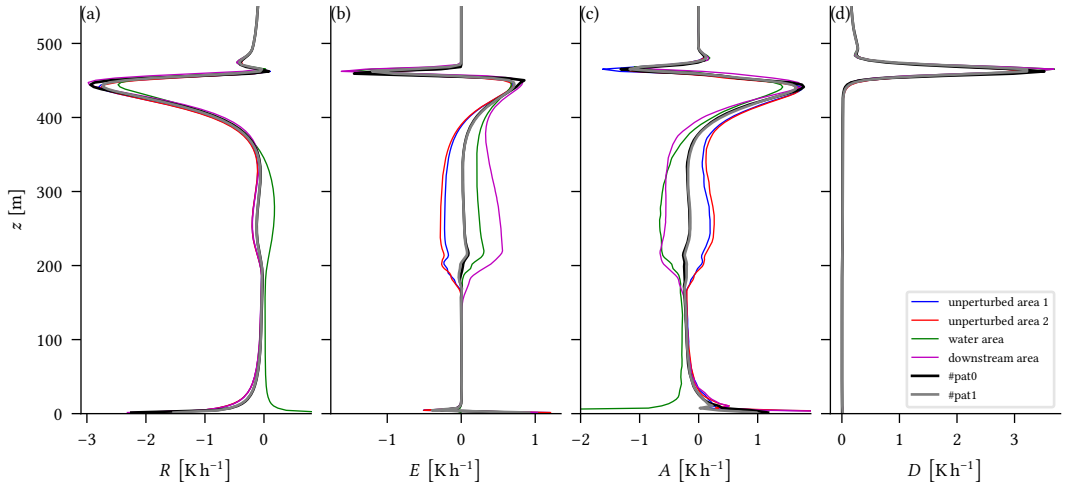

Figure 38: Time-slab averaged profiles of cooling rates due to radiation R, microphysics E, advection A, and subsidence D.

but a corresponding increase of CTE cannot be spotted easily. For example, neither the ABL rises in height nor warms and dries notably. Thus, the amount of condensed water remains roughly the same between both surface patterns (Fig. 36). Though, the condensed water reduces slightly from the unstructured to the structured surface pattern. This relation is contradictory and warrants further investigation.

Analysis of the individual contributors to the cooling rate $\partial_t \theta$ points out that structuring the surface heterogeneity causes all of their bulk values—here the cooling rates due to radiation R, microphysics E, advection A, and large-scale subsidence D are presented[29]—to decrease in their magnitude at the cloud top (Fig. 38). Hence, the individual effects counteract each other, and, indeed, the changes in R, E, and A roughly balance. The effect of structuring the surface heterogeneity on the bulk profile of $\partial_t \theta$ is therefore small and indicates that CTE does not increase with structuring the surface heterogeneity. The corresponding profiles of the individual areas of pattern #pat1 indicate, again, distinct structural differences between the *perturbed areas* and *unperturbed areas*, especially within the cloud. For instance, the *unperturbed areas* experience microphysical heating and advective cooling while the *perturbed areas* show opposite phenomena. I address a similar observation in Section 4.3.4 to buoyancy production and consumption, but this is not the case here (Fig. 39). Instead, the differences in the profiles of the individual areas strongly point to a domain-wide circulation with cold air subsiding over the *unperturbed areas* and warm air ascending over the *perturbed areas* (Fig. 38b,c).

[29] The contribution of SGS is not discussed here. It is comparatively low and shows no dedicated sensitivity to the surface heterogeneity structure. Also, the contribution of numerics is not discussed here for two reasons: first, its contribution is even less than the one of SGS; second, its reasons are purely related to numerics and not to physics.

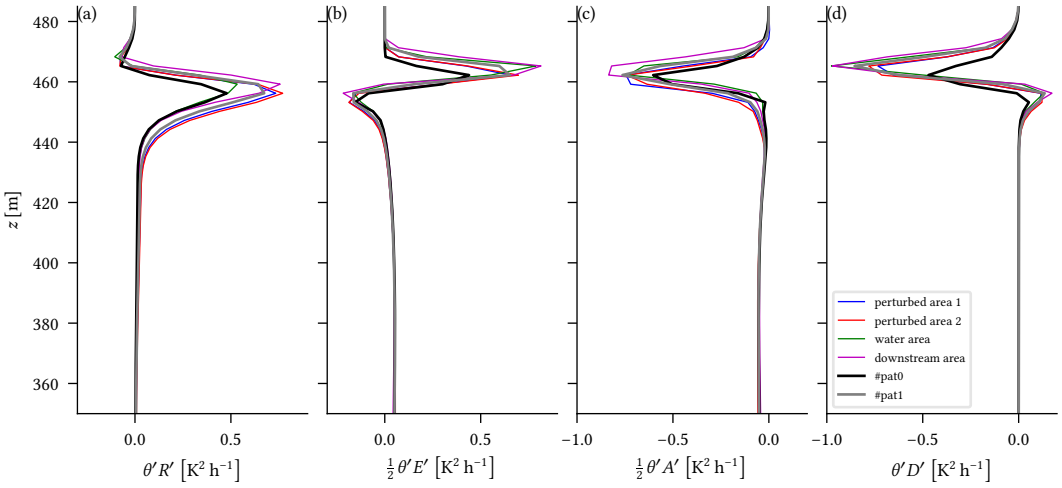

Figure 39: Time-slab averaged profiles of buoyancy production due to radiation $\theta' R'$, microphysics $\theta' E'$, advection $\theta' A'$, and sub-grid scale $\theta' S'$.

While the profiles of $\partial_t \theta$ support the observations of a non-existent effect of structuring surface heterogeneity on CTE, their counterparts[30] describing the production of potential temperature variance $\partial_t \sigma_\theta^2$ as defined in Eq. 69 strongly indicate higher CTE. For instance, the cutout presented in Fig. 39 indicates a slightly, one to two grid points, higher ABL for the simulation utilizing pattern #pat1. This increase in ABL height is a strong indicator of increased CTE, which can also be seen in most profiles of other quantities if the same cutout is applied. The individual areas of pattern #pat1 deviate neither strongly nor systematically from their corresponding bulk profiles (Fig. 39).[31] Although the total values of $\partial_t \sigma_\theta^2$ indicate no sensitivity towards changes in surface heterogeneity structure, its individual contributors experience strong increasing magnitudes at the cloud top from pattern #pat0 to pattern #pat1 (Fig. 39), which counteract each other to a large extent.

Indeed, the individual components of $\partial_t \sigma_\theta^2$ increase by up to 50 % at the cloud top for the bulk values of the individual areas. Thereby, the increase due to radiation is roughly the same for all areas but the *water area* (Fig. 39a), which falls in line with its corresponding anomaly in the profile of R (Fig. 38a). It might be a consequence of the missing radiation fog or the lower surface albedo compared to the other areas. Of course, the anomaly can also arise from cloud physics, such as a different distribution of solid and liquid hydrometeors but the profiles presented here (Fig. 36c) and the distributions of LWP and IWP support no such hypothesis.

[30] Again, I do not present contributions of SGS and numerics because they are comparatively low and show no dedicated sensitivity to the surface heterogeneity structure.

[31] The profile of the *downstream area* reveals a small outlier at the cloud top where advection consumes more σ_θ^2 than the other areas indicate. This outlier is counteracted by the other areas, respectively.

In the microphysical component, again, the profiles of the *perturbed areas* can be distinguished at the cloud top from their counterparts of the *unperturbed areas* and show accordingly higher values (Fig. 39b). The sum of all contributors to $\partial_t \sigma_\theta^2$ remains roughly the same between both utilized surface patterns. Thus, the increase in production of σ_θ^2 due to radiation and microphysics has to be consumed. Advection and large-scale subsidence are the main consumers. Consumption due to advection increases about 25 % from pattern #pat0 to pattern #pat1 and consumption due to large-scale subsidence increases by about 100 %. The individual areas show no notable spread in advection besides the *downstream area*, which marks a small outlier and provides more intense consumption. The profiles of large-scale subsidence indicate, again, a streamwise elongated structure, with the profiles of the *perturbed areas* showing a higher magnitude than their counterparts of the *unperturbed areas*.

The combination of increased production of σ_θ^2 by radiation and microphysics with increased consumption by dynamical processes points to the horizontal resolution sensitivity study performed in Chapter 4. I conclude, therefore, that structuring surface heterogeneity enhances CTE. In the case of structured surface heterogeneity, the profiles of the *perturbed areas* not only clearly distinguish for most higher-order quantities from their counterparts of the *unperturbed areas*. Even more, they show for several variables (Fig. 39a,b, Fig. 38b,d) a slightly higher ABL height. Both phenomena are again indicators for a streamwise difference between the *perturbed areas* and *unperturbed areas*. A first glance at the instantaneous snapshots of LWP (Fig. 40) questions if such a structure is evolving at all. The individual cloud patches simulated over pattern #pat1

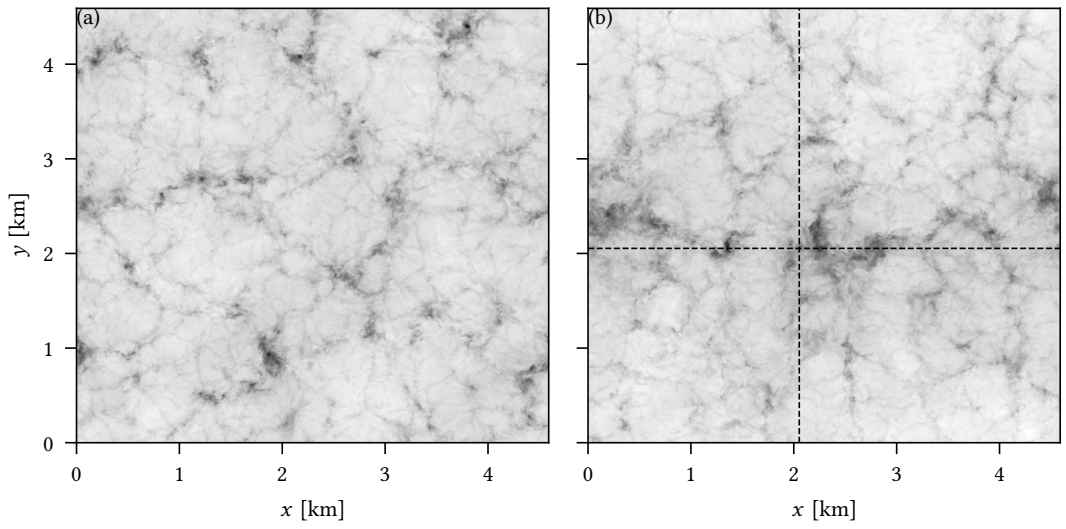

Figure 40: Instantaneous snapshot of liquid water path LWP [0 g m^{-2} (black) to 65 g m^{-2} (white)] at the end of the simulations utilizing the unstructured reference pattern #pat0 (left) and the structured pattern #pat1 (right). The dashed lines in pattern #pat1 separate the individual areas defined in Section 5.3.

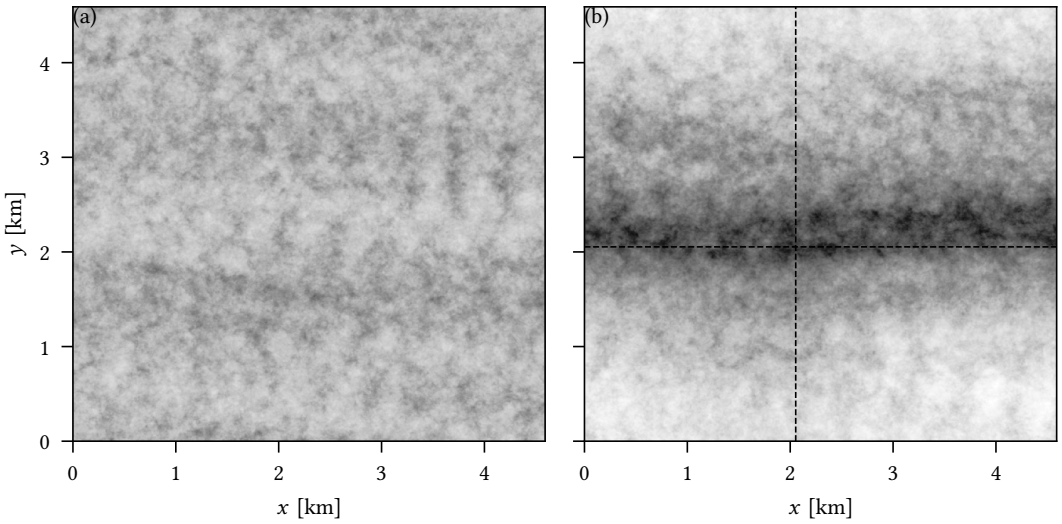

Figure 41: Liquid water path LWP [35 g m^{-2} (black) to 50 g m^{-2} (white)] averaged over the third and fourth hour of the simulations utilizing the unstructured reference pattern #pat0 (left) and the structured pattern #pat1 (right). The dashed lines in pattern #pat1 separate the individual areas defined in Section 5.3.

(Fig. 40b) differ only marginally from those simulated over pattern #pat0 (Fig. 40a) and show similar magnitudes. The Sc acts like a filter on the surface heterogeneity structure because it is not possible to determine if there is a difference between the utilized surface patterns at all and how the difference looks like. In fact, the accumulation of all oceanic water in #pat1 can not be identified in the Sc. If at all, the only structure visible in the instantaneous values of LWP is a local minimum close to the boundary between the *perturbed areas* and the *unperturbed areas* (Fig. 40b).

This barely noticeable local minimum, however, might be randomly appearing and is likely to attract attention only because the underlying surface heterogeneity structure is known. To evaluate if it is randomly appearing, I visualize in Fig. 41 the time-averaged LWP. It reveals a distinct minimum over #pat1, contrary to #pat0 where it is distributed homogeneously. That minimum of LWP is located at the boundary between the *perturbed areas* and the *unperturbed areas*. It extends about 200 m in the north–south direction and over the whole domain streamwise. Therefore, the time-averaged LWP confirms the so far only indicated streamwise elongated structure within the Sc. The structure superposes the individual cloud patches and falls in line with my observations from the individual area profiles of higher-order quantities (Section 5.4.2 and 5.4.3). However, even the time-averaged LWP provides no information on the underlying accumulated oceanic water because the evolving structure is elongated streamwise instead of reproducing the square structure of the accumulated oceanic water.

The observed structure is not only visible in LWP but also in various other integrated and non-integrated variables, such as IWP, or vertically integrated TKE. It usually becomes easily spottable in time-averaged quantities but is also observable for several instantaneous quantities. Not all quantities are directly correlated to the structure as it is represented in LWP. For instance, vertically integrated TKE is affected by a north-south shift (Fig. 42b). Its maxima are located next to, but not within the minimum of LWP. The maximum located in the *perturbed areas* is, thereby, more intense than the one located in the *unperturbed areas*. In general, TKE experiences a strong increase compared to pattern #pat0 (Fig. 42a), which agrees well with the observation that higher-order quantities show, in general, higher values in all altitudes (Section 5.4.2).

Like for the ACRF13 case (Fig. 29), void-depth ratio d_v/d_z (Eq. 66), a measure of engulfment, is maximum at the cloud boundaries (Fig. 43). Indeed, it is assumed to be closely related to the minimum in LWP. However, engulfment also shows notable deviations from this assumption. For instance, values arise at a certain distance from the expected maximum over the *unperturbed areas* but tend to vanish directly next to it over the *perturbed areas* (Fig. 43). Indeed, engulfment should not be limited strictly to the minimum in time-averaged LWP because the individual cloud patches are still far smaller than the individual areas. Therefore, cloud boundaries also occur within them (Fig. 40b). The observed distribution of engulfment likely arises from a general circulation pattern because naturally, engulfment appears less frequently in areas with

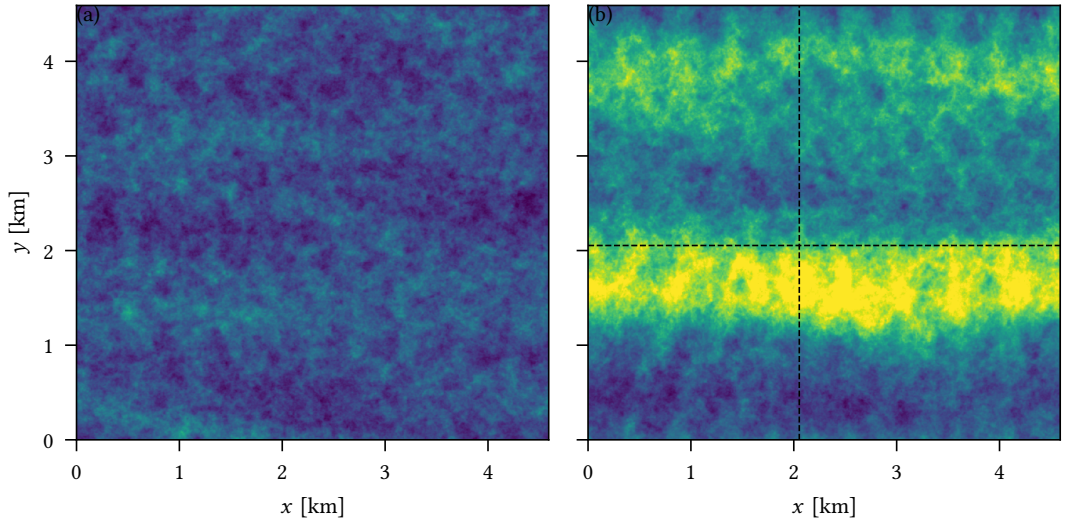

Figure 42: Vertically integrated total turbulent kinetic energy $\int_z TKE_t$ [70 $m^3\ s^{-2}$ (blue) to 150 $m^3\ s^{-2}$ (yellow)] averaged over the third and fourth hour of the simulations utilizing the unstructured reference pattern #pat0 (left) and the structured pattern #pat1 (right). The dashed lines in pattern #pat1 separate the individual areas defined in Section 5.3.

uprising air masses than in areas with subsiding air masses. Contrary to the ACRF13 case, the observed increase in CTE causes bulk engulfment to decrease here by about 13 %.

5.4.4 Circulation Pattern and Heat Fluxes over Structured Surface Heterogeneity

The preceding sections describe the effects of surface heterogeneity structure on Sc and ABL. For the presented surface patterns, these effects are far-reaching: a streamwise elongated structure evolves in the whole domain, leading to increased CTE (Section 5.4.3), less precipitation, and changes in the surface temperature (Section 5.4.2). The evolution of such a structure is not captured by traditional Arctic lead theory (Glendening and Burk, 1992; Michaelis et al., 2020). It also correlates not with the surface heterogeneity as studies of mid-latitude convective ABLs indicate for low-wind cases (Maronga and Raasch, 2013). Instead, the streamwise elongated structure resembles features occurring in high-wind cases, which is contradictory. The effects of the evolving structure are neither negligible nor fully explained by known theories, which is why I analyze here how the surface heterogeneity structure affects the evolution of Sc and ABL. Therefore, I limit my analysis to the circulation pattern and the sensible heat flux SH. Still, the same analysis can be performed for most other quantities, especially for the latent heat flux, and yields similar results.

The unstructured pattern #pat0 is affected by a horizontal homogeneous sensible heat

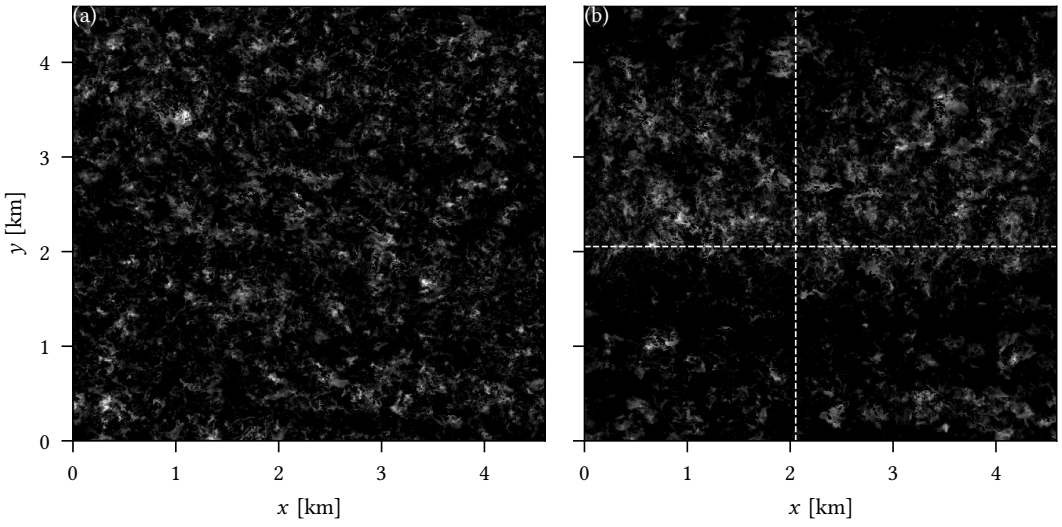

Figure 43: Void-depth ratio d_v/d_z [0 % (black) to 2.5 % (white)] averaged over the third and fourth hour of the simulations utilizing the unstructured reference pattern #pat0 (left) and the structured pattern #pat1 (right). The dashed lines in pattern #pat1 separate the individual areas defined in Section 5.3.

flux (Fig. 44) which is estimated via

$$SH = \rho T' w' c_p \tag{71}$$

with temperature T, specific heat capacity of air $c_p = 1004.5\,\mathrm{J\,kg^{-1}\,K^{-1}}$, and density of moist air ρ. In general, SH increases from the surface ($SH = -1\,\mathrm{W\,m^{-2}}$) to the cloud top ($SH = 18\,\mathrm{W\,m^{-2}}$). Parallel to the mean wind, no stationary circulation evolves (Fig. 44a). Contrary, perpendicular to the mean wind, stationary but weak roll-like circulations evolve, which roughly seize the size an individual cloud patch (Fig. 44b). These steady circulations are a common feature of Arctic convective flows as they occur, for example, in a stronger form during cold-air outbreaks. Here, they form from heat fluxes and motions caused by the utilized specific distribution of oceanic water.

In case the surface heterogeneity becomes structured in the form of pattern #pat1, the relatively homogeneous circulation pattern, compared to the mean wind, as well as the horizontal homogeneous heat flux experience dramatical changes: a strong secondary circulation perpendicular to the the mean wind (Fig. 46b,d) and internal boundary layers (Fig. 46a) evolve.

Secondary Circulation High surface heat fluxes over the *water area* cause a corresponding negative pressure anomaly of less than 2 Pa to build up, which is similar to a thermal low (Fig. 45a). While the pressure anomaly is too small to notably influence the mean wind, which is mainly constrained by the geostrophic forcing, it induces a secondary circulation $\mathbf{v}' = (u', v', w')^T$ in the whole domain. The secondary circulation, is on average, to a large extent perpendicular to the mean wind. Close to the surface, the pressure anomaly causes convergence and, in turn, updrafts along a characteristic horizontal x-shape over the *perturbed areas* (Fig. 45a). The maximum of convergence, the location where both lines cross, is located over the *downstream area*. This location

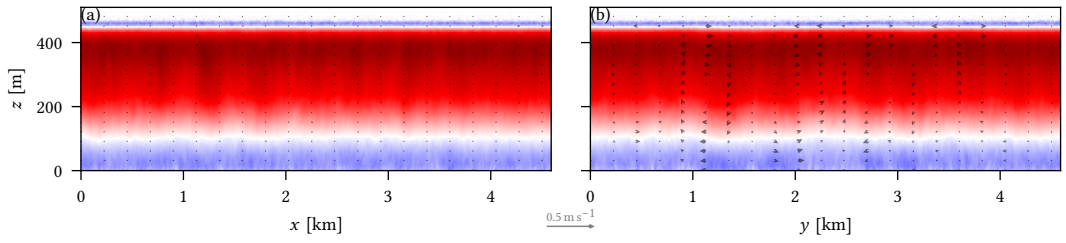

Figure 44: Averaged values for sensible heat flux SH [$-20\,\mathrm{W\,m^{-2}}$ (blue) to $20\,\mathrm{W\,m^{-2}}$ (red)] and circulation anomaly (arrows) over pattern #pat0. Panel (a) visualizes the average along the y-axis, and the corresponding averaged circulation anomalies (u', w'). Panel (b) visualizes the average along the x-axis, and the corresponding averaged circulation anomalies (v', w').

of maximum updraft is not only determined by the surface heat fluxes but also a consequence of the mean wind and development of internal boundary layers. They transport the "footprint" of the surface signals to higher altitudes downstream along $\phi_h = 96^\circ$ (Fig. 34b) by mixing and vertical propagation. The downstream transport also causes the slightly southern shift of the maximum of convergence, which would be expected otherwise in the north–south middle of the *perturbed areas*.

A streamwise elongated divergence zone counteracts the arising updrafts at the surface and is highly correlated to the minimum in LWP. Consequently, the induced near-surface wind anomalies are mostly one-dimensional along the north–south direction. They strengthen especially above the boundaries between the *perturbed areas* and *unperturbed areas* because at these locations the pressure gradients, induced by the pressure anomaly, are most intense. Remarkably, SH is not only correlated to the updrafts within the surface layer. In fact, it is also correlated to the underlying surface type. Thus, positive values of SH occur mostly in the *water area* (Fig. 45b). Indeed, although the updrafts are also strong along the convergence zone over the *downstream area*, these updrafts are correlated to negative values and carry therefore cold air.

The correlation between SH and surface type shifts slightly downstream with increasing altitude due to the formation of internal boundary layers. These vertically propagate the corresponding signals while following the mean wind. Above the surface layer, the former highly localized variations of the updrafts blur quickly with increasing altitude. They merge into each other and produce a roughly homogenously

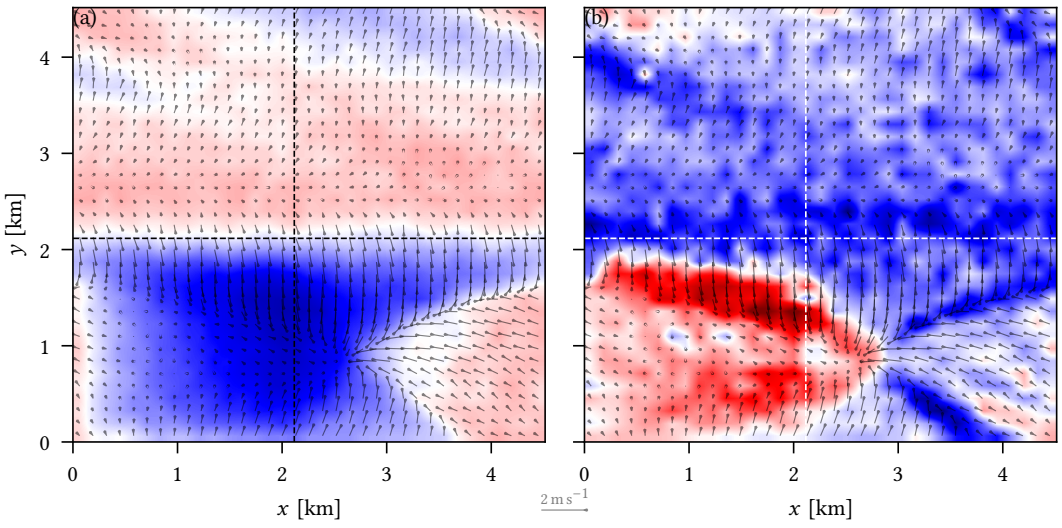

Figure 45: Panel (a) visualizes dry air pressure anomaly p' [−2 Pa (blue) to 2 Pa (red)] at the lowest level. Panel (b) visualizes the corresponding heat flux SH [−20 W m^{-2} (blue) to 20 W m^{-2} (red)]. The arrows symbolize near-surface wind anomaly (u', v'). The dashed lines separate the individual areas defined in Section 5.3.

uprising air mass above the *perturbed areas*. The uprising air masses experience a sharp boundary above the zone with divergence at the surface. This location is in the higher altitudes marked by a strong downdraft that still correlates with the minimum in time-averaged LWP. Within the downdraft, SH is intense and also positive (Fig. 46b,d). Thus, the downdraft carries cold air from the upper ABL to the surface. The *unperturbed areas* generally show no homogeneous uprising or subsiding air masses in higher altitudes but many individual areas with updrafts and downdrafts. These areas are related to individual cloud patches and will blur if longer periods are considered. Close to the central downdraft zone, longer periods will result in an area without vertical motion on average. However, the share of updrafts increases with distance from the downdraft zone due to the turbulent mixing of air masses from the *perturbed areas*. Close to the cloud top, SH as well as the vertical circulation anomaly weaken, and a horizontal pattern evolves opposite the surface circulation anomaly.

Summarized, pattern #pat1 causes a strong secondary circulation to evolve, which consists of two major cells along the background wind. Thus, the resulting circulation among them is perpendicular to the background wind and the circulation's wind speeds at the surface and cloud top exceed 0.6 m s^{-1}, which is more than one-third of the background wind (Fig. 47b,d). Contrary, along the background wind, heterogeneity-induced motions are mainly of vertical nature: uprising over the *perturbed areas* and subsiding over the *unperturbed areas* (Fig. 47a,c). Though, heterogeneity-induced motions converging at the interface between sea ice and oceanic water can be spotted

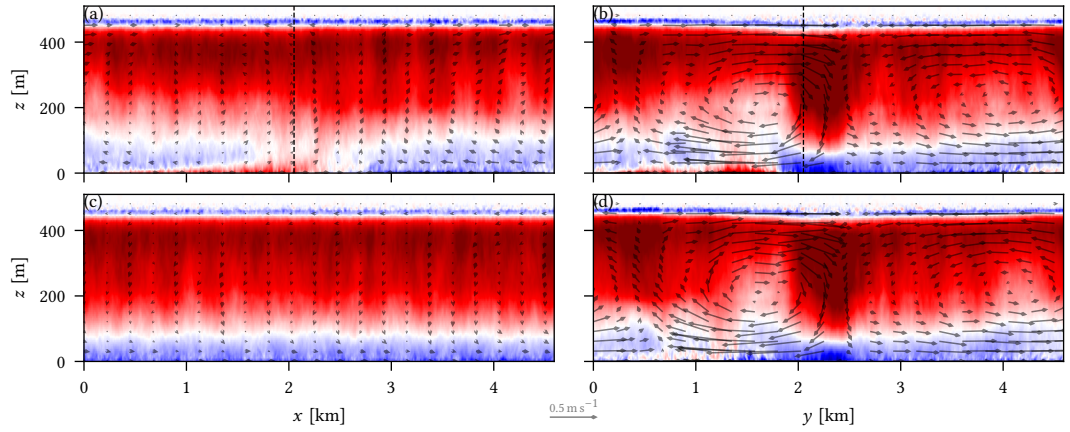

Figure 46: Averaged values for sensible heat flux SH [−20 W m^{-2} (blue) to 20 W m^{-2} (red)] and circulation anomaly (arrows) over pattern #pat1. Panels (a) and (c) visualize the average along the y-axis, and the corresponding averaged circulation anomalies $\left(u', w'\right)$. Panels (b) and (d) visualize the average along the x-axis, and the corresponding averaged circulation anomalies $\left(v', w'\right)$. The top panels are averaged over the *perturbed areas*, and the bottom panels are averaged over the *unperturbed areas*. The vertical dashed lines in the top panels mark the boundary between ocean water (left) and ice sheet (right).

near the surface over the *perturbed areas*. These motions is weaker than the perpendicular motions and arises from the pressure gradient between the *water area* and the *downstream area* (Fig. 45a and 46a).

SH is homogeneously distributed over pattern #pat0 because of the "randomly" evolving cloud patches and their related up- and downdrafts. Contrary, its heterogeneity-induced distribution over pattern #pat1 is strongly correlated to the secondary circulation (Fig. 47). For instance, a distinct streamwise prolongated downdraft area in the middle of the domain carries cold and dry air. This downdraft dominates the motions occurring over the *unperturbed areas* and, therefore, explains the corresponding profiles of *A* (Fig. 38c). Contrary, updrafts over the *perturbed areas* carry mostly warm and moist air, which explains the observed advective heating over this area. The observed differences in the heating rate profiles due to microphysics (Fig. 38b) result, in turn, mainly from condensation and evaporation dominating the regions with up- and downdrafts, respectively.

Development of Internal Boundary Layers The formation and evolution of internal boundary layers fall perfectly in line with traditional theories on Arctic leads (Glendening and Burk, 1992; Michaelis et al., 2020) and are outlined in the paragraphs below. Although these theories confine the growth of internal boundary layers to ABL height—which might increase as a consequence of internal boundary layer development—here, the vertical evolution of the internal boundary layers is confined

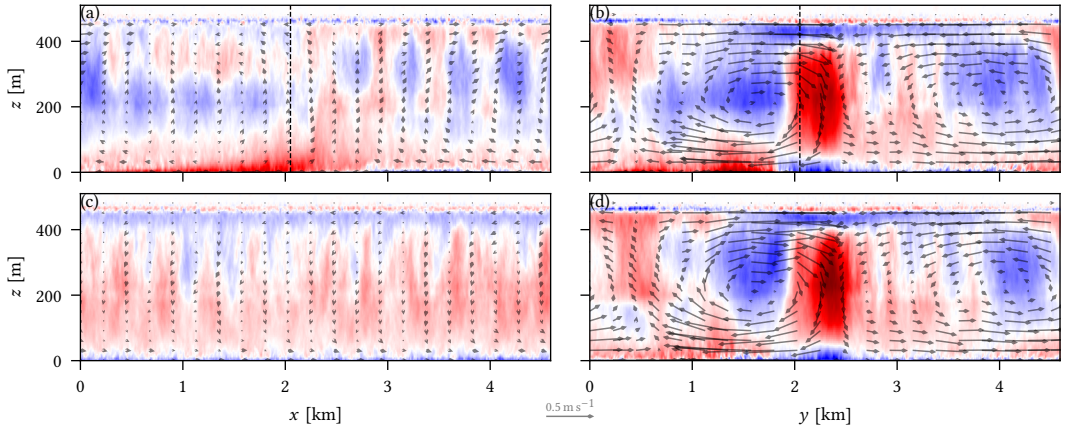

Figure 47: Averaged values for heterogeneity-induced sensible heat flux anomaly SH_{hi} [$-20\,\mathrm{W\,m^{-2}}$ (blue) to $20\,\mathrm{W\,m^{-2}}$ (red)] and circulation anomaly (arrows) for pattern #pat1. Panels (a) and (c) visualize the average along the y-axis, and the corresponding averaged circulation anomalies $\left(u'_{\mathrm{hi}}, w'_{\mathrm{hi}}\right)$. Panels (b) and (d) visualize the average along the x-axis, and the corresponding averaged circulation anomalies $\left(v'_{\mathrm{hi}}, w'_{\mathrm{hi}}\right)$. The top panels are averaged over the *perturbed areas*, and the bottom panels are averaged over the *unperturbed areas*. The vertical dashed lines in the top panels mark the boundary between ocean water (left) and ice sheet (right).

by the lower boundary of the Sc. The development of internal boundary layers is crucial for the observed secondary circulation. It explains why this weak-wind case evolves roll-like structures as it is only indicated for strong-wind cases (Maronga and Raasch, 2013).

The development of internal boundary layers is trackable, for example, by SH (Fig. 46a) or its heterogeneity-induced counterpart SH_{hi} (Fig. 47a). One internal boundary layer carries moisture and heat from the intense oceanic heat fluxes over the *water area* to higher altitudes by vertical propagation and mixing. The mean wind superposes the vertical transport of these signals. It is the combination of turbulent vertical transport and mean horizontal advection which causes not the higher altitudes of the *water area* but instead the higher altitudes of the *downstream area* to be heated and moistened from the considered internal boundary layer. The opposite effect, to a lesser extent, results from a cold and dry internal boundary forming over the *downstream area* and being advected to the *water area*. Remarkably, the internal boundary layer originating from the *water area* is even visible above the internal boundary layer originating from the *downstream area*.

Once the internal boundary layers reach the lower Sc boundary, their corresponding signals vanish and blur to the homogeneous heat flux observed over the *perturbed areas*. This transition causes the surface heterogeneity structure to transform to the streamwise elongated structure. Therefore, it is the key process that causes the ABL to "feel" the effective surface pattern—the streamwise averaged surface pattern (Maronga and Raasch, 2013)—instead of the actual surface pattern. Further investigation on this phenomenon is required, but my results indicate that it is caused likely from the combination of weak vertical motion compared to convective ABLs on the one side and intense turbulent mixing induced by cloud processes on the other side.

5.4.5 Effects on the Surface

Sc and surface closely interact with each other (Section 1.1), and changes in the Sc inevitably affect the surface water and energy balance. The corresponding bulk effects on the domain are roughly outlined below and represent the effects mesoscale or climate models "feel". They can not represent non-bulk variables of my simulations because of their comparatively lower resolution. The results of this analysis have to be interpreted with suspicion for two reasons: first, the surface properties are kept constant throughout the simulations. Thus, the surface cannot respond to atmospheric changes, for instance, by freezing or melting; second, I analyze here merely the bulk effects, but high variations in the domain are observed (Fig. 48). Both, the

missing surface responses and the neglected in-plane variations suppress potentially surface developments and signals, which may enhance or dampen the here discussed observations in theoretical considerations or with advancing simulation.

Structuring the surface heterogeneity reduces precipitation by about $0.0005\,\mathrm{mm\,h^{-1}}$. This decrease is not much in absolute numbers but equals roughly a decrease of 5 % given the generally low precipitation of $0.0105\,\mathrm{mm\,h^{-1}}$. Its over- or underestimation with respect to the surface heterogeneity structure causes, for example, erroneous prediction of fresh-fallen snow, which affects not only the production of sea ice but, for instance, also the surface albedo or the corresponding heat fluxes.

The surface energy balance is given here by

$$HFX = SH + LH + R_{\mathrm{LW}} + R_{\mathrm{SW}} \tag{72}$$

with LH the latent heat flux, R_{LW} the long wave radiative flux, R_{SW} the short wave radiative flux, and HFX the resulting surface heat flux which induces, for example, melting of ice or propagates to the lower surface layers. In the presented simulations, the largest contributors to HFX are $R_{\mathrm{SW}} \approx -94\,\mathrm{W\,m^{-2}}$ and $R_{\mathrm{LW}} \approx -14\,\mathrm{W\,m^{-2}}$. Both radiative fluxes are directed to the surface and therefore cause surface warming. Contrary, SH and LH show magnitudes of less than $2\,\mathrm{W\,m^{-2}}$ with LH cooling the surface and SH warming the surface.

Structuring the surface heterogeneity causes the surface to experience a 0.43 % stronger cooling, which equals about $0.47\,\mathrm{W\,m^{-2}}$. These numbers also do not seem large, but the cooling in principle accumulates. It may cause the near-surface air temperatures to

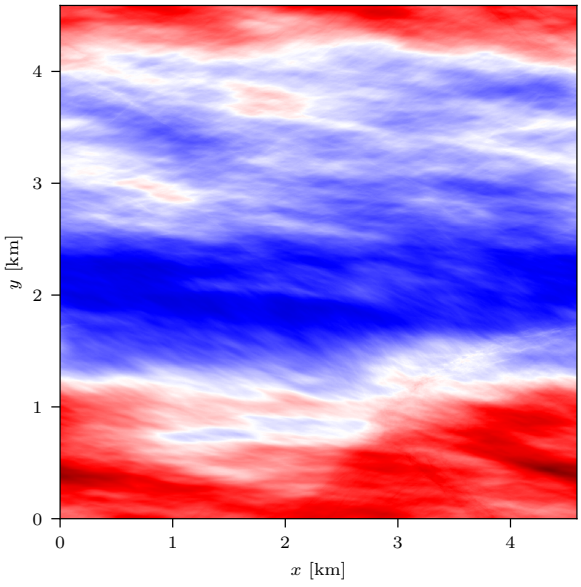

Figure 48: Heterogeneity-induced precipitation anomaly P_{hi} [$-0.018\,\mathrm{mm\,h^{-1}}$ (blue) to $0.018\,\mathrm{mm\,h^{-1}}$ (red)] as defined in Eq. 70 for pattern #pat1.

cool by up to $-1.4\,\mathrm{K\,h^{-1}}$ if no additional heat fluxes from other surface processes such as freezing or propagation from the lower surface layers arise. The observed changes in HFX originate to a large extent, more than 90 %, from changes in SH which intensifies by about 55 %. The other components of the surface energy balance experience only marginal changes of less than 5 %. The observed hypothetical temperature change is large and illustrates the need to utilize a surface model which allows the surface to respond accordingly.

Chapter 6

Conclusion

The presented work utilizes highly-resolved LES to investigate the representation and effects of small-scale processes on Sc. The studies and their results can be separated into three major parts. I first set up and modified the LES mode of WRF 4 (Chapter 2). I evaluated its capabilities to simulate Sc on highly-resolved grids by applying it to the well-known and in detail investigated DYRF01 case (Chapter 3). Subsequently, I defined a new Arctic Sc case during spring, the ACRF13 case, based on the recent field campaigns ACLOUD and PASCAL. I applied the modified model to this case and performed a resolution sensitivity study on it, which covers one magnitude in horizontal resolution from frequently used 35 m to highly resolved 3.5 m (Chapter 4). For the last study, I modified the ACRF13 case to analyze the effects of surface heterogeneity structure on Sc and ABL. Two different surface patterns were investigated, which represents the limiting cases of heterogeneity structure (Chapter 5). The main findings related to each research objective defined in Section 1.3 are summarized in the paragraphs below. I end this chapter with a concluding remark.

O1: Can WRF-LES' simulate cloud-driving processes for mixed-phase Sc, and how are the results affected by horizontal resolution?

I modified the WRF's LES algorithm to perform the simulations and provide additional output variables and input parameters, which support the simulation data analysis. The inclusion of large-scale subsidence and the choice of a distinct microphysical time step are the main modifications to the LES algorithm. Here, large-scale subsidence acts as an idealized, constant physical forcing parameter rather than the nudging term already implemented in WRF. The microphysical time step is needed for the combination of small time steps, microphysical parameterization, and compressibility of the model. Otherwise, these settings cause density–pressure waves in response to frequent changes in hydrometeor species concentrations. These density–pressure waves may intensify, thus causing numerical instability.

A thus modified version of WRF, WRF-LES, containing the core modifications, is applied with horizontal resolutions of 35.0 m, 10.0 m, and 3.5 m to the well-known and in detail investigated DYRF01 case as defined by (Stevens et al., 2005). It reproduces the main features of earlier studies (Stevens et al., 2005; Yamaguchi and Feingold, 2012; Matheou and Chung, 2014; Heinze et al., 2015; Pedersen et al., 2016; Pressel et al., 2017; Mellado et al., 2018) for all applied horizontal resolutions, such as a non-precipitating and thickening Sc. The bulk quantities are mostly within the standard deviation of the ensemble presented in Stevens et al. (2005). Thereby, the results indicate a resolution convergence of the simulations only for a horizontal resolution below 10 m which is not further investigated in this study but similar to findings for the benchmark case defined based on the ACRF13 case.

O2: Define and evaluate a semi-idealized mixed-phase Sc case during Arctic spring that is suitable for LES.

Based on the recent field campaigns ACLOUD and PASCAL, I define a new benchmark case, the ACRF13 case, for Arctic mixed-phase Sc. The case is characterized by a two-layer structure for potential temperature and water vapor mixing ratio and a one-layer structure for geostrophic forcing. The lower boundary condition is a homogeneous ice surface. The well-mixed ABL reaches up to an altitude of 470 m and contains a mixed-phase cloud, which is mostly liquid and produces weak solid sedimentation. Subsequent simulations for this case support my choice of initialization profiles and demonstrate the case's suitability for process-based investigation of mixed-phase Arctic Sc.

O3: Which processes drive CTE in Arctic Sc?

[32]Sc CTE is generally driven by wind shear, microphysics, and radiation (Mellado, 2017). In the presented ACRF13 case, wind shear is found negligible. A detailed analysis of the microphysical cooling profiles unveils a characteristic s-shape with slight warming just below the cloud top caused by microphysics. This shape slightly differs from the prototypical profiles that emerged from equilibrium microphysical considerations over the past years (Mellado, 2017). I suggest that this is due to accumulated supersaturation in updrafts being released close to the cloud-top region and different microphysical processes acting in updrafts and downdrafts. Both aspects illustrate the importance of non-equilibrium microphysical effects if such subtleties of the cloud-top region are of interest. Further, I find that the dominant role of cloud-top interfacial microphysical

[32]Large parts of this section are excerpts of Rauterkus and Ansorge (2020); see footnote 21.

processes, found here, is a peculiarity of the Arctic environment where the low optical thickness of the cloud renders radiation as the cloud-driving process overall relatively less important than in low-latitude Sc.

O4: Which processes cause sensitivity of Sc to horizontal resolution?

[33]My resolution-sensitivity study for the benchmark case ACRF13 covers one magnitude in horizontal resolution. I show that increasing the horizontal resolution from 35 m to 3.5 m causes a slightly warmer and drier atmosphere and, therefore, a decrease in liquid and ice water paths of about 15 % after six hours of simulation. Those differences are rather small but can lead to a collapse or break-up of Sc if located close to its transition regime. Process-based analysis of the LES data shows that the observed changes arise from more spatial variability, which improves three aspects of the LES process-level representativity of Sc, and especially that of CTE.

- First, the increased representation of spatial variability allows to resolve parts of the inertial cascade of turbulent motion without notable numerical dissipation. This holds for the whole domain but is in particular crucial for the cloud top, where the model relies heavily on the SGS parameterization. The wavenumber dependence of anisotropy suggests that resolving motion at scales of $\mathcal{O}(10\,\mathrm{m})$ is crucial to simulate CTE correctly; parameterization of this behavior based on resolved-scale properties does not seem possible using standard turbulence parameterization. At the same time, the convergence of bulk and entrainment statistics beginning for case #10.0m also suggests that it is sufficient to resolve part of the dynamics at this scale—on the order of few meters in the case of the benchmark case introduced here—for a correct representation of CTE.

- Second, the extended range of resolved turbulence allows smaller turbulent eddies, which, in turn, produce more engulfment of free tropospheric air into the cloud layer.

- Third, a higher resolution increases the resolved spatial variability in the atmospheric variables. These variations increase by non-linear relationships to an even higher spatial variability in microphysical cooling, which, in turn, causes buoyant instability and, therefore, triggers turbulent eddies.

All three aspects are closely connected through the production of and being driven by turbulence which outlines the importance of a valid SGS parameterization.

[33]Large parts of this section are excerpts of Rauterkus and Ansorge (2020), including the wording. For more information on my contribution, see footnote 21.

O5: How does surface heterogeneity affect Arctic Sc

I investigate two surface patterns consisting of 20 % open water and 80 % sea ice and differing only in their degree of heterogeneity structure. The reference pattern, where patches of oceanic water and ice sheets are randomly distributed, is first compared with the original ACRF13 case, which got modified to enhance signals originating from the implemented surface patterns. The simulated Sc is mostly liquid and produces weak solid sedimentation. As a consequence of the cooled surface, the ABL is slightly cooler and more stable in the modified case.

Structuring the surface heterogeneity by accumulating all oceanic water in one squared area is shown to affect the bulk zero- and first-order quantities only marginally. Effects are limited to the surface layer or highly sensitive quantities such as those directly describing cloud properties such as liquid water mixing ratio. The bulk values of higher-order quantities, on the contrary, increase by up to 100 % for selected variables and result in a slight increase of CTE. The effects of surface heterogeneity structure are observed to be most intense in the surface layer and vanish—due to turbulent mixing—with increasing altitude, especially within the cloud. At the cloud-top, the signals of the surface patterns are again enhanced. They reveal distinct differences between the profiles over perturbed and unperturbed areas with respect to the accumulated oceanic water.

In the case of accumulated open water, a secondary circulation forms perpendicular to the mean wind, which has a strength of about one-third of the mean wind speed at the cloud top and in the surface layer. The observed secondary circulation consists of two cells that affect the whole ABL and cause a streamwise roll-like structure to evolve in the ABL and the Sc. It, therefore, bears no geometric resemblance to the surface forcing. The formation of this structure is not captured by traditional Arctic lead theory (Glendening and Burk, 1992; Michaelis et al., 2020) and disagrees with studies of lower-latitude cloud-free ABLs (Raasch and Harbusch, 2001; Maronga and Raasch, 2013). Indeed, such roll-like structures due to secondary circulations are expected for high mean wind speeds, which in turn cause the ABL to only “feel” the streamwise-averaged surface pattern. Instead, a correlation of surface heterogeneity and circulation is expected for low wind speeds, like in the presented case (Maronga and Raasch, 2013). The first analysis of this discrepancy reveals the cloud-induced turbulence in combination with comparatively weak vertical motion to cause the streamwise “smudging” of the surface heterogeneity signals.

Concluding Remarks

The presented studies outline the appreciable value of LES for process investigation of Sc configurations for increasing complexity in terms of external forcing and surface heterogeneity. However, they also show—in accordance Mellado et al. (2018)—that LES can converge in zero-order and first-order statistics even though underlying assumptions are violated or crucial processes are non-resolved. Therefore, the results of LES have to be always analyzed with caution because correct profiles do not necessarily imply physical correctness on a process level but may also be simply due to the forcing.

This thesis provides insight to insight into the physical processes driving Sc. Its results call for horizontal resolution on the order of a few meters in LES if process-level research is conducted. Especially the study on effects of surface heterogeneity motivates future investigation of different surface patterns but also identifies the specific reason producing the observed streamwise "smudging", and the surface heterogeneity signals at the lower cloud boundary. Investigating other surface patterns might inject Sc parameterizations in climate models due to their dependence on surface heterogeneity. In turn, this will improve the representation of Arctic Sc in such models, which supports more exact prognoses of AA, especially due to a better representation of the lapse-rate feedback mechanism.

Acknowledgements

Throughout work on this thesis, I received a great deal of support and input through many valuable and informative discussions.

I first like to thank my supervisor, Prof. Dr. Yaping Shao, for giving me the opportunity to make this thesis happen. His expertise was invaluable during discussions of the research questions and methodology, and his feedback pushed me to reevaluate my applied methods and achieved results.

I offer my special thanks to Dr. Cedrick Ansorge for his assistance at every stage of this research project. His supervision of my day-to-day work and many valuable and informative discussions on the results and occurring problems sharpened my analysis and brought my work to a higher level.

I further thank the Alfred Wegener Institute (AWI), the PS106/1 crew, and the ACLOUD science teams for making the field campaigns and this project happen. I especially thank Ulrich Löhnert for supporting my thesis by many valuable and informative discussions during meetings of the doctoral committee, Christof Lüpkes for providing and discussing noseboom data from Polar 6, Regis Dupuy and Stephan Mertes for providing information on aerosols, and Johannes Stapf for providing information on the surface properties.

I also gratefully acknowledge the funding by the Deutsche Forschungsgemeinschaft (DFG, German Research Foundation)—project ID 268020496–TRR 172—within the Transregional Collaborative Research Center "ArctiC Amplification: Climate Relevant Atmospheric and SurfaCe Processes, and Feedback Mechanisms (AC)^3".

Last but not least, I gratefully acknowledge the Gauss Centre for Supercomputing e.V. (www.gauss-centre.eu) for funding this project by providing computing time through the John von Neumann Institute for Computing (NIC) project HKU24 on the GCS Supercomputers JUQUEEN and JUWELS at Jülich Supercomputing Center (JSC).

Bibliography

Adem, J., 1965: Experiments Aiming at Monthly and Seasonal Numerical Weather Prediction. *Monthly Weather Review*, **93 (8)**, 495–503, doi:10.1175/1520-0493(1965)093<0495:EAAMAS>2.3.CO;2.

Albrecht, B. A., D. A. Randall, and S. Nicholls, 1988: Observations of Marine Stratocumulus Clouds During FIRE. *Bulletin of the American Meteorological Society*, **69 (6)**, 618–626, doi:10.1175/1520-0477(1988)069<0618:OOMSCD>2.0.CO;2.

Arakawa, A., and V. R. Lamb, 1977: Computational Design of the Basic Dynamical Processes of the UCLA General Circulation Model. *Methods in Computational Physics: Advances in Research and Applications*, **17**, 173–265, doi:10.1016/B978-0-12-460817-7.50009-4.

Arrhenius, S., 1897: On the Influence of Carbonic Acid in the Air upon the Temperature of the Earth. *Publications of the Astronomical Society of the Pacific*, **9 (54)**, 14–24, doi:10.1086/121158.

Beare, R. J., and Coauthors, 2006: An Intercomparison of Large-Eddy Simulations of the Stable Boundary Layer. *Boundary-Layer Meteorology*, **118 (2)**, 247–272, doi:10.1007/s10546-004-2820-6.

Beljaars, A. C. M., 1995: The parametrization of surface fluxes in large-scale models under free convection. *Quarterly Journal of the Royal Meteorological Society*, **121 (522)**, 255–270, doi:10.1002/qj.49712152203.

Boussinesq, J., 1877: *Essai sur la théorie des eaux courantes*. Imprimerie Nationale.

Bretherton, C. S., and Coauthors, 1999: An intercomparison of radiatively driven entrainment and turbulence in a smoke cloud, as simulated by different numerical models. *Quarterly Journal of the Royal Meteorological Society*, **125 (554)**, 391–423, doi:10.1002/qj.49712555402.

Ceppi, P., F. Brient, M. D. Zelinka, and D. L. Hartmann, 2017: Cloud feedback mechanisms and their representation in global climate models. *Wiley Interdisciplinary Reviews: Climate Change*, **8 (4)**, e465, doi:10.1002/wcc.465.

Cheng, Y., and W. Brutsaert, 2005: Flux-profile Relationships for Wind Speed and Temperature in the Stable Atmospheric Boundary Layer. *Boundary-Layer Meteorology*, **114 (3)**, 519–538, doi:10.1007/s10546-004-1425-4.

Clough, S. A., M. W. Shephard, E. J. Mlawer, J. S. Delamere, M. J. Iacono, K. Cady-Pereira, S. Boukabara, and P. D. Brown, 2005: Atmospheric radiative transfer modeling: a summary of the AER codes. *Journal of Quantitative Spectroscopy and Radiative Transfer*, **91 (2)**, 233–244, doi:10.1016/j.jqsrt.2004.05.058.

Cohen, J., and Coauthors, 2014: Recent Arctic amplification and extreme mid-latitude weather. *Nature Geoscience*, **7 (9)**, 627–637, doi:10.1038/ngeo2234.

Cohen, J., and Coauthors, 2020: Divergent consensuses on Arctic amplification influence on midlatitude severe winter weather. *Nature Climate Change*, **10 (1)**, 20–29, doi:10.1038/s41558-019-0662-y.

Cottet, G.-H., D. Jiroveanu, and B. Michaux, 2003: Vorticity dynamics and turbulence models for Large-Eddy Simulations. *ESAIM: Mathematical Modelling and Numerical Analysis*, **37 (1)**, 187–207, doi:10.1051/m2an:2003013.

Courant, R., K. Friedrichs, and H. Lewy, 1967: On the Partial Difference Equations of Mathematical Physics. *IBM Journal of Research and Development*, **11 (2)**, 215–234, doi:10.1147/rd.112.0215.

de Lozar, A., and J. P. Mellado, 2017: Reduction of the Entrainment Velocity by Cloud Droplet Sedimentation in Stratocumulus. *Monthly Weather Review*, **74 (3)**, 751–765, doi:10.1175/JAS-D-16-0196.1.

Dirksen, R. J., M. Sommer, F. J. Immler, D. F. Hurst, R. Kivi, and H. Vömel, 2014: Reference quality upper-air measurements: GRUAN data processing for the Vaisala RS92 radiosonde. *Atmospheric Measurement Techniques*, **7 (12)**, 4463–4490, doi:10.5194/amt-7-4463-2014.

Eastman, R., and S. G. Warren, 2010: Interannual Variations of Arctic Cloud Types in Relation to Sea Ice. *Journal of Climate*, **23 (15)**, 4216–4232, doi:10.1175/2010JCLI3492.1.

Egerer, U., M. Gottschalk, H. Siebert, A. Ehrlich, and M. Wendisch, 2019: The new BELUGA setup for collocated turbulence and radiation measurements using a tethered balloon: first applications in the cloudy Arctic boundary layer. *Atmospheric Measurement Techniques*, **12 (7)**, 4019–4038, doi:10.5194/amt-12-4019-2019.

Ehrlich, A., M. Wendisch, C. Lüpkes, S. Crewell, and M. Mech, 2018a: Links to master tracks in different resolutions from POLAR 5 flight ACLOUD_2017_1706051301 (ACLOUD flight reference number 13). PANGAEA, doi:10.1594/PANGAEA.888161.

Ehrlich, A., M. Wendisch, C. Lüpkes, S. Crewell, and M. Mech, 2018b: Links to master tracks in different resolutions from POLAR 6 flight ACLOUD_2017_1706051201 (ACLOUD flight reference number 13). PANGAEA, doi:10.1594/PANGAEA.888350.

Ehrlich, A., and Coauthors, 2019: A comprehensive in situ and remote sensing data set from the Arctic CLoud Observations Using airborne measurements during polar Day (ACLOUD) campaign. *Earth System Science Data Discussions*, **2019 (1)**, 1–42, doi:10.5194/essd-2019-96.

Esau, I. N., 2007: Amplification of turbulent exchange over wide Arctic leads: Large-eddy simulation study. *Journal of Geophysical Research: Atmospheres*, **112 (D8)**, doi:10.1029/2006JD007225.

European Centre for Medium-Range Weather Forecasts, 2017: Era5 reanalysis. Research Data Archive at the National Center for Atmospheric Research, Computational and Information Systems Laboratory, Boulder CO, doi:10.5065/D6X34W69.

Fairall, C. W., E. F. Bradley, D. P. Rogers, J. B. Edson, and G. S. Young, 1996: Bulk parameterization of air-sea fluxes for Tropical Ocean-Global Atmosphere Coupled-Ocean Atmosphere Response Experiment. *Journal of Geophysical Research: Oceans*, **101 (C2)**, 3747–3764, doi:10.1029/95JC03205.

Garcia, J. R., and J. P. Mellado, 2014: The Two-Layer Structure of the Entrainment Zone in the Convective Boundary Layer. *Journal of the Atmospheric Sciences*, **71 (6)**, 1935–1955, doi:10.1175/JAS-D-13-0148.1.

Glendening, J. W., 1994: Dependence of a Plume Heat Budget upon Lateral Advection. *Journal of the Atmospheric Sciences*, **51 (23)**, 3517–3530, doi:10.1175/1520-0469(1994)051<3517:DOAPHB>2.0.CO;2.

Glendening, J. W., and S. D. Burk, 1992: Turbulent transport from an arctic lead: A large-eddy simulation. *Boundary-Layer Meteorology*, **59 (4)**, 315–339, doi:10.1007/BF02215457.

Goody, R., R. West, L. Chen, and D. Crisp, 1989: The correlated-k method for radiation calculations in nonhomogeneous atmospheres. *Journal of Quantitative Spectroscopy and Radiative Transfer*, **42 (6)**, 539–550, doi:10.1016/0022-4073(89)90044-7.

Goody, R. M., and Y. L. Yung, 1989: *Atmospheric radiation: Theoretical basis*. Oxford University Press.

Goosse, H., and Coauthors, 2018: Quantifying climate feedbacks in polar regions. *Nature Communications*, **9 (1)**, 1919, doi:10.1038/s41467-018-04173-0.

Gregory, J. M., and J. Oerlemans, 1998: Simulated future sea-level rise due to glacier melt based on regionally and seasonally resolved temperature changes. *Nature*, **391 (54)**, 474–476, doi:10.1038/35119.

Gryschka, M., C. Drüe, D. Etling, and S. Raasch, 1967: On the influence of sea-ice inhomogeneities onto roll convection in cold-air outbreaks. *Geophysical Research Letters*, **35 (23)**, L23 804, doi:10.1029/2008GL035845.

Gultepe, I., G. A. Isaac, A. Williams, D. Marcotte, and K. B. Strawbridge, 2003: Turbulent heat fluxes over leads and polynyas, and their effects on arctic clouds during FIRE.ACE: Aircraft observations for April 1998. *Atmosphere-Ocean*, **41 (1)**, 15–34, doi:10.3137/ao.410102.

Harrington, J. Y., T. Reisin, W. R. Cotton, and S. M. Kreidenweis, 1999: Cloud resolving simulations of Arctic stratus: Part II: Transition-season clouds. *Atmospheric Research*, **51 (1)**, 45–75, doi:10.1016/S0169-8095(98)00098-2.

Hartmann, J., C. Lüpkes, and D. Chechin, 2019: High resolution aircraft measurements of wind and temperature during the ACLOUD campaign in 2017. PANGAEA, doi:10.1594/PANGAEA.900880.

Heinze, R., D. Mironov, and S. Raasch, 2015: Second-moment budgets in cloud topped boundary layers: A large-eddy simulation study. *Journal of Advances in Modeling Earth Systems*, **7 (2)**, 510–536, doi:10.1002/2014MS000376.

Heinze, R., and Coauthors, 2017: Large-eddy simulations over Germany using ICON: a comprehensive evaluation. *Quarterly Journal of the Royal Meteorological Society*, **143 (702)**, 69–100, doi:10.1002/qj.2947.

Hines, K. M., and D. H. Bromwich, 2017: Simulation of Late Summer Arctic Clouds during ASCOS with Polar WRF. *Monthly Weather Review*, **145 (2)**, 521–541, doi:10.1175/MWR-D-16-0079.1.

Hodson, D. L. R., S. P. E. Keeley, A. West, J. Ridley, E. Hawkins, and H. T. Hewitt, 2013: Identifying uncertainties in Arctic climate change projections. *Climate Dynamics*, **40 (11)**, 2849–2865, doi:10.1007/s00382-012-1512-z.

Iacono, M. J., J. S. Delamere, E. J. Mlawer, M. W. Shephard, S. A. Clough, and W. D. Collins, 2008: Radiative forcing by long-lived greenhouse gases: Calculations with the AER radiative transfer models. *Journal of Geophysical Research: Atmospheres*, **113 (D13)**, D13 103, doi:10.1029/2008JD009944.

Illingworth, A. J., and Coauthors, 2007: Cloudnet. *Bulletin of the American Meteorological Society*, **88 (6)**, 883–898, doi:10.1175/BAMS-88-6-883.

Jiang, H., W. R. Cotton, J. O. Pinto, J. A. Curry, and M. J. Weissbluth, 2000: Cloud Resolving Simulations of Mixed-Phase Arctic Stratus Observed during BASE: Sensitivity to Concentration of Ice Crystals and Large-Scale Heat and Moisture Advection. *Journal of the Atmospheric Sciences*, **57 (13)**, 2105–2117, doi:10.1175/1520-0469(2000)057<2105:CRSOMP>2.0.CO;2.

Jiménez, P. A., J. Dudhia, J. F. González-Rouco, J. Navarro, J. P. Montávez, and E. García-Bustamante, 2012: A Revised Scheme for the WRF Surface Layer Formulation. *Monthly Weather Review*, **140 (3)**, 898–918, doi:10.1175/MWR-D-11-00056.1.

Jung, T., and Coauthors, 2016: Advancing Polar Prediction Capabilities on Daily to Seasonal Time Scales. *Bulletin of the American Meteorological Society*, **97 (9)**, 1631–1647, doi:10.1175/BAMS-D-14-00246.1.

Kaul, C. M., J. Teixeira, and K. Suzuki, 2015: Sensitivities in Large-Eddy Simulations of Mixed-Phase Arctic Stratocumulus Clouds Using a Simple Microphysics Approach. *Monthly Weather Review*, **143 (11)**, 4393–4421, doi:10.1175/MWR-D-14-00319.1.

Kay, J. E., and A. Gettelman, 2009: Cloud influence on and response to seasonal Arctic sea ice loss. *Journal of Geophysical Research: Atmospheres*, **114 (D18)**, doi:10.1029/2009JD011773.

Kay, J. E., T. L'Ecuyer, H. Chepfer, N. Loeb, A. Morrison, and G. Cesana, 2016: Recent Advances in Arctic Cloud and Climate Research. *Current Climate Change Reports*, **2 (4)**, 159–169, doi:10.1007/s40641-016-0051-9.

Klein, S. A., and Coauthors, 2009: Intercomparison of model simulations of mixed-phase clouds observed during the ARM Mixed-Phase Arctic Cloud Experiment. I:

single-layer cloud. *Quarterly Journal of the Royal Meteorological Society*, **135 (641)**, 979–1002, doi:10.1002/qj.416.

Knudsen, E. M., and Coauthors, 2018: Meteorological conditions during the ACLOUD/-PASCAL field campaign near Svalbard in early summer 2017. *Atmospheric Chemistry and Physics*, **18 (24)**, 17 885–8022, doi:10.5194/acp-18-17995-2018.

Kolmogorov, A. N., V. Levin, J. C. R. Hunt, O. M. Phillips, and D. Williams, 1941: The local structure of turbulence in incompressible viscous fluid for very large Reynolds numbers. *Doklady Akademii Nauk SSSR*, **30**, 299–303.

Kolmogorov, A. N., V. Levin, J. C. R. Hunt, O. M. Phillips, and D. Williams, 1991: The local structure of turbulence in incompressible viscous fluid for very large Reynolds numbers. *Proceedings of the Royal Society of London. Series A: Mathematical and Physical Sciences*, **434 (1890)**, 9–13, doi:10.1098/rspa.1991.0075.

Lee, S.-W., and J.-M. Song, 2014: Economic Possibilities of Shipping though Northern Sea Route. *The Asian Journal of Shipping and Logistics*, **30 (3)**, 415–430, doi:10.1016/j.ajsl.2014.12.009.

Leonard, A., 1975: Energy Cascade in Large-Eddy Simulations of Turbulent Fluid Flows. *Turbulent Diffusion in Environmental Pollution*, Advances in Geophysics, Vol. 18, Elsevier, 237–248, doi:10.1016/S0065-2687(08)60464-1.

Lewellen, D. C., and W. S. Lewellen, 1998: Large-Eddy Boundary Layer Entrainment. *Journal of the Atmospheric Sciences*, **55 (16)**, 2645–2668, doi:10.1175/1520-0469(1998)055<2645:LEBLE>2.0.CO;2.

Lilly, D. K., 1962: On the numerical simulation of buoyant convection. *Tellus*, **14 (2)**, 148–172, doi:10.1111/j.2153-3490.1962.tb00128.x.

Liu, S., Y. Shao, A. Kunoth, and C. Simmer, 2017: Impact of surface-heterogeneity on atmosphere and land-surface interactions. *Environmental Modelling & Software*, **88**, 35–47, doi:10.1016/j.envsoft.2016.11.006.

Lüpkes, C., V. M. Gryanik, B. Witha, M. Gryschka, S. Raasch, and T. Gollnik, 2008a: Modeling convection over arctic leads with LES and a non-eddy-resolving microscale model. *Journal of Geophysical Research: Oceans*, **113 (C9)**, doi:10.1029/2007JC004099.

Lüpkes, C., T. Vihma, G. Birnbaum, and U. Wacker, 2008b: Influence of leads in sea ice on the temperature of the atmospheric boundary layer during polar night. *Geophysical Research Letters*, **35 (3)**, L03 805, doi:10.1029/2007GL032461.

Mahrt, L. T., and J. Sun, 1995: The Subgrid Velocity Scale in the Bulk Aerodynamic Relationship for Spatially Averaged Scalar Fluxes. *Monthly Weather Review*, **123 (10)**, 3032–3041, doi:10.1175/1520-0493(1995)123<3032:TSVSIT>2.0.CO;2.

Manabe, S., and R. J. Stouffer, 1980: Sensitivity of a global climate model to an increase of CO2 concentration in the atmosphere. *Journal of Geophysical Research: Oceans*, **85 (C10)**, 5529–5554, doi:10.1029/JC085iC10p05529.

Manabe, S., and R. T. Wetherald, 1967: Thermal Equilibrium of the Atmosphere with a Given Distribution of Relative Humidity. *Journal of the Atmospheric Sciences*, **24 (3)**, 241–259, doi:10.1175/1520-0469(1967)024<0241:TEOTAW>2.0.CO;2.

Manabe, S., and R. T. Wetherald, 1975: The Effects of Doubling the CO2 Concentration on the climate of a General Circulation Model. *Journal of the Atmospheric Sciences*, **32 (1)**, 3–15, doi:10.1175/1520-0469(1975)032<0003:TEODTC>2.0.CO;2.

Maronga, B., and S. Raasch, 2013: Large-Eddy Simulations of Surface Heterogeneity Effects on the Convective Boundary Layer During the LITFASS-2003 Experiment. *Boundary-Layer Meteorology*, **146 (1)**, 17–44, doi:10.1007/s10546-012-9748-z.

Matheou, G., 2018: Turbulence Structure in a Stratocumulus Cloud. *Atmosphere*, **9 (10)**, 392, doi:10.3390/atmos9100392.

Matheou, G., and D. Chung, 2014: Large-Eddy Simulation of Stratified Turbulence. Part II: Application of the Stretched-Vortex Model to the Atmospheric Boundary Layer. *Journal of the Atmospheric Sciences*, **71 (12)**, 4439–4460, doi:10.1175/JAS-D-13-0306.1.

Mellado, J. P., 2017: Cloud-Top Entrainment in Stratocumulus Clouds. *Annual Review of Fluid Mechanics*, **49 (1)**, 145–169, doi:10.1146/annurev-fluid-010816-060231.

Mellado, J. P., C. S. Bretherton, B. Stevens, and M. C. Wyant, 2018: DNS and LES for Simulating Stratocumulus: Better Together. *Journal of Advances in Modeling Earth Systems*, **10 (7)**, 1421–1438, doi:10.1029/2018MS001312.

Mellado, J. P., M. Puche, and C. C. van Heerwaarden, 2017: Moisture statistics in free convective boundary layers growing into linearly stratified atmospheres. *Quarterly Journal of the Royal Meteorological Society*, **143 (707)**, 2403–2419, doi:10.1002/qj.3095.

Mellado, J. P., B. Stevens, H. Schmidt, and N. Peters, 2009: Buoyancy reversal in cloud-top mixing layers. *Quarterly Journal of the Royal Meteorological Society*, **135 (641)**, 963–978, doi:10.1002/qj.417.

Michaelis, J., C. Lüpkes, X. Zhou, M. Gryschka, and V. M. Gryanik, 2020: Influence of Lead width on the Turbulent Flow Over Sea Ice Leads: Modeling and Parametrization. *Journal of Geophysical Research: Atmospheres*, **125 (15)**, doi:10.1029/2019JD031996.

Mironov, D. V., and P. P. Sullivan, 2015: Second-Moment Budgets and Mixing Intensity in the Stably Stratified Atmospheric Boundary Layer over Thermally Heterogeneous Surfaces. *Journal of the Atmospheric Sciences*, **73 (1)**, 449–464, doi:10.1175/JAS-D-15-0075.1.

Mlawer, E. J., S. J. Taubman, P. D. Brown, M. J. Iacono, and S. A. Clough, 1997: Radiative transfer for inhomogeneous atmospheres: RRTM, a validated correlated-k model for the longwave. *Journal of Geophysical Research: Atmospheres*, **102 (D14)**, 16 663–16 682, doi:10.1029/97JD00237.

Moin, P., 2009: Revisiting Taylor's hypothesis. *Journal of Fluid Mechanics*, **640 (1)**, 1–4, doi:10.1017/S0022112009992126.

Morrison, A. L., J. E. Kay, H. Chepfer, R. Guzman, and V. Yettella, 2018: Isolating the Liquid Cloud Response to Recent Arctic Sea Ice Variability Using Spaceborne Lidar Observations. *Journal of Geophysical Research: Atmospheres*, **123 (1)**, 473–490, doi:10.1002/2017JD027248.

Morrison, H., J. A. Curry, and V. I. Khvorostyanov, 2005: A New Double-Moment Microphysics Parameterization for Application in Cloud and Climate Models. Part I: Description. *Journal of the Atmospheric Sciences*, **62 (6)**, 1665–1677, doi:10.1175/JAS3446.1.

Morrison, H., and J. O. Pinto, 2006: Intercomparison of Bulk Cloud Microphysics Schemes in Mesoscale Simulations of Springtime Arctic Mixed-Phase Stratiform Clouds. *Monthly Weather Review*, **134 (7)**, 1880–1900, doi:10.1175/MWR3154.1.

Morrison, H., J. O. Pinto, J. A. Curry, and G. M. McFarquhar, 2008: Sensitivity of modeled arctic mixed-phase stratocumulus to cloud condensation and ice nuclei over regionally varying surface conditions. *Journal of Geophysical Research: Atmospheres*, **113 (D5)**, D05 203, doi:10.1029/2007JD008729.

Morrison, H., G. Thompson, and V. Tatarskii, 2009: Impact of Cloud Microphysics on the Development of Trailing Stratiform Precipitation in a Simulated Squall Line: Comparison of One- and Two-Moment Schemes. *Monthly Weather Review*, **137 (3)**, 991–1007, doi:10.1175/2008MWR2556.1.

Morrison, H., and Coauthors, 2020: Confronting the Challenge of Modeling Cloud and Precipitation Microphysics. *Journal of Advances in Modeling Earth Systems*, **12 (8)**, e2019MS001 689, doi:10.1029/2019MS001689.

Naakka, T., T. Nygård, and T. Vihma, 2018: Arctic Humidity Inversions: Climatology and Processes. *Journal of Climate*, **31 (10)**, 3765–3787, doi:10.1175/JCLI-D-17-0497.1.

Neggers, R. A. J., J. Chylik, U. Egerer, H. Griesche, V. Schemann, P. Seifert, H. Siebert, and A. Macke, 2019: Local and remote controls on Arctic mixed-layer evolution. *Journal of Advances in Modeling Earth Systems*, **11 (7)**, 2214–2237, doi:10.1029/2019MS001671.

Neggers, R. A. J., T. Heus, and A. P. Siebesma, 2011: Overlap statistics of cumuliform boundary-layer cloud fields in large-eddy simulations. *Journal of Geophysical Research: Atmospheres*, **116 (1)**, D21, doi:10.1029/2011JD015650.

Oreopoulos, L., and H. W. Barker, 1999: Accounting for subgrid-scale cloud variability in a multi-layer 1d solar radiative transfer algorithm. *Quarterly Journal of the Royal Meteorological Society*, **125 (553)**, 301–330, doi:10.1002/qj.49712555316.

Ovchinnikov, M., and Coauthors, 2014: Intercomparison of large-eddy simulations of Arctic mixed-phase clouds: Importance of ice size distribution assumptions. *Journal of Advances in Modeling Earth Systems*, **6 (1)**, 223–248, doi:10.1002/2013MS000282.

Park, S.-H., W. C. Skamarock, J. B. Klemp, L. D. Fowler, and M. G. Duda, 2013: Evaluation of Global Atmospheric Solvers Using Extensions of the Jablonowski and Williamson Baroclinic Wave Test Case. *Monthly Weather Review*, **141 (9)**, 3116–3129, doi:10.1175/MWR-D-12-00096.1.

Paulson, C. A., 1970: The Mathematical Representation of Wind Speed and Temperature Profiles in the Unstable Atmospheric Surface Layer. *Journal of Applied Meteorology*, **9 (6)**, 857–861, doi:10.1175/1520-0450(1970)009<0857:TMROWS>2.0.CO;2.

Pawlak, D. T., E. E. Clothiaux, M. F. Modest, and J. N. S. Cole, 2004: Full-Spectrum Correlated-k Distribution for Shortwave Atmospheric Radiative Transfer. *Journal of the Atmospheric Sciences*, **61 (21)**, 2588–2601, doi:10.1175/JAS3285.1.

Pedersen, J. G., S. P. Malinowski, and W. W. Grabowski, 2016: Resolution and domain-size sensitivity in implicit large-eddy simulation of the stratocumulus-topped boundary layer. *Journal of Advances in Modeling Earth Systems*, **8 (2)**, 885–903, doi:10.1002/2015MS000572.

Pincus, R., H. W. Barker, and J.-J. Morcrette, 2003: A fast, flexible, approximate technique for computing radiative transfer in inhomogeneous cloud fields. *Journal of Geophysical Research: Atmospheres*, **108 (D13)**, AAC, doi:10.1029/2002JD003322.

Pithan, F., and T. Mauritsen, 2013: Comments on "Current GCMs' Unrealistic Negative Feedback in the Arctic". *Journal of Climate*, **26 (19)**, 7783–7788, doi:10.1175/JCLI-D-12-00331.1.

Pithan, F., and T. Mauritsen, 2014: Arctic amplification dominated by temperature feedbacks in contemporary climate models. *Nature Geoscience*, **7 (3)**, 181–184, doi:10.1038/ngeo2071.

Pithan, F., B. Medeiros, and T. Mauritsen, 2014: Mixed-phase clouds cause climate model biases in Arctic wintertime temperature inversions. *Climate Dynamics*, **43 (1)**, 289–303, doi:10.1007/s00382-013-1964-9.

Pope, S. B., 2000: *Turbulent Flows*. Cambridge University Press, doi:10.1017/CBO9780511840531.

Possner, A., A. M. L. Ekman, and U. Lohmann, 2017: Cloud response and feedback processes in stratiform mixed-phase clouds perturbed by ship exhaust. *Geophysical Research Letters*, **44 (4)**, 1964–1972, doi:10.1002/2016GL071358.

Prabha, T. V., A. Karipot, and M. W. Binford, 2007: Characteristics of secondary circulations over an inhomogeneous surface simulated with large-eddy simulation. *Boundary-Layer Meteorology*, **123 (2)**, 239–261, doi:10.1007/s10546-006-9137-6.

Pressel, K. G., S. Mishra, T. Schneider, C. M. Kaul, and Z. Tan, 2017: Numerics and subgrid-scale modeling in large eddy simulations of stratocumulus clouds. *Journal of Advances in Modeling Earth Systems*, **9 (2)**, 1342–1365, doi:10.1002/2016MS000778.

Raasch, S., and G. Harbusch, 2001: An Analysis Of Secondary Circulations And Their Effects Caused By Small-Scale Surface Inhomogeneities Using Large-Eddy Simulation. *Boundary-Layer Meteorology*, **101 (1)**, 31–59, doi:10.1023/A:1019297504109.

Rauterkus, R., and C. Ansorge, 2019: LES of Arctic mixed-phase Stratocumulus (ACLOUD RF13). PANGAEA, doi:10.1594/PANGAEA.904399.

Rauterkus, R., and C. Ansorge, 2020: Cloud-Top Entrainment in Mixed-Phase Stratocumulus and its Process-Level Representation in Large-Eddy Simulation. *Journal of the Atmospheric Sciences*, **77 (12)**, 4109–4127, doi:10.1175/JAS-D-19-0221.1.

Regehr, E. V., N. J. Lunn, S. C. Amstrup, and I. Stirling, 2007: Effects of Earlier Sea Ice Breakup on Survival and Population Size of Polar Bears in Western Hudson Bay. *Journal of Wildlife Management*, **71 (8)**, 2673–2683, doi:10.2193/2006-180.

Rogers, T. S., J. E. Walsh, T. S. Rupp, L. W. Brigham, and M. Sfraga, 2013: Future Arctic marine access: analysis and evaluation of observations, models, and projections of sea ice. *The Cryosphere*, **7 (1)**, 321–332, doi:10.5194/tc-7-321-2013.

Sagaut, P., 2006: *Large Eddy Simulation for Incompressible Flows*. Springer-Verlag Berlin Heidelberg, doi:10.1007/b137536.

Schemann, V., and K. Ebell, 2020: Simulation of mixed-phase clouds with the ICON large-eddy model in the complex Arctic environment around Ny-Ålesund. *Atmospheric Chemistry and Physics*, **20 (1)**, 475–485, doi:10.5194/acp-20-475-2020.

Schmithüsen, H., 2017a: Radiosonde PS106_39890 during POLARSTERN cruise PS106.1 (ARK-XXXI/1.1) on 2017-06-05 10:53h. PANGAEA, doi:10.1594/PANGAEA.882679.

Schmithüsen, H., 2017b: Radiosonde PS106_39891 during POLARSTERN cruise PS106.1 (ARK-XXXI/1.1) on 2017-06-05 16:50h. PANGAEA, doi:10.1594/PANGAEA.882680.

Schmitt, F. G., 2007: About Boussinesq's turbulent viscosity hypothesis: historical remarks and a direct evaluation of its validity. *Comptes Rendus Mécanique*, **335 (9)**, 617–627, doi:10.1016/j.crme.2007.08.004.

Schneider, T., J. Teixeira, C. S. Bretherton, F. Brient, K. G. Pressel, C. Schär, and A. P. Siebesma, 2017: Climate goals and computing the future of clouds. *Nature Climate Change*, **7 (1)**, 3–5, doi:10.1038/nclimate3190.

Schulz, B., and J. P. Mellado, 2018: Wind Shear Effects on Radiatively and Evaporatively Driven Stratocumulus Tops. *Journal of the Atmospheric Sciences*, **75 (9)**, 3245–3263, doi:10.1175/JAS-D-18-0027.1.

Shupe, M. D., and J. M. Intrieri, 2004: Cloud Radiative Forcing of the Arctic Surface: The Influence of Cloud Properties, Surface Albedo, and Solar Zenith Angle. *Journal of Climate*, **17 (3)**, 616–628, doi:10.1175/1520-0442(2004)017<0616:CRFOTA>2.0.CO;2.

Skamarock, W. C., 2004: Evaluating Mesoscale NWP Models Using Kinetic Energy Spectra. *Monthly Weather Review*, **132 (12)**, 3019–3032, doi:10.1175/MWR2830.1.

Skamarock, W. C., and Coauthors, 2008: A Description of the Advanced Research WRF Model Version 3. Tech. rep., National Center for Atmospheric Research, Boulder CO. doi:10.5065/D68S4MVH.

Skamarock, W. C., and Coauthors, 2019: A Description of the Advanced Research WRF Model Version 4. Tech. rep., National Center for Atmospheric Research, Boulder CO. doi:10.5065/1dfh-6p97.

Smagorinsky, J., 1963: GENERAL CIRCULATION EXPERIMENTS WITH THE PRIMITIVE EQUATIONS. *Monthly Weather Review*, **91 (3)**, 99–164, doi:10.1175/1520-0493(1963)091<0099:GCEWTP>2.3.CO;2.

Solomon, A., G. de Boer, J. M. Creamean, A. McComiskey, M. D. Shupe, M. Maahn, and C. Cox, 2018: The relative impact of cloud condensation nuclei and ice nucleating particle concentrations on phase partitioning in Arctic mixed-phase stratocumulus clouds. *Atmospheric Chemistry and Physics*, **18 (23)**, 17 047–17 059, doi:10.5194/acp-18-17047-2018.

Solomon, A., M. D. Shupe, O. Persson, H. Morrison, T. Yamaguchi, P. M. Caldwell, and G. de Boer, 2014: The Sensitivity of Springtime Arctic Mixed-Phase Stratocumulus Clouds to Surface-Layer and Cloud-Top Inversion-Layer Moisture Sources. *Journal of the Atmospheric Sciences*, **71 (2)**, 574–595, doi:10.1175/JAS-D-13-0179.1.

Sorooshian, A., and Coauthors, 2018: A multi-year data set on aerosol-cloud-precipitation-meteorology interactions for marine stratocumulus clouds. *Scientific Data*, **5 (1)**, 180 026, doi:10.1038/sdata.2018.26.

Stapf, J., A. Ehrlich, E. Jäkel, and M. Wendisch, 2019: Aircraft measurements of broadband irradiance during the ACLOUD campaign in 2017. PANGAEA, doi:10.1594/PANGAEA.900442.

Stensrud, D. J., 2007: *Parameterization Schemes: Keys to Understanding Numerical Weather Prediction Models*. Cambridge University Press, doi:10.1007/978-94-009-3027-8.

Stern, H. L., and K. L. Laidre, 2016: Sea-ice indicators of polar bear habitat. *The Cryosphere*, **10 (5)**, 2027–2041, doi:10.5194/tc-10-2027-2016.

Stevens, B., and Coauthors, 2001: Simulations of Trade Wind Cumuli under a Strong Inversion. *Journal of the Atmospheric Sciences*, **58 (14)**, 1870–1891, doi:10.1175/1520-0469(2001)058<1870:SOTWCU>2.0.CO;2.

Stevens, B., and Coauthors, 2003a: Dynamics and Chemistry of Marine Stratocumulus–DYCOMS-II. *Bulletin of the American Meteorological Society*, **84 (5)**, 579–594, doi:10.1175/BAMS-84-5-579.

Stevens, B., and Coauthors, 2003b: Dynamics and Chemistry of Marine Stratocumulus–DYCOMS-II. *Bulletin of the American Meteorological Society*, **84 (5)**, S12–S25, doi:10.1175/BAMS-84-5-Stevens.

Stevens, B., and Coauthors, 2003c: On entrainment rates in nocturnal marine stratocumulus. *Quarterly Journal of the Royal Meteorological Society*, **129 (595)**, 3469–3493, doi:10.1256/qj.02.202.

Stevens, B., and Coauthors, 2005: Evaluation of Large-Eddy Simulations via Observations of Nocturnal Marine Stratocumulus. *Monthly Weather Review*, **133 (6)**, 1443–1462, doi:10.1175/MWR2930.1.

Stevens, D. E., and C. S. Bretherton, 1999: Effects of resolution on the simulation of stratocumulus entrainment. *Quarterly Journal of the Royal Meteorological Society*, **125 (554)**, 425–439, doi:10.1002/qj.49712555403.

Stoll, R., and F. Porté-Agel, 2009: Surface Heterogeneity Effects on Regional-Scale Fluxes in Stable Boundary Layers: Surface Temperature Transitions. *Journal of the Atmospheric Sciences*, **66 (2)**, 412–431, doi:10.1175/2008JAS2668.1.

Stull, R. B., 1988: *An Introduction to Boundary Layer Meteorology*. Springer Netherlands, doi:10.1007/978-94-009-3027-8.

Taylor, G. I., 1938: The Spectrum of Turbulence. *Proceedings of the Royal Society of London. Series A - Mathematical and Physical Sciences*, **164 (919)**, 476–490, doi:10.1098/rspa.1938.0032.

Tjernström, M., J. Sedlar, and M. D. Shupe, 2008: How Well Do Regional Climate Models Reproduce Radiation and Clouds in the Arctic? An Evaluation of ARCMIP Simulations. *Journal of Applied Meteorology and Climatology*, **47 (9)**, 2405–2422, doi:10.1175/2008JAMC1845.1.

Tjernström, M., and Coauthors, 2014: The Arctic Summer Cloud Ocean Study (ASCOS): overview and experimental design. *Monthly Weather Review*, **14 (6)**, 2823–2869, doi:10.5194/acp-14-2823-2014.

Tyndall, J., 1861: The Bakerian Lecture: On the Absorption and Radiation of Heat by Gases and Vapours, and onthe Physical Connexion of Radiation, Absorption, and Conduction. *Philosophical Transactions of the Royal Society of London*, **151 (1)**, 1–36, doi:10.1098/rstl.1861.0001.

Vavrus, S., 2004: The Impact of Cloud Feedbacks on Arctic Climate under Greenhouse Forcing. *Journal of Climate*, **17 (3)**, 603–615, doi:10.1175/1520-0442(2004)017<0603:TIOCFO>2.0.CO;2.

Verlinde, J., and Coauthors, 2007: The Mixed-Phase Arctic Cloud Experiment. *Bulletin of the American Meteorological Society*, **88 (2)**, 205–222, doi:10.1175/BAMS-88-2-205.

Wang, J., H.-M. Kim, and E. K. M. Chang, 2017: Changes in Northern Hemisphere Winter Storm Tracks under the Background of Arctic Amplification. *Journal of Climate*, **30 (10)**, 3705–3724, doi:10.1175/JCLI-D-16-0650.1.

Wang, X., and J. R. Key, 2003: Recent Trends in Arctic Surface, Cloud, and Radiation Properties from Space. *Science*, **299 (5613)**, 1725–1728, doi:10.1126/science.1078065.

Weinbrecht, S., and S. Raasch, 2001: High-resolution simulations of the turbulent flow in the vicinity of an Arctic lead. *Journal of Geophysical Research: Oceans*, **106 (C11)**, 27 035–27 046, doi:10.1029/2000JC000781.

Wendisch, M., and Coauthors, 2017: Understanding Causes and Effects of Rapid Warming in the Arctic. *Eos*, **98 (8)**, 22–26, doi:10.1029/2017EO064803.

Wendisch, M., and Coauthors, 2019: The Arctic Cloud Puzzle: Using ACLOUD/PASCAL Multiplatform Observations to Unravel the Role of Clouds and Aerosol Particles in Arctic Amplification. *Bulletin of the American Meteorological Society*, **100 (5)**, 841–871, doi:10.1175/BAMS-D-18-0072.1.

Wenta, M., and A. Herman, 2018: The influence of the spatial distribution of leads and ice floes on the atmospheric boundary layer over fragmented sea ice. *Annals of Glaciology*, **59 (76pt2)**, 213–230, doi:10.1017/aog.2018.15.

Wenta, M., and A. Herman, 2019: Area-Averaged Surface Moisture Flux over Fragmented Sea Ice: Floe Size Distribution Effects and the Associated Convection Structure within the Atmospheric Boundary Layer. *Atmosphere*, **10 (11)**, 654, doi:10.3390/atmos10110654.

Wicker, L. J., and W. C. Skamarock, 2002: Time-Splitting Methods for Elastic Models Using Forward Time Schemes. *Monthly Weather Review*, **130 (8)**, 2088–2097, doi:10.1175/1520-0493(2002)130<2088:TSMFEM>2.0.CO;2.

Wood, R., 2012: Stratocumulus Clouds. *Monthly Weather Review*, **140 (8)**, 2373–2423, doi:10.1175/MWR-D-11-00121.1.

Yamaguchi, T., and G. Feingold, 2012: Technical note: Large-eddy simulation of cloudy boundary layer with the Advanced Research WRF model. *Journal of Advances in Modeling Earth Systems*, **4 (3)**, M09 003, doi:10.1029/2012MS000164.

Young, G., P. J. Connolly, H. M. Jones, and T. W. Choularton, 2017: Microphysical sensitivity of coupled springtime Arctic stratocumulus to modelled primary ice over the ice pack, marginal ice, and ocean. *Atmospheric Chemistry and Physics*, **17 (6)**, 4209–4227, doi:10.5194/acp-17-4209-2017.

Yu, Y., P. C. Taylor, and M. Cai, 2019: Seasonal Variations of Arctic Low-Level Clouds and Its Linkage to Sea Ice Seasonal Variations. *Journal of Geophysical Research: Atmospheres*, **124 (22)**, 12 206–12 226, doi:10.1029/2019JD031014.

Zelinka, M. D., S. A. Klein, and D. L. Hartmann, 2012: Computing and Partitioning Cloud Feedbacks Using Cloud Property Histograms. Part II: Attribution to Changes in Cloud Amount, Altitude, and Optical Depth. *Journal of Climate*, **25 (11)**, 3736–3754, doi:10.1175/JCLI-D-11-00249.1.

Zemp, M., and Coauthors, 2019: Global glacier mass changes and their contributions to sea-level rise from 1961 to 2016. *Nature*, **568 (7752)**, 382–386, doi:10.1038/s41586-019-1071-0.

Zhou, X., P. Kollias, and E. R. Lewis, 2004: Clouds, Precipitation, and Marine Boundary Layer Structure during the MAGIC Field Campaign. *Journal of Climate*, **28 (6)**, 2420–2442, doi:10.1175/JCLI-D-14-00320.1.

Appendix A

Parameterization of Large-Scale Subsidence

```
module module_rora

use module_model_constants, only: g=>g, cp=>cp
implicit none
contains

!=================================================================================
!rora_subsidence_init ============================================================
!=================================================================================
subroutine rora_subsidence_init(mu_ten,th_ten,ph_ten,u_ten,v_ten,w_ten,          &
  qv_ten,qc_ten,qr_ten,qi_ten,qs_ten,qg_ten,qrn_ten,qin_ten,qsn_ten,qgn_ten,     &
  ims,ime,jms,jme,kms,kme,its,ite,jts,jte,kts,kte)
!input variables
  integer,intent(in) :: ims,ime,jms,jme,kms,kme,its,ite,jts,jte,kts,kte
!output variables
  real,dimension(ims:ime,jms:jme),intent(out) :: mu_ten
  real,dimension(ims:ime,kms:kme,jms:jme),intent(out) :: th_ten,ph_ten,          &
    u_ten,v_ten,w_ten,qv_ten,qc_ten,qr_ten,qi_ten,qs_ten,qg_ten,                 &
    qrn_ten,qin_ten,qsn_ten,qgn_ten
!initialization
  mu_ten(its:ite,jts:jte) = 0.0
  th_ten(its:ite,kts:kte,jts:jte) = 0.0
  ph_ten(its:ite,kts:kte,jts:jte) = 0.0
  u_ten(its:ite,kts:kte,jts:jte) = 0.0
  v_ten(its:ite,kts:kte,jts:jte) = 0.0
  w_ten(its:ite,kts:kte,jts:jte) = 0.0
  qv_ten(its:ite,kts:kte,jts:jte) = 0.0
  qc_ten(its:ite,kts:kte,jts:jte) = 0.0
  qr_ten(its:ite,kts:kte,jts:jte) = 0.0
  qi_ten(its:ite,kts:kte,jts:jte) = 0.0
  qs_ten(its:ite,kts:kte,jts:jte) = 0.0
  qg_ten(its:ite,kts:kte,jts:jte) = 0.0
  qrn_ten(its:ite,kts:kte,jts:jte) = 0.0
  qin_ten(its:ite,kts:kte,jts:jte) = 0.0
  qsn_ten(its:ite,kts:kte,jts:jte) = 0.0
  qgn_ten(its:ite,kts:kte,jts:jte) = 0.0
end subroutine rora_subsidence_init
```

```
!##################################################################################
!rora_subsidence ###################################################################
!##################################################################################
subroutine rora_subsidence(thg,div,z,zw,th,ph,u,v,w,                    &
  qv,qc,qr,qi,qs,qg,qrn,qin,qsn,qgn,mu_ten,th_ten,ph_ten,u_ten,v_ten,w_ten,     &
  qv_ten,qc_ten,qr_ten,qi_ten,qs_ten,qg_ten,qrn_ten,qin_ten,qsn_ten,qgn_ten,    &
  ims,ime,jms,jme,kms,kme,its,ite,jts,jte,kts,kte)
!input variables
  integer,intent(in) :: ims,ime,jms,jme,kms,kme,its,ite,jts,jte,kts,kte
  real,intent(in) :: thg,div
  real,dimension(ims:ime,kms:kme,jms:jme),intent(in) :: z,zw,th,ph,u,v,w,       &
    qv,qc,qr,qi,qs,qg,qrn,qin,qsn,qgn
!output variables
  real,dimension(ims:ime,jms:jme),intent(out) :: mu_ten
  real,dimension(ims:ime,kms:kme,jms:jme),intent(out) :: th_ten,ph_ten,         &
    u_ten,v_ten,w_ten,qv_ten,qc_ten,qr_ten,qi_ten,qs_ten,qg_ten,                 &
    qrn_ten,qin_ten,qsn_ten,qgn_ten
!runtime variables
  integer :: i,j,k,m,n,ke,ks,kt,kb
  real :: dz
!initialization
  call rora_subsidence_init(mu_ten,th_ten,ph_ten,u_ten,v_ten,w_ten,             &
    qv_ten,qc_ten,qr_ten,qi_ten,qs_ten,qg_ten,qrn_ten,qin_ten,qsn_ten,qgn_ten, &
    ims,ime,jms,jme,kms,kme,its,ite,jts,jte,kts,kte)
!### no large-scale forcing (w=0) ###############################################
  if (div == 0.0) then
    return
!### large-scale divergence in boundary layer (w<0) #############################
  else if (div > 0.0) then
    ke = kme-1
    ks = kms
    m = 1
    n = 0
!### large-scale convergence in boundary layer (w>0) ############################
  else
    ke = kme
    ks = kms+1
    m = 0
    n = -1
  end if
!##################################################################################
!algorithm
!##################################################################################
  !column tendency of dry air mass is proportional to divergence
  mu_ten = div
  !loop through coordinates for other variables
  do j = jts,jte,1
  do k = ks,ke,1
    kt = k+m                                                                    !
        upper k
    kb = k+n                                                                    !
        lower k
  do i = its,ite,1
    !half level variables
    dz = z(i,kt,j)-z(i,kb,j)
```

```
    th_ten(i,k,j) = div*zw(i,kt,j) * (th(i,kt,j)-th(i,kb,j))/dz
    u_ten(i,k,j) = div*zw(i,kt,j) * (u(i,kt,j)-u(i,kb,j))/dz
    v_ten(i,k,j) = div*zw(i,kt,j) * (v(i,kt,j)-v(i,kb,j))/dz
    qv_ten(i,k,j) = div*zw(i,kt,j) * (qv(i,kt,j)-qv(i,kb,j))/dz
    qc_ten(i,k,j) = div*zw(i,kt,j) * (qc(i,kt,j)-qc(i,kb,j))/dz
    qr_ten(i,k,j) = div*zw(i,kt,j) * (qr(i,kt,j)-qr(i,kb,j))/dz
    qi_ten(i,k,j) = div*zw(i,kt,j) * (qi(i,kt,j)-qi(i,kb,j))/dz
    qs_ten(i,k,j) = div*zw(i,kt,j) * (qs(i,kt,j)-qs(i,kb,j))/dz
    qg_ten(i,k,j) = div*zw(i,kt,j) * (qg(i,kt,j)-qg(i,kb,j))/dz
    qrn_ten(i,k,j) = div*zw(i,kt,j) * (qrn(i,kt,j)-qrn(i,kb,j))/dz
    qin_ten(i,k,j) = div*zw(i,kt,j) * (qin(i,kt,j)-qin(i,kb,j))/dz
    qsn_ten(i,k,j) = div*zw(i,kt,j) * (qsn(i,kt,j)-qsn(i,kb,j))/dz
    qgn_ten(i,k,j) = div*zw(i,kt,j) * (qgn(i,kt,j)-qgn(i,kb,j))/dz
    !full level variables
    dz = zw(i,kt,j)-zw(i,kb,j)
    ph_ten(i,k,j) = -g*div*zw(i,k,j) +                                    &
                     div*z(i,kb,j) * (ph(i,kt,j)-ph(i,kb,j))/dz
    w_ten(i,k,j) = div*z(i,kb,j) * (w(i,kt,j)-w(i,kb,j))/dz +             &
                     w(i,k,j)*div - div*z(i,k,j)*div
  end do
  end do
  end do
!###############################################################################
!boundary condition (only for w<0 because very small w at surface)
!###############################################################################
  if (div > 0.0) then
    do j = jts,jte,1
    do i = its,ite,1
      th_ten(i,ke,j) = div*zw(i,ke+1,j) * thg
      th_ten(i,ke+1,j) = th_ten(i,ke,j)
      u_ten(i,ke,j) = 0.0
      v_ten(i,ke,j) = 0.0
      w_ten(i,ke,j) = 0.0
      qv_ten(i,ke,j) = 0.0
      qc_ten(i,ke,j) = 0.0
      qr_ten(i,ke,j) = 0.0
      qi_ten(i,ke,j) = 0.0
      qs_ten(i,ke,j) = 0.0
      qg_ten(i,ke,j) = 0.0
      qrn_ten(i,ke,j) = 0.0
      qin_ten(i,ke,j) = 0.0
      qsn_ten(i,ke,j) = 0.0
      qgn_ten(i,ke,j) = 0.0
      ph_ten(i,ke,j) = -g*div*zw(i,ke,j) + div*z(i,ke-1,j) * g
      ph_ten(i,ke+1,j) = ph_ten(i,ke,j)
    end do
    end do
  end if
end subroutine rora_subsidence

end module module_rora
```

Appendix B

Pattern Creation Algorithm

The surface pattern creation algorithm starts with a two-dimensional Gaussian function G in wavenumber space

$$G\left(k_x, k_y\right) = \exp\left(c_x\left(k_x - \lambda_\mathrm{c}^{-1}\right)^2 + c_y\left(k_y - \lambda_\mathrm{c}^{-1}\right)^2\right) \tag{73}$$

with λ_c the characteristic wavelength and c_x and c_y the normalization factors. Multiplying G by a pseudo-randomized phase yields

$$\begin{aligned} G_\mathrm{r}\left(k_x, k_y\right) &= G\left(k_x, k_y\right) \cdot \exp\left(2\pi i r\left(k_x, k_y\right)\right) && (74)\\ &= \exp\left(c_x\left(k_x - \lambda_\mathrm{c}^{-1}\right)^2 + c_y\left(k_y - \lambda_\mathrm{c}^{-1}\right)^2\right) \cdot \exp\left(2\pi i r\left(k_x, k_y\right)\right) && (75)\end{aligned}$$

where i is the imaginary unit and $r \in [0, 1)$ is a pseudo-randomized number for each combination of wavenumbers which is constrained by

$$\begin{aligned} r\left(k_x, k_y\right) &= -r\left(-k_x, -k_y\right) && (76)\\ r\left(-k_x, k_y\right) &= -r\left(k_x, -k_y\right) && (77)\end{aligned}$$

to ensure that the inverse Fourier transformed ($\mathcal{FT}^{-1}$) Gaussian function $\hat{G}_\mathrm{r}$ contains no imaginary parts. Hence,

$$\hat{G}_\mathrm{r}(x, y) = \mathcal{FT}^{-1}\left(G_\mathrm{r}\left(k_x, k_y\right)\right) \quad \text{with } G_\mathrm{r} \in \mathbb{I} \text{ and } \hat{G}_\mathrm{r} \in \mathbb{R}. \tag{78}$$

According to Parseval's theorem $\hat{G}_\mathrm{r}$ and G_r contain the same amount of total energy. $\hat{G}_\mathrm{r}$, furthermore, contains the desired surface pattern with continuous transitions. Thus, it is suitable—and can be used—to represent, for example, a smooth temperature distribution. However, it cannot represent the distribution of surface types because their values are discontinuous. To transform $\hat{G}_\mathrm{r}$ into a discontinuous form, a square-wave

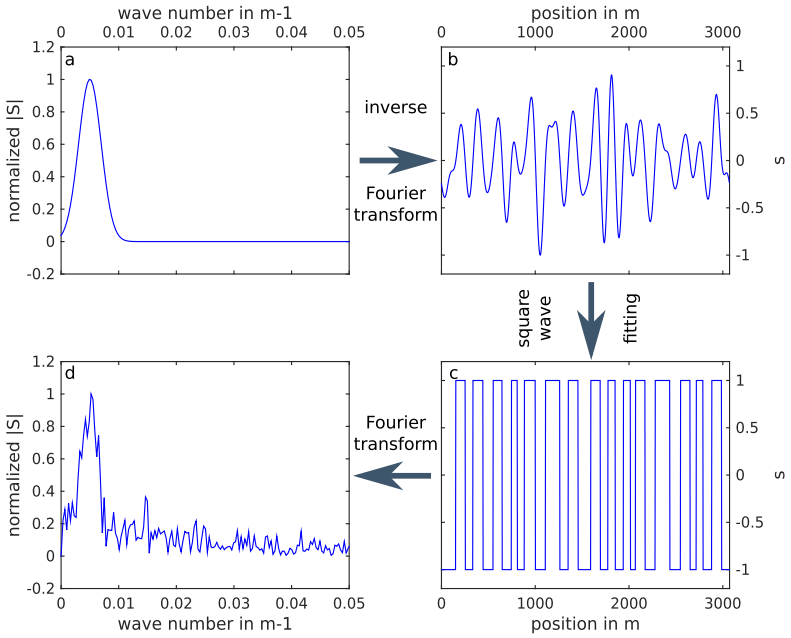

Figure 49: Exemplary one-dimensional surface pattern creation algorithm. A Gaussian function is defined in wavenumber space (a) and gets inverse Fourier transformed (b). The applied square wave fitting transforms the continuous signal into a discontinuous signal (c). Thereby, the dominating wavelength remains constant (d).

fit has to be applied, which replaces a specific amount of values by the corresponding surface type identifiers. This can be done, for example, by utilizing quantiles. For instance, setting all values smaller than the 50%-quantile to the value “ice” and all values larger than the 50%-quantile to the value “water” produces a discontinuous pattern consisting of ice and water where both account for 50% of the surface area. Due to the Gibbs phenomenon, the dominating wavelength remains constant while applying the square-wave fit. A one-dimensional exemplary visualization of this algorithm is provided in Fig. 49.

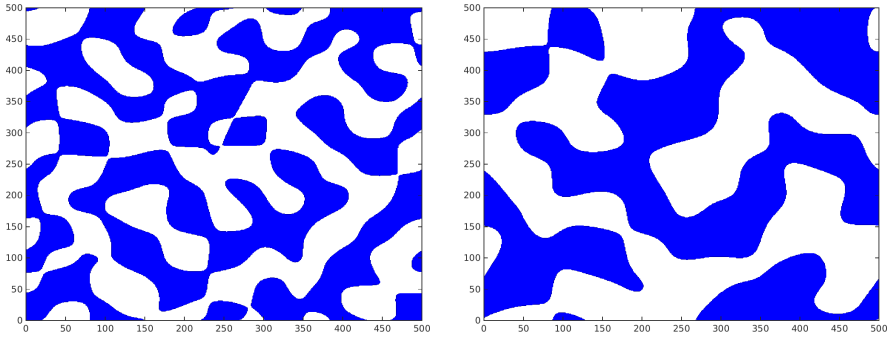

Figure 50: Two surface patterns created by the presented surface pattern creation algorithm. Their characteristic wavelength λ_c differs by a factor of 2.

The surface patterns created following this algorithm suit especially (semi-)idealized LES because their boundary conditions are periodic (Fig. 50) due to the initial definition in the wavenumber space and the performed inverse Fourier transform. As long as r is reproducible, for example, by definition of a random number seed, the created surface patterns are reproducible. Thereby, λ_c determines their characteristic wavelength and is the only required input parameter to the algorithm. However, c_x and c_y may also be utilized as input parameters. They determine how narrow or wide the initial Gaussian function is and specify the amount of occurring wavelengths in the created surface pattern. Their values are negative and the larger they are, the narrower the resulting Gaussian distribution is, and the less wavelengths appear in the created surface pattern.

Appendix C

Model Modifications

```
--- Registry/Registry.EM_COMMON
@@ -3206,0 +3207,40 @@ package    any_fft_used    fft_used==1                -
                state:t_xxx,
+
+#rora,add - start
+state real rora_swu   ikj misc 1 - - "SWUPFLX"     "short wave upward radiative flux"
                      "W m-2"
+state real rora_swd   ikj misc 1 - - "SWDNFLX"     "short wave downward radiative
    flux"               "W m-2"
+state real rora_lwu   ikj misc 1 - - "LWUPFLX"     "long wave upward radiative flux"
                      "W m-2"
+state real rora_lwd   ikj misc 1 - - "LWDNFLX"     "long wave downward radiative flux
    "                 "W m-2"
+state real rora_rc    ikj misc 1 - - "EFFR_C"      "effective radius of cloud
    droplets"               "10-6 m"
+state real rora_rr    ikj misc 1 - - "EFFR_R"      "effective radius of rain droplets
    "                 "10-6 m"
+state real rora_ri    ikj misc 1 - - "EFFR_I"      "effective radius of cloud ice"
                       "10-6 m"
+state real rora_rs    ikj misc 1 - - "EFFR_S"      "effective radius of snow"
                            "10-6 m"
+state real rora_rg    ikj misc 1 - - "EFFR_G"      "effective radius of graupel/hail"
                      "10-6 m"
+state real rora_mu    ikj misc 1 - r "RORA_MU"     "mu tendency due to large-scale
    subsidence"         "Pa s-1"
+state real rora_th    ikj misc 1 - r "RORA_TH"     "th tendency due to large-scale
    subsidence"         "K s-1"
+state real rora_ph    ikj misc 1 - r "RORA_PH"     "ph tendency due to large-scale
    subsidence"         "m2 s-3"
+state real rora_u     ikj misc 1 - r "RORA_U"      "u tendency due to large-scale
    subsidence"         "m s-2"
+state real rora_v     ikj misc 1 - r "RORA_V"      "v tendency due to large-scale
    subsidence"         "m s-2"
+state real rora_w     ikj misc 1 - r "RORA_W"      "w tendency due to large-scale
    subsidence"         "m s-2"
+state real rora_qv    ikj misc 1 - r "RORA_QV"     "qv tendency due to large-scale
    subsidence"         "kg kg-1 s-1"
+state real rora_qc    ikj misc 1 - r "RORA_QC"     "qc tendency due to large-scale
    subsidence"         "kg kg-1 s-1"
+state real rora_qr    ikj misc 1 - r "RORA_QR"     "qr tendency due to large-scale
    subsidence"         "kg kg-1 s-1"
```

```
+state real rora_qi   ikj misc 1 - r "RORA_QI"     "qi tendency due to large-scale
    subsidence"        "kg kg-1 s-1"
+state real rora_qs   ikj misc 1 - r "RORA_QS"     "qs tendency due to large-scale
    subsidence"        "kg kg-1 s-1"
+state real rora_qg   ikj misc 1 - r "RORA_QG"     "qg tendency due to large-scale
    subsidence"        "kg kg-1 s-1"
+state real rora_qrn  ikj misc 1 - r "RORA_QRN"    "qrn tendency due to large-scale
    subsidence"       "kg-1 s-1"
+state real rora_qin  ikj misc 1 - r "RORA_QIN"    "qin tendency due to large-scale
    subsidence"       "kg-1 s-1"
+state real rora_qsn  ikj misc 1 - r "RORA_QSN"    "qsn tendency due to large-scale
    subsidence"       "kg-1 s-1"
+state real rora_qgn  ikj misc 1 - r "RORA_QGN"    "qgn tendency due to large-scale
    subsidence"       "kg-1 s-1"
+state real rora_tke  ikj misc 1 - - "DEFOR_TRACE" "trace of deformation tensor"
                        "m2 s-2"
+
+rconfig integer rora_fixFluxes     namelist,physics 1 0     h "rora_fixFluxes"     "
    switch if fixed surface fluxes shall be used (=1) []"
+rconfig real    rora_lh            namelist,physics 1 0.0   h "rora_lh"           "
    optional fixed latent heat flux [W m-2]"
+rconfig real    rora_sh            namelist,physics 1 0.0   h "rora_sh"           "
    optional fixed sensible heat flux [W m-2]"
+rconfig real    rora_nc            namelist,physics 1 250.0 h "rora_nc"           "
    cloud droplet concentration in morrison microphysics [cm-3]"
+rconfig real    rora_inp           namelist,physics 1 0.16  h "rora_inp"          "
    ice nucleation particles in morrison microphysics [l-1]"
+rconfig real    rora_dtmp          namelist,physics 1 0.0   h "rora_dtmp"         "
    time step for microphysics [s]"
+rconfig real    rora_div           namelist,physics 1 0.0   h "rora_div"          "
    large-scale divergence in boundary layer [s-1]"
+rconfig real    rora_turbLev       namelist,physics 1 0.0   h "rora_turbLev"      "
    optional turbulence-seeding level []"
+rconfig real    rora_turbVal       namelist,physics 1 0.0   h "rora_turbVal"      "
    optional turbulence-seeding value (+/-) [K]"
+rconfig real   rora_thetaGradient namelist,physics 1 0.0   h "rora_thetaGradient" "
    optional gradient of theta at the model top [K m-1]"
+#rora,add - end

--- dyn_em/depend.dyn_em
@@ -236,0 +237 @@ start_em.o:     module_bc_em.o \
+     ../phys/module_rora.o \
@@ -288,0 +290 @@ module_first_rk_step_part1.o : \
+     ../phys/module_rora.o \

--- dyn_em/module_diffusion_em.F
@@ -26 +26 @@
-                                   its, ite, jts, jte, kts, kte      )
+                                   its, ite, jts, jte, kts, kte, sub_tke      ) !
    rora,add
@@ -77,0 +78,2 @@
+     real,dimension(ims:ime,kms:kme,jms:jme),intent(out) :: sub_tke              !
    rora,add
+
@@ -1181,0 +1184,12 @@
```

```
+!rora,add - start
+do j = jts,jte,1
+do k = kts,kte,1
+do i = its,ite,1
+  sub_tke(i,k,j) = defor11(i,k,j)**2 + defor22(i,k,j)**2 + defor33(i,k,j)**2 + &
+    2*defor12(i,k,j)**2 + 2*defor13(i,k,j)**2 + 2*defor23(i,k,j)**2
+  sub_tke(i,k,j) = sqrt(sub_tke(i,k,j))
+end do
+end do
+end do
+!rora,add - end
+
```

--- **dyn_em/module_em.F**

```
@@ -1854,0 +1855,5 @@ SUBROUTINE calculate_phy_tend (config_flags,c1,c2,
                          &
+!rora,add - start
+rora_mu,rora_th,rora_u,rora_v,rora_w,                                    &
+rora_qv,rora_qc,rora_qr,rora_qi,rora_qs,rora_qg,                         &
+rora_qrn,rora_qin,rora_qsn,rora_qgn,                                     &
+!rora,add - end
@@ -1880,0 +1886,7 @@ SUBROUTINE calculate_phy_tend (config_flags,c1,c2,
                          &
+!rora,add - start
+real, dimension(ims:ime,jms:jme), intent(inout) :: rora_mu
+real, dimension(ims:ime,kms:kme,jms:jme), intent(inout) :: rora_th,      &
+  rora_u,rora_v,rora_w,rora_qv,rora_qc,rora_qr,rora_qi,rora_qs,rora_qg,   &
+  rora_qrn,rora_qin,rora_qsn,rora_qgn
+!rora,add - end
+
@@ -1965,0 +1978,39 @@ SUBROUTINE calculate_phy_tend (config_flags,c1,c2,
                          &
+!rora,add - start
+if (config_flags%rora_div /= 0.0) then
+  do j = jts,jtf,1
+  do i = its,itf,1
+    rora_mu(i,j) = mut(i,j) * rora_mu(i,j)
+  end do
+  end do
+  do j = jts,jtf,1
+  do k = kts,ktf,1
+  do i = its,itf,1
+    rora_th(i,k,j) = (c1(k)*mut(I,J)+c2(k)) * rora_th(i,k,j)
+    rora_u(i,k,j) = (c1(k)*mut(I,J)+c2(k)) * rora_u(i,k,j)
+    rora_v(i,k,j) = (c1(k)*mut(I,J)+c2(k)) * rora_v(i,k,j)
+    rora_qv(i,k,j) = (c1(k)*mut(I,J)+c2(k)) * rora_qv(i,k,j)
+    rora_qc(i,k,j) = (c1(k)*mut(I,J)+c2(k)) * rora_qc(i,k,j)
+    rora_qr(i,k,j) = (c1(k)*mut(I,J)+c2(k)) * rora_qr(i,k,j)
+    rora_qi(i,k,j) = (c1(k)*mut(I,J)+c2(k)) * rora_qi(i,k,j)
+    rora_qs(i,k,j) = (c1(k)*mut(I,J)+c2(k)) * rora_qs(i,k,j)
+    rora_qg(i,k,j) = (c1(k)*mut(I,J)+c2(k)) * rora_qg(i,k,j)
+    rora_qrn(i,k,j) = (c1(k)*mut(I,J)+c2(k)) * rora_qrn(i,k,j)
+    rora_qin(i,k,j) = (c1(k)*mut(I,J)+c2(k)) * rora_qin(i,k,j)
+    rora_qsn(i,k,j) = (c1(k)*mut(I,J)+c2(k)) * rora_qsn(i,k,j)
+    rora_qgn(i,k,j) = (c1(k)*mut(I,J)+c2(k)) * rora_qgn(i,k,j)
```

```
+  end do
+  end do
+  do k = kts+1,ktf,1
+  do i = its,itf,1
+    rora_w(i,k,j) = ((c1(k)+c1(k-1))*mut(I,J)+(c2(k)+c2(k-1)))/2 * rora_w(i,k,j)
+  end do
+  end do
+  !lowest and uppest level always zero in w-tendency
+  do i = its,itf,1
+    rora_w(i,ktf,j) = 0.0
+    rora_w(i,kts,j) = 0.0
+   end do
+   end do
+end if
+!rora,add - end
+
```

--- **dyn_em/module_first_rk_step_part1.F**

```
@@ -51,0 +52 @@ CONTAINS
+    use module_rora, only: rora_subsidence                                    !
     rora,add
@@ -216,0 +218,24 @@ BENCH_END(phy_prep_tim)
+!rora,add - start
+!$OMP PARALLEL DO &
+!$OMP PRIVATE(ij)
+do ij = 1,grid%num_tiles,1
+  call rora_subsidence(config_flags%rora_thetaGradient,config_flags%rora_div, &
+    grid%z,grid%z_at_w,                                                       &
+    th_phy,grid%ph_2+grid%phb,grid%u_phy,grid%v_phy,grid%w_2,                 &
+    moist(ims,kms,jms,P_QV),moist(ims,kms,jms,P_QC),moist(ims,kms,jms,P_QR), &
+    moist(ims,kms,jms,P_QI),moist(ims,kms,jms,P_QS),moist(ims,kms,jms,P_QG), &
+    scalar(ims,kms,jms,P_QNR),scalar(ims,kms,jms,P_QNI),                     &
+    scalar(ims,kms,jms,P_QNS),scalar(ims,kms,jms,P_QNG),                     &
+    grid%rora_mu,grid%rora_th,grid%rora_ph,                                   &
+    grid%rora_u,grid%rora_v,grid%rora_w,                                      &
+    grid%rora_qv,grid%rora_qc,grid%rora_qr,                                   &
+    grid%rora_qi,grid%rora_qs,grid%rora_qg,                                   &
+    grid%rora_qrn,grid%rora_qin,grid%rora_qsn,grid%rora_qgn,                  &
+    ims,ime,jms,jme,kms,kme,                                                  &
+    grid%i_start(ij),min(grid%i_end(ij),ide-1),                               &
+    grid%j_start(ij),min(grid%j_end(ij),jde-1),                               &
+    k_start,k_end)
+end do
+!$OMP END PARALLEL DO
+!rora,add - end
+
@@ -329,0 +355,4 @@ BENCH_START(rad_driver_tim)
+!rora,add - start
+&,rora_swu=grid%rora_swu,rora_swd=grid%rora_swd                               &
+&,rora_lwu=grid%rora_lwu,rora_lwd=grid%rora_lwd                               &
+!rora,add - end
@@ -448,0 +478,4 @@ BENCH_START(surf_driver_tim)
+!rora,add - start
+&rora_fixFluxes=config_flags%rora_fixFluxes,                                  &
+&rora_lh=config_flags%rora_lh,rora_sh=config_flags%rora_sh,                   &
```

```
+!rora,add - end

--- dyn_em/module_first_rk_step_part2.F
@@ -321,0 +322,5 @@ BENCH_START(cal_phy_tend)
+!rora,add - start
+grid%rora_mu,grid%rora_th,grid%rora_u,grid%rora_v,grid%rora_w,                    &
+grid%rora_qv,grid%rora_qc,grid%rora_qr,grid%rora_qi,grid%rora_qs,grid%rora_qg,    &
+grid%rora_qrn,grid%rora_qin,grid%rora_qsn,grid%rora_qgn,                          &
+!rora,add - end
@@ -450 +455 @@ BENCH_START(deform_div_tim)
-                                     k_start     , k_end                     )
+                                     k_start     , k_end,grid%rora_tke       )    !
    rora,add
@@ -682,0 +688,6 @@ BENCH_START(update_phy_ten_tim)
+!rora,add - start
+rw_tendf,                                                                         &
+grid%rora_mu,grid%rora_th,grid%rora_ph,grid%rora_u,grid%rora_v,grid%rora_w,       &
+grid%rora_qv,grid%rora_qc,grid%rora_qr,grid%rora_qi,grid%rora_qs,grid%rora_qg,    &
+grid%rora_qrn,grid%rora_qin,grid%rora_qsn,grid%rora_qgn,                          &
+!rora,add - end

--- dyn_em/module_initialize_ideal.F
@@ -134 +134 @@ CONTAINS
-   REAL :: randx        ! for LES
+   REAL :: randx,randx_rora        ! for LES                                      !
    rora,add
@@ -138,0 +139,9 @@ CONTAINS
+!rora,add - start
+real :: z_in_at_w,p_in_top,p_in_surf,theta_in_surf
+integer :: ierr,myid
+integer,dimension(8) :: seedArr = (/2,3,5,7,11,13,17,19/)
+call MPI_COMM_RANK(MPI_COMM_WORLD,myid,ierr)
+seedArr = seedArr**myid
+call random_seed(put=seedArr)
+!rora,add - end
+
@@ -569,4 +578,5 @@ CONTAINS
-    CALL nl_set_mminlu(1,'     ')
-    CALL nl_set_iswater(1,0)
-    CALL nl_set_cen_lat(1,40.)
-    CALL nl_set_cen_lon(1,-105.)
+    CALL nl_set_mminlu(1,'USGS')                                                  !
    rora,mod
+    CALL nl_set_iswater(1,16)                                                     !
    rora,mod
+     call nl_set_isice(1,24)                                                      !
    rora,add
+    CALL nl_set_cen_lat(1,81.93)                                                  !
    rora,mod (31.3 DYCOMS; 81.93 ACLOUD)
+    CALL nl_set_cen_lon(1,10.95)                                                  !
    rora,mod (-121.7 DYCOMS; 10.95 ACLOUD)
@@ -579,0 +590,2 @@ CONTAINS
+     call nl_get_iswater(1,grid%iswater)                                          !
    rora,add
+     call nl_get_isice(1,grid%isice)                                              !
```

```
     rora,add
@@ -580,0 +593,6 @@ CONTAINS
+!rora,add - start
+open(unit=42,file='input_sounding',form='formatted',status='old')
+rewind(42)
+read(42,*) p_in_surf,theta_in_surf
+close(42)
+!rora,add - end
@@ -598 +616,3 @@ CONTAINS
-          grid%f(i,j)         = 1.e-4
+          grid%f(i,j)         = 1.44e-4                                    !
     rora,mod (0.756 DYCOMS; 1.44 ACLOUD)
+          grid%xland(i,j)     = 1.0                                        !
     rora,add (2.0 DYCOMS; 1.0 ACLOUD)
+          grid%lu_index(i,j) = 24                                          !
     rora,add (16 DYCOMS; 24 ACLOUD)
@@ -646,0 +667,6 @@ CONTAINS
+!rora,add -start
+call get_sounding(zk,p_in,pd_in,theta,rho,u,v,qv,.false.,nl_max,nl_in,theta_surf)
+p_in_top = interp_0(p_in,zk,config_flags%ztop,nl_in)
+open(unit=42,file='input_heights',form='formatted',status='old')
+rewind(42)
+!rora,add - end
@@ -648 +674,6 @@ CONTAINS
-       grid%znw(k) = 1. - float(k-1)/float(kde-1)
+!rora,add - start
+       !grid%znw(k) = 1. - float(k-1)/float(kde-1)
+read(42,*) z_in_at_w
+grid%znw(k) = (interp_0(p_in,zk,z_in_at_w,nl_in) - p_in_top) &
+  / (100.0*p_in_surf-p_in_top)
+!rora,add - end
@@ -649,0 +681 @@ CONTAINS
+      close(42)                                                            !
     rora,add
@@ -1369,0 +1402 @@ CONTAINS
+       call random_number (randx_rora)                                     !
     rora,add
@@ -1370,0 +1404 @@ CONTAINS
+       randx_rora = randx_rora-0.5                                         !
     rora,add
@@ -1394,0 +1429,17 @@ CONTAINS
+!rora,add - start
+k = config_flags%rora_turbLev
+grid%t_1(i,k,j) = grid%t_1(i,k,j) + config_flags%rora_turbVal * randx_rora
+grid%t_2(i,k,j) = grid%t_1(i,k,j)
+qvf = 1. + rvovrd*moist(i,k,j,P_QV)
+grid%alt(i,k,j) = (r_d/p1000mb)*(grid%t_1(i,k,j)+t0)*qvf* &
+  (((grid%p(i,k,j)+grid%pb(i,k,j))/p1000mb)**cvpm)
+grid%al(i,k,j) = grid%alt(i,k,j) - grid%alb(i,k,j)
+k = k+1
+grid%t_1(i,k,j) = grid%t_1(i,k,j) - config_flags%rora_turbVal * randx_rora
+grid%t_2(i,k,j) = grid%t_1(i,k,j)
+qvf = 1. + rvovrd*moist(i,k,j,P_QV)
+grid%alt(i,k,j) = (r_d/p1000mb)*(grid%t_1(i,k,j)+t0)*qvf* &
+  (((grid%p(i,k,j)+grid%pb(i,k,j))/p1000mb)**cvpm)
```

```
+grid%al(i,k,j) = grid%alt(i,k,j) - grid%alb(i,k,j)
+!rora,add - end
+
@@ -1626,2 +1677,2 @@ CONTAINS
-          grid%tsk(i,j) = theta_surf * (p_surf/p1000mb)**rcp
-          grid%tmn(i,j) = grid%tsk(i,j)-0.5
+          grid%tsk(i,j) = theta_in_surf * (100.0*p_in_surf/p1000mb)**rcp          !
     rora,mod
+          grid%tmn(i,j) = grid%tsk(i,j)                                           !
     rora,mod

--- dyn_em/solve_em.F
@@ -119,0 +120 @@ SUBROUTINE solve_em ( grid , config_flags  &
+    real :: rora_temp                                                             !
     rora,add
@@ -3520,0 +3522,10 @@ BENCH_END(advance_ppt_tim)
+!rora,add - start
+if ( (grid%itimestep .EQ. 1) .OR. (grid%rora_dtmp .EQ. 0.0) .OR.                  &
+  (mod(grid%itimestep,max(nint(config_flags%rora_dtmp/dtm),1)) .EQ. 1) ) then
+  if(config_flags%rora_dtmp > 0.0) then
+    rora_temp = config_flags%rora_dtmp
+  else
+    rora_temp = dtm
+  end if
+!rora,add - end
+
@@ -3542 +3553 @@ BENCH_START(moist_physics_prep_tim)
-                                    dtm, grid%h_diabatic,                         &
+                                    rora_temp, grid%h_diabatic,                   &!
     rora,mod (from dtm)
@@ -3553,2 +3564,2 @@ BENCH_START(moist_physics_prep_tim)
-          CALL bulk_dust_emis (grid%itimestep,dtm,config_flags%num_soil_layers  &
+          CALL bulk_dust_emis (grid%itimestep,rora_temp                         &!
     rora,mod (from dtm)
+               ,config_flags%num_soil_layers                                    &!
     rora,mod (new line)
@@ -3598 +3610 @@ BENCH_START(micro_driver_tim)
-      &          DT=dtm               ,DX=grid%dx               ,DY=grid%dy    &
+      &          DT=rora_temp         ,DX=grid%dx               ,DY=grid%dy    &     !
     rora,mod (from dtm)
@@ -3612,0 +3625,4 @@ BENCH_START(micro_driver_tim)
+!rora,add - start
+&,rora_rc=grid%rora_rc,rora_rr=grid%rora_rr                                       &
+&,rora_ri=grid%rora_ri,rora_rs=grid%rora_rs,rora_rg=grid%rora_rg                  &
+!rora,add - end
@@ -3857 +3873 @@ BENCH_START(moist_phys_end_tim)
-                                      grid%h_diabatic, dtm,                       &
+                                      grid%h_diabatic, rora_temp,                 &!
     rora,mod (from dtm)
@@ -3871,0 +3888 @@ BENCH_START(moist_phys_end_tim)
+end if                                                                            !
     rora,add

--- dyn_em/start_em.F
@@ -974,0 +975,5 @@ endif
```

```
+!rora,add - start
+grid%rora_mu,grid%rora_th,grid%rora_ph,grid%rora_u,grid%rora_v,grid%rora_w,     &
+grid%rora_qv,grid%rora_qc,grid%rora_qr,grid%rora_qi,grid%rora_qs,grid%rora_qg, &
+grid%rora_qrn,grid%rora_qin,grid%rora_qsn,grid%rora_qgn,                       &
+!rora,add - end

--- main/depend.common
@@ -504,0 +505 @@ module_physics_init.o : \
+     module_rora.o \

---phys/Makefile
@@ -8,0 +9 @@ MODULES = \
+   module_rora.o \

--- phys/module_microphysics_driver.F
@@ -13,0 +14 @@ SUBROUTINE microphysics_driver(
                                                 &
+,rora_rc,rora_rr,rora_ri,rora_rs,rora_rg                                       &!
     rora,add
@@ -355,0 +357,6 @@ SUBROUTINE microphysics_driver(
                                                 &
+
+!rora,add - start
+real,dimension(ims:ime,kms:kme,jms:jme),intent(out) :: rora_rc,rora_rr,        &
+   rora_ri,rora_rs,rora_rg
+!rora,add - end
+
@@ -1046,0 +1054,5 @@ REAL, DIMENSION( ims:ime, kms:kme, jms:jme ),
                               &
+!rora,add - start
+rora_nc=config_flags%rora_nc,rora_inp=config_flags%rora_inp,                   &
+rora_rc=rora_rc,rora_rr=rora_rr,                                               &
+rora_ri=rora_ri,rora_rs=rora_rs,rora_rg=rora_rg,                               &
+!rora,add - end

--- phys/module_mp_morr_two_moment.F
+++ b/WRFLES-4.0.3/phys/module_mp_morr_two_moment.F
@@ -327 +327 @@ SUBROUTINE MORR_TWO_MOMENT_INIT(morr_rimed_ice) ! RAS
-       INUC = 0
+       INUC = 1                                                                !
     rora,mod (from 0)
@@ -333 +333 @@ SUBROUTINE MORR_TWO_MOMENT_INIT(morr_rimed_ice) ! RAS
-       IGRAUP = 0
+       IGRAUP = 1                                                              !
     rora,mod (from 0)
@@ -563,0 +564 @@ SUBROUTINE MP_MORR_TWO_MOMENT(ITIMESTEP,                                        &
+                  rora_nc,rora_inp,rora_rc,rora_rr,rora_ri,rora_rs,rora_rg,&    !
     rora,add
@@ -648,0 +650,7 @@ SUBROUTINE MP_MORR_TWO_MOMENT(ITIMESTEP,                                       &
+
+!rora,add - start
+real,intent(in) :: rora_nc,rora_inp
+real,dimension(ims:ime,kms:kme,jms:jme),intent(out) :: rora_rc,rora_rr,        &
+   rora_ri,rora_rs,rora_rg
+!rora,add - end
```

```
+
@@ -810,0 +819 @@ SUBROUTINE MP_MORR_TWO_MOMENT(ITIMESTEP,                                  &
+       rora_nc,rora_inp,                                                 &!
     rora,add
@@ -857,0 +867,8 @@ SUBROUTINE MP_MORR_TWO_MOMENT(ITIMESTEP,                                  &
+!rora,add - start
+rora_rc(i,k,j) = effc(i,k,j)
+rora_rr(i,k,j) = effr(i,k,j)
+rora_ri(i,k,j) = effi(i,k,j)
+rora_rs(i,k,j) = effs(i,k,j)
+rora_rg(i,k,j) = effg(i,k,j)
+!rora,add - end
+
@@ -917,0 +935 @@ END SUBROUTINE MP_MORR_TWO_MOMENT
+       rora_nc,rora_inp,                                                 &!
     rora,add
@@ -961,0 +980 @@ END SUBROUTINE MP_MORR_TWO_MOMENT
+      real,intent(in) :: rora_nc,rora_inp                                 !
     rora,add
@@ -1252,0 +1272,2 @@ END SUBROUTINE MP_MORR_TWO_MOMENT
+NDCNST = rora_nc                                                         !
     rora,add
+
@@ -2893 +2914 @@ END SUBROUTINE MP_MORR_TWO_MOMENT
-              KC2 = 0.16*1000./RHO(K)  ! CONVERT FROM L-1 TO KG-1
+              KC2 = rora_inp*1000./RHO(K)  ! CONVERT FROM L-1 TO KG-1      !
     rora,mod (from 0.16)

--- phys/module_physics_addtendc.F
@@ -29,0 +30,8 @@ SUBROUTINE update_phy_ten(rph_tendf,rt_tendf,ru_tendf,rv_tendf,
     moist_tendf, &
+
+!rora,add - start
+rw_tendf,                                                                &
+rora_mu,rora_th,rora_ph,rora_u,rora_v,rora_w,                            &
+rora_qv,rora_qc,rora_qr,rora_qi,rora_qs,rora_qg,                         &
+rora_qrn,rora_qin,rora_qsn,rora_qgn,                                     &
+!rora,add - end
+
@@ -55,0 +64,8 @@ SUBROUTINE update_phy_ten(rph_tendf,rt_tendf,ru_tendf,rv_tendf,
     moist_tendf, &
+!rora,add - start
+real, dimension(ims:ime,kms:kme,jms:jme), intent(inout) :: rw_tendf
+real, dimension(ims:ime,jms:jme), intent(in) :: rora_mu
+real, dimension(ims:ime,kms:kme,jms:jme), intent(in) :: rora_th,rora_ph,  &
+  rora_u,rora_v,rora_w,rora_qv,rora_qc,rora_qr,rora_qi,rora_qs,rora_qg,   &
+  rora_qrn,rora_qin,rora_qsn,rora_qgn
+!rora,add - end
+
@@ -112 +128,39 @@ SUBROUTINE update_phy_ten(rph_tendf,rt_tendf,ru_tendf,rv_tendf,
     moist_tendf, &
-                                                    rqvfrten
+                                                    rqvfrten
+
+!rora,add - start
```

```
+if (config_flags%rora_div /= 0.0) then
+  call add_a2a(mu_tendf,rora_mu,config_flags,                                    &
+    ids,ide,jds,jde,kds,kde,ims,ime,jms,jme,kms,kme,its,ite,jts,jte,kts,kte)
+  call add_a2a(rt_tendf,rora_th,config_flags,                                    &
+    ids,ide,jds,jde,kds,kde,ims,ime,jms,jme,kms,kme,its,ite,jts,jte,kts,kte)
+  call add_a2a_ph(rph_tendf,rora_ph,config_flags,                                &
+    ids,ide,jds,jde,kds,kde,ims,ime,jms,jme,kms,kme,its,ite,jts,jte,kts,kte)
+  call add_a2c_u(ru_tendf,rora_u,config_flags,                                   &
+    ids,ide,jds,jde,kds,kde,ims,ime,jms,jme,kms,kme,its,ite,jts,jte,kts,kte)
+  call add_a2c_v(rv_tendf,rora_v,config_flags,                                   &
+    ids,ide,jds,jde,kds,kde,ims,ime,jms,jme,kms,kme,its,ite,jts,jte,kts,kte)
+  call add_a2a_ph(rw_tendf,rora_w,config_flags,                                  &
+    ids,ide,jds,jde,kds,kde,ims,ime,jms,jme,kms,kme,its,ite,jts,jte,kts,kte)
+  call add_a2a(moist_tendf(ims,kms,jms,P_QV),rora_qv,config_flags,               &
+    ids,ide,jds,jde,kds,kde,ims,ime,jms,jme,kms,kme,its,ite,jts,jte,kts,kte)
+  call add_a2a(moist_tendf(ims,kms,jms,P_QC),rora_qc,config_flags,               &
+    ids,ide,jds,jde,kds,kde,ims,ime,jms,jme,kms,kme,its,ite,jts,jte,kts,kte)
+  call add_a2a(moist_tendf(ims,kms,jms,P_QR),rora_qr,config_flags,               &
+    ids,ide,jds,jde,kds,kde,ims,ime,jms,jme,kms,kme,its,ite,jts,jte,kts,kte)
+  call add_a2a(moist_tendf(ims,kms,jms,P_QI),rora_qi,config_flags,               &
+    ids,ide,jds,jde,kds,kde,ims,ime,jms,jme,kms,kme,its,ite,jts,jte,kts,kte)
+  call add_a2a(moist_tendf(ims,kms,jms,P_QS),rora_qs,config_flags,               &
+    ids,ide,jds,jde,kds,kde,ims,ime,jms,jme,kms,kme,its,ite,jts,jte,kts,kte)
+  call add_a2a(moist_tendf(ims,kms,jms,P_QG),rora_qg,config_flags,               &
+    ids,ide,jds,jde,kds,kde,ims,ime,jms,jme,kms,kme,its,ite,jts,jte,kts,kte)
+  call add_a2a(scalar_tendf(ims,kms,jms,P_QNR),rora_qrn,config_flags,            &
+    ids,ide,jds,jde,kds,kde,ims,ime,jms,jme,kms,kme,its,ite,jts,jte,kts,kte)
+  call add_a2a(scalar_tendf(ims,kms,jms,P_QNI),rora_qin,config_flags,            &
+    ids,ide,jds,jde,kds,kde,ims,ime,jms,jme,kms,kme,its,ite,jts,jte,kts,kte)
+  call add_a2a(scalar_tendf(ims,kms,jms,P_QNS),rora_qsn,config_flags,            &
+    ids,ide,jds,jde,kds,kde,ims,ime,jms,jme,kms,kme,its,ite,jts,jte,kts,kte)
+  call add_a2a(scalar_tendf(ims,kms,jms,P_QNG),rora_qgn,config_flags,            &
+    ids,ide,jds,jde,kds,kde,ims,ime,jms,jme,kms,kme,its,ite,jts,jte,kts,kte)
+end if
+!rora,add - end
+
```

--- phys/module_physics_init.F

```
@@ -28,0 +29,5 @@ CONTAINS
+!rora,add - start
+rora_mu,rora_th,rora_ph,rora_u,rora_v,rora_w,                                    &
+rora_qv,rora_qc,rora_qr,rora_qi,rora_qs,rora_qg,                                 &
+rora_qrn,rora_qin,rora_qsn,rora_qgn,                                             &
+!rora,add - end
@@ -239,0 +245 @@ CONTAINS
+   use module_rora, only: rora_subsidence_init                                    !
    rora,add
@@ -258,0 +265,7 @@ CONTAINS
+!rora,add - start
+real,dimension(ims:ime,jms:jme),intent(out) :: rora_mu
+real,dimension(ims:ime,kms:kme,jms:jme),intent(out) :: rora_th,rora_ph,          &
+  rora_u,rora_v,rora_w,rora_qv,rora_qc,rora_qr,rora_qi,rora_qs,rora_qg,           &
+  rora_qrn,rora_qin,rora_qsn,rora_qgn
+!rora,add - end
+
```

```
@@ -1355,0 +1369,7 @@ integer myproc
+!rora,add - start
+call rora_subsidence_init(rora_mu,rora_th,rora_ph,rora_u,rora_v,rora_w,          &
+   rora_qv,rora_qc,rora_qr,rora_qi,rora_qs,rora_qg,                              &
+   rora_qrn,rora_qin,rora_qsn,rora_qgn,                                          &
+   ims,ime,jms,jme,kms,kme,its,ite,jts,jte,kts,kte)
+!rora,add - end
+
```

--- **phys/module_ra_rrtmg_lw.F**

```
@@ -11458,0 +11459 @@ CONTAINS
+                           rora_lwu,rora_lwd,                                  &          !
     rora,add
@@ -11607,0 +11609 @@ CONTAINS
+    real,dimension(ims:ime,kms:kme,jms:jme),intent(out) :: rora_lwu,rora_lwd    !
     rora,add
@@ -12683,0 +12686,7 @@ CONTAINS
+!rora,add - start
+do k = kts,kte,1
+   rora_lwu(i,k,j) = uflx(1,k+1)
+   rora_lwd(i,k,j) = dflx(1,k+1)
+end do
+!rora,add - end
+
```

--- **phys/module_ra_rrtmg_sw.F**

```
@@ -3268,0 +3269,2 @@
+      sfluxzen = 0.0                                                           !
     rora,add
+
@@ -9897,0 +9900 @@ CONTAINS
+                           rora_swu,rora_swd,                                  &          !
     rora,add
@@ -10101,0 +10105,2 @@ CONTAINS
+    real,dimension(ims:ime,kms:kme,jms:jme),intent(out) :: rora_swu,rora_swd    !
     rora,add
+
@@ -11163,0 +11169,7 @@ CONTAINS
+!rora,add - start
+do k = kts,kte,1
+   rora_swu(i,k,j) = swuflx(1,k+1)
+   rora_swd(i,k,j) = swdflx(1,k+1)
+end do
+!rora,add - end
+
```

--- **phys/module_radiation_driver.F**

```
@@ -135,0 +136 @@ CONTAINS
+               ,rora_swu,rora_swd,rora_lwu,rora_lwd                           &          !
     rora,add
@@ -539,0 +541,5 @@ CONTAINS
+!rora,add - start
+real,dimension(ims:ime,kms:kme,jms:jme),intent(out) ::                         &
+   rora_swu,rora_swd,rora_lwu,rora_lwd
+!rora,add - end
```

```
+
@@ -1699,0 +1706 @@ CONTAINS
+                    rora_lwu=rora_lwu,rora_lwd=rora_lwd,                &          !
    rora,add
@@ -2158,0 +2166 @@ CONTAINS
+                        rora_swu=rora_swu,rora_swd=rora_swd,                &          !
    rora,add
```

--- **phys/module_rora.F**

new file (see Appendix A)

--- **phys/module_sf_sfclayrev.F**

```
@@ -14,0 +15 @@ CONTAINS
+                        rora_fixFluxes,rora_lh,rora_sh,                &          !
    rora,add
@@ -119,0 +121,6 @@ CONTAINS
+
+!rora,add - start
+integer,intent(in) :: rora_fixFluxes
+real,intent(in) :: rora_lh,rora_sh
+!rora,add - end
+
@@ -221,0 +229 @@ CONTAINS
+                  rora_fixFluxes,rora_lh,rora_sh,                &          !
    rora,add
@@ -250,0 +259 @@ CONTAINS
+                        rora_fixFluxes,rora_lh,rora_sh,                &          !
    rora,add
@@ -273,0 +283,6 @@ CONTAINS
+
+!rora,add - start
+integer,intent(in) :: rora_fixFluxes
+real,intent(in) :: rora_lh,rora_sh
+!rora,add - end
+
@@ -1029,0 +1045,8 @@ CONTAINS
+
+!rora,add - start
+if (rora_fixFluxes == 1) then
+  lh(i) = rora_lh
+  qfx(i) = lh(i)/xlv
+end if
+!rora,add - end
+
@@ -1047 +1070,8 @@ CONTAINS
-        ENDIF
+        ENDIF
+
+!rora,add - start
+if (rora_fixFluxes == 1) then
+  hfx(i) = rora_sh
+end if
+!rora,add - end
+
```

```
--- phys/module_surface_driver.F
@@ -6,0 +7 @@ CONTAINS
+     &           rora_fixFluxes,rora_lh,rora_sh,                    &        !
     rora,add
@@ -563,0 +565,5 @@ CONTAINS
+!rora,add - start
+integer,intent(in) :: rora_fixFluxes
+real,intent(in) :: rora_lh,rora_sh
+!rora,add - end
+
@@ -1935 +1941,2 @@ CONTAINS
-                  p_phy,dz8w,cp,g,rcp,r_d,xlv,psfc,chs,chs2,cqs2,cpm, &
+                  p_phy,dz8w,rora_fixFluxes,rora_lh,rora_sh,          &        !
     rora,add
+                  cp,g,rcp,r_d,xlv,psfc,chs,chs2,cqs2,cpm, &                   !
     rora,mod (new line)
@@ -1953 +1960,2 @@ CONTAINS
-                p_phy,dz8w,cp,g,rcp,r_d,xlv,psfc,chs,chs2,cqs2,cpm, &
+                p_phy,dz8w,rora_fixFluxes,rora_lh,rora_sh,           &        !
     rora,add
+                cp,g,rcp,r_d,xlv,psfc,chs,chs2,cqs2,cpm, &                     !
     rora,mod (new line)
@@ -5492,0 +5501 @@ TICE2TSK_IF2COLD,XICE_THRESHOLD,
                                        &
+                       rora_fixFluxes,rora_lh,rora_sh,                 &       !
     rora,add
@@ -5518,0 +5528,5 @@ TICE2TSK_IF2COLD,XICE_THRESHOLD,
                                        &
+!rora,add - start
+integer,intent(in) :: rora_fixFluxes
+real,intent(in) :: rora_lh,rora_sh
+!rora,add - end
+
@@ -5744,0 +5759 @@ TICE2TSK_IF2COLD,XICE_THRESHOLD,
                                        &
+                  rora_fixFluxes,rora_lh,rora_sh,                  &        !
     rora,add
@@ -5827,0 +5843 @@ TICE2TSK_IF2COLD,XICE_THRESHOLD,
                                        &
+                  rora_fixFluxes,rora_lh,rora_sh,                  &        !
     rora,add

--- run/LANDUSE.TBL
@@ -57 +57 @@ SUMMER
-24,      55.,    .95,    .95,    0.1,     5.,     0., 9.0e25,'Snow or Ice'
+24,      85.,    .95,    .95,    0.1,     5.,     0., 9.0e25,'Snow or Ice'
@@ -91 +91 @@ WINTER
-24,      70.,    .95,    .95,    0.1,     5.,     0., 9.0e25,'Snow or Ice'
+24,      85.,    .95,    .95,    0.1,     5.,     0., 9.0e25,'Snow or Ice'
```